ADSORPTION MECHANISMS OF As AND B OXYANIONS FOR WATER REMEDIATION APPLICATIONS. SYNTHESIS OF ADSORBENTS AND CHARACTERIZATION USING X-RAY ABSORPTION SPECTROSCOPY.

Xiangyang Lou

Universitat Autònoma de Barcelona

ADSORPTION MECHANISMS OF As AND B OXYANIONS FOR WATER REMEDIATION APPLICATIONS.

SYNTHESIS OF ADSORBENTS AND CHARACTERIZATION USING X-RAY ABSORPTION SPECTROSCOPY.

Xiangyang Lou

Doctoral Thesis

Doctorate Program in Chemistry

Directors: Manuel Valiente Malmagro

Roberto Boada Romero

Department of Chemistry

Faculty of science

2021

Universitat Autònoma de Barcelona

Report submitted to aspire for the Doctor Degree by

Xiangyang Lou

Approval:

Directors: Manuel Valiente Roberto Boada

Bellaterra, 2/09/2021

ACKNOWLEDGMENT

First of all, I want to thank my supervisors Manuel Valiente and Roberto Boada for their patient guidance. Many thanks to you, Manolo, for accepting me as a PhD candidate, this is where the story began. You with your vast knowledge, rich experience, and insightful criticism gave me invaluable advice on my experiments and thesis. Your enthusiasm for your work also encouraged me a lot for my career. Many thanks to you, Roberto, for all the constant encouragement and selfless assistance. We worked together to talk about the details of the experiments, methods of the data treatment, writing of the thesis and manuscripts. Without your vast help, it would be three thousand times harder for me to finish this thesis.

Many thanks to the secretary team: Maria Dolors, Alba and Carme. You were always here to help me no matter what difficulties I encountered.

Many thanks to the GTS-Seniors and Technical staff: Montse, Cristina, Mari, Gustavo, Mon, Manu, Victor. All of you are so nice and give me lots of suggestions and help on both my experiments and life. Special thanks to Mon and Manu for their help in ICP detections.

I would like to thank the lab A team: Laia and Dong; Biomat team: Sandra and Jorge; Stone Office team: Iris; Plant's team: Nithya, Marilyn and Marcia; my TFG: Diana. It was a great pleasure for me to work with all of you.

I also would like to express my gratitude to all the researches from other countries that worked with me during their stay at GTS: Cuba team (Margarita, Toky, Louis); Argentina team (Lucia, Nancy).

I would also like to thank previous GTS members: Vero, Jingjing, Tingting, M. Ángles, Clara, Elena. Thanks for all the wonderful time we shared together.

I would also like to thank my family (my parents, my girlfriend, my younger sister) and friends in China, who have been always supporting me all these four years.

Last but not least, I would like to thanks the financial support of Chinese Scholarship Council (201708110179) for providing me the scholarship to study at the UAB, and ALBA synchrotron facility for providing us the beamtime no. 2018093125 at BL22-CLAESS beamline. Laboratory expenses and costs of services providers have been covered by EU-H2020 research project NANOREMOVAS (No. 645024) and Spanish Ministry MINECO project CHEMNEXUS (No. 665919).

SUMMARY

The research carried out in the present thesis concerns with the development of new adsorption materials and procedures to improve the removal efficiency of contaminants oxyanions from polluted waters, particularly arsenic (As) and boron (B), in order to implement procedures to accomplish the actual water regulations.

For As removal, many adsorbents with high adsorption capacity and good selectivity have been reported, while most of them are in powder form and have rather limited industrial applicability. In this study, a commercial cube-shaped open-celled cellulose sponge adsorbent was modified by in-situ co-precipitation of superparamagnetic iron oxide nanoparticles (SPION) and used to remove As from aqueous solutions. XAS measurements at the Fe K-edge and TEM identified maghemite as the main iron phase of the SPION nanoparticles (average size ~13 nm).

Batch adsorption experiments of As(V) at 800 $mg \cdot L^{-1}$ showed a ~63% increase of adsorption capacity when loading 2.6 wt.% mass fraction of SPION in the cube-sponge. Experimental determination of the adsorption thermodynamic parameters indicated that the As(V) adsorption on the composite material is a spontaneous and exothermic process. As K-edge XAS results confirmed that the adsorption enhancement on the composite was due to the nanoparticles presence. In addition, adsorbed As(V) kept its oxidation state and formed a binuclear corner-sharing complex with SPION. The composite adsorbent also showed a good regeneration property.

Batch adsorption experiments of As(III) showed that the 2.6 wt.% of SPION loaded in the sponge outperforms the adsorption of the unsupported SPION. In this concern, the adsorption capacity obtained for the composite was ~14

times larger than the one of the unsupported SPION, thus revealing the SPION aggregation drop when loaded at the sponge with consequent enhanced surface contact. The adsorption of As(III) on this composite adsorbent was best described by the Temkin isotherm model and the pseudo-second order kinetic model which indicates that chemisorption is controlling the speed of the adsorption process. Experimental determination of thermodynamic parameters, $\Delta H°$ and $\Delta G°$, indicated that As(III) adsorption on the composite adsorbent was spontaneous and endothermic, as the already observed As(III) adsorption on the unsupported SPION. Arsenic K-edge XAS results revealed that the adsorbed As(III) was partially oxidized to less toxic As(V) by hydroxyl free radical (•OH) generated from Fe(III) and hydroxyl groups. Besides, the oxidation of adsorbed As(III) on the composite was more favorable at lower temperatures and no difference was found as a function of the cube depth.

For As removal on fixed-bed column experiments, several parameters of the breakthrough experiments such as initial concentration and the adsorbent material (sponge and sponge-loaded SPION) had a greater effect than the flow rate and/or the temperature. In both column systems (lab scale and pilot plant), the As(V) removal rates were always higher than 95% for all the operating parameters studied. The results obtained for the composite material, sponge-loaded SPION, indicated that loading 2.6 wt.% SPION on the commercial cube sponge results in a 96% and 97% increment in the number of bed volumes and adsorption capacity at breakthrough point, respectively, respect to sponge. For low concentrated As solutions, which are closer to more realistic polluted environmental scenarios, 1 $mg \cdot L^{-1}$, the maximum desorption concentrations obtained for both systems were higher than 100 $mg \cdot g^{-1}$. Hence, we were able to concentrate the inlet solution by 100 times which is rather relevant for industrial applications. All these results proved that both adsorbents, sponge and sponge-loaded SPION, have a great As adsorption

performance when used as fixed-bed in both laboratory columns and pilot plant systems.

For B removal, the challenge is to overcome the reported low adsorption capacity. In this study, hierarchical alumina microspheres (HAM) were successfully synthesized by microwave-assisted co-precipitation method and used to remove boron from aqueous solutions. SEM, TEM and XRD analysis showed that synthesized HAM is hollow γ-Al_2O_3 particles with a fluffy and porous dandelion shape and an average size of 1.5 μm. Adsorption data were fitted well to the Langmuir isotherm, indicating a single-layer homogeneous adsorption, and Pseudo-second order model, suggesting a chemical adsorption to control the related adsorption rate. The theoretical maximum capacity calculated by Langmuir was 138.50 $mg \cdot g^{-1}$, which is, to our knowledge, higher than the adsorption capacities previously reported. Experimental determination of the adsorption thermodynamic parameters by varying the adsorption temperature indicated the adsorption of boron on HAM to be an exothermic and non-spontaneous process. HAM also showed high adsorption affinity and excellent selectivity towards boron in an aqueous solution, even in the presence of competitive salt ions, metal ions, anions and high ion strength. In addition, the adsorbent particles could be recyclable up to five cycles without a considerable decrease in the boron removal efficiency.

Resumen

La investigación llevada a cabo en este proyecto de Tesis se basa en el desarrollo de nuevos materiales y procedimientos de adsorción para mejorar la eficiencia de eliminación de los contaminantes oxianiones de las aguas contaminadas, en particular el arsénico (As) y el boro (B), para implementar procedimientos que permitan cumplir la regulación actual sobre la calidad del agua.

Para la eliminación de As, se han descrito muchos adsorbentes con alta capacidad de adsorción y buena selectividad, aunque la mayoría de ellos están en forma de polvo y tienen una aplicabilidad industrial bastante limitada. En este estudio, se modificó un adsorbente comercial de celulosa de celda abierta en forma de cubo mediante la coprecipitación in situ de nanopartículas de óxido de hierro superparamagnético (SPION) y se utilizó para eliminar As de soluciones acuosas. Las medidas XAS en el borde K del Fe y la caracterización TEM identificaron la maghemita como la principal fase de óxido de hierro de las nanopartículas de SPION (tamaño medio ~13 nm).

Los experimentos de adsorción por lote de As(V) a 800 $mg \cdot L^{-1}$ mostraron un aumento de la capacidad de adsorción de ~63% al cargar una fracción de masa de 2,6 wt.% de SPION en el cubo-esponja. La determinación experimental de los parámetros termodinámicos de adsorción indicó que la adsorción de As(V) en el material compuesto es un proceso espontáneo y exotérmico. Los resultados del XAS del borde K del As confirmaron que la mejora de la adsorción en el material compuesto se debía a las nanopartículas. Además, el As(V) adsorbido no se redujo a As(III), que es más tóxico, y formó un complejo binuclear de esquina con SPION. El adsorbente compuesto también mostró una buena propiedad de regeneración.

Los experimentos de adsorción por lote de As(III) mostraron que el 2,6 wt.% de

SPION cargado en la esponja supera la adsorción del SPION sin soporte. Normalizando por la fracción de masa del SPION, la capacidad de adsorción obtenida para el compuesto fue ~14 veces mayor que la del SPION sin soporte. La adsorción de As(III) en este adsorbente compuesto se describió mejor mediante el modelo de isoterma de Temkin y el modelo cinético de pseudo-segundo orden, lo que indica que la quimisorción controla la velocidad del proceso de adsorción. El análisis de los parámetros termodinámicos, $\Delta H°$ y $\Delta G°$, indicó que la adsorción de As(III) en el adsorbente compuesto mantuvo las mismas propiedades, espontáneas y endotérmicas, que el SPION sin soporte. Los resultados del XAS del borde K del As revelaron que el As(III) adsorbido se oxidó parcialmente a As(V), menos tóxico, por el radical libre hidroxilo (•OH) generado a partir del Fe(III) y los grupos hidroxilo. Además, la oxidación del As(III) adsorbido en el composite fue más favorable a bajas temperaturas y no se encontraron diferencias en función de la profundidad del cubo.

En los experimentos con columnas de lecho fijo de As, varios parámetros de los experimentos de ruptura, como la concentración inicial y el material adsorbente (esponja y SPION cargado con esponja), tuvieron un efecto mayor que el caudal y/o la temperatura. En ambos sistemas de columnas (a escala de laboratorio y a nivel de planta piloto), las tasas de eliminación de As(V) fueron siempre superiores al 95% para todos los parámetros de funcionamiento estudiados. Los resultados obtenidos para el material compuesto, SPION cargado con esponja, indicaron que la carga de 2,6 wt.% de SPION en la esponja cúbica comercial da lugar a un incremento del 96% y 97% en el número de volúmenes de lecho y la capacidad de adsorción en el punto de ruptura, respectivamente, respecto a la esponja. Para soluciones de As poco concentradas, que se acercan a escenarios ambientales contaminados más realistas, 1 $mg \cdot L^{-1}$, las concentraciones máximas de desorción obtenidas para ambos sistemas fueron superiores a 100 $mg \cdot g^{-1}$. Por lo tanto, pudimos concentrar la solución de entrada en 100 veces, lo que es

bastante relevante para las aplicaciones industriales. Todos estos resultados demostraron que ambos adsorbentes, la esponja y el SPION cargado con esponja, tienen un gran rendimiento de adsorción cuando se utilizan como lecho fijo tanto en columnas de laboratorio como en sistemas de planta piloto.

Para la eliminación de B, el reto a superar es la baja capacidad de adsorción. En este estudio, se sintetizaron con éxito microesferas jerárquicas de alúmina (HAM) mediante el método de coprecipitación asistida por microondas y se utilizaron para eliminar el boro de soluciones acuosas. Los análisis SEM, TEM y XRD mostraron que las HAM sintetizadas son partículas huecas de γ-Al_2O_3 con una forma de diente de león poroso y un tamaño medio de 1,5 μm. Los datos de adsorción se ajustaron bien a la isoterma de Langmuir y al modelo de pseudo-segundo orden, indicando una adsorción homogénea de una sola capa y que la adsorción química era el paso controlador. La capacidad máxima teórica calculada por Langmuir fue de 138,50 $mg \cdot g^{-1}$, que es, hasta donde sabemos, superior a las capacidades de adsorción reportadas previamente en la literatura. La determinación experimental de los parámetros termodinámicos de adsorción mediante la variación de la temperatura de adsorción indicó que la adsorción de boro sobre HAM es un proceso exotérmico y no espontáneo. El HAM también mostró una alta afinidad de adsorción y una excelente selectividad hacia el boro en una solución acuosa, incluso en presencia de iones salinos competitivos, iones metálicos, aniones y alta fuerza iónica. Además, las partículas adsorbentes podían ser recicladas hasta cinco ciclos sin una disminución considerable de la eficiencia de eliminación del boro.

Content

ACKNOWLEDGMENT V

SUMMARY VII

Resumen XI

Chapter 1: General introduction 1

1.1 Background 3

1.2 Problem description 3

1.3 Bullet points for each case of study: As and B 5

1.4 Reference 6

Part I: Arsenic 9

Chapter 2: Arsenic: sources, toxicity, chemistry and removal methods 11

2.1. Arsenic sources and related problems 13

2.2. The standard of arsenic 14

2.3. Chemistry of arsenic in aqueous solution 14

2.4. Arsenic removal methods 15

2.5. Adsorbents used for arsenic removal 16

2.6. Previous studies in our group 17

2.7. Objectives 20

2.8. Reference 21

Chapter 3: Adsorbents: synthesis and characterizations 31

3.1. Materials and chemical reagents 33

3.2 Pre-treatment of sponge 33

3.3. Synthesis of SPION and cube-loaded SPION 34

3.4. Characterizations of the adsorbents 34

3.4.1 SEM and TEM 35
3.4.2 FT-IR 38
3.4.3 XRD 39
3.4.4 Fe K-edge XANES measurements 40
3.5. Conclusions 42
3.6. Reference 43
Chapter 4: As(V) adsorption behavior and mechanism studies by cube sponge-loaded SPION 45
4.1. Materials and methodology 47
4.1.1 Chemical reagent 47
4.1.2 Adsorption experiments 47
4.1.3 Adsorption-desorption cycle experiments 48
4.1.4 Determination of As(V) concentration by UV-Visible 48
4.1.5 As K-edge XAS measurements 49
4.1.6 As K-edge XAS analysis 50
4.2. Adsorption behaviors 50
4.3. Adsorption isotherm and kinetic study 54
4.3.1 Isotherm modeling 54
4.3.2 Kinetic modeling 55
4.4. Thermodynamics analysis 57
4.5. Chemical state of As determined by XAS 59
4.6. Life-cycle investigation 64
4.7. Conclusions 65
4.8. Reference 66

Chapter 5: As(III) adsorption-oxidation mechanism studies on cube sponge-loaded SPION 71
5.1. Materials and methodology 73
5.1.1 Chemical reagent 73
5.1.2 Adsorption experiments 73
5.1.3 Isotherm and kinetic models 74
5.1.4 Determination of As(III) concentration by UV-Visible 74
5.1.5 As K-edge XAS measurements 75
5.1.6 As K-edge XAS peak fitting analysis 76
5.2. Adsorption behaviors 79
5.3. Adsorption isotherm and kinetic study 82
5.3.1 Isotherm modeling 82
5.3.2 Kinetic modeling 84
5.4. Thermodynamics analysis 86
5.5. Compare of the adsorption capacity with similar adsorbent system 87
5.6. As K-edge XAS measurements 88
5.7. Conclusions 94
5.8. Reference 95
Chapter 6: Arsenic fixed-bed column adsorption study 99
6.1. Fixed-bed adsorption system 101
6.2. Arsenic adsorption by using laboratory fixed-bed column 102
6.2.1. Effect of different initial concentrations 103
6.2.2. Effect of different flow rates 105
6.2.3. Effect of different temperatures 106

6.2.4. Continue adsorption-thermo desorption experiments.....108
6.3. Arsenic adsorption and desorption by pilot plant.....110
6.3.1. Effect of different initial concentrations 111
6.3.2. Compare of the sponge and sponge-loaded SPION.....112
6.4. Compare of column and pilot plant adsorption.....114
6.5. Conclusions.....116
6.6. Reference 118
Chapter 7: Boron adsorption by microwave-assisted synthesized HAM 125
7.1. Introduction 127
7.1.1. Boron sources and environmental pollution. 127
7.1.2. The standard of boron 128
7.1.3. Chemistry of boron in aqueous solution 128
7.1.4. Boron removal methods.....129
7.1.5. Adsorbents used for boron removal 130
7.1.6. Objectives 131
7.2. Materials and Methods.....131
7.2.1. Chemical reagents.....131
7.2.2. Microwave-assisted synthesis of HAM 132
7.2.3. Characterizations of HAM.....133
7.2.4. Detection of Boron 134
7.2.5. Adsorption and desorption experiments 134
7.2.6. Effect of competing ions and different ion strength 135
7.3. Results and discussion 136

7.3.1. Characterizations of HAM 136
7.3.2. Adsorption performance 139
7.3.3. Isotherm and kinetic study 143
7.3.4. Thermodynamic analysis 145
7.3.5. Effect of the foreign ions on the adsorption of boron 146
7.3.6. Adsorption capacity comparison with similar adsorbent systems 148
7.3.7. Adsorption-desorption study 149
7.4. Conclusions 150
7.5. Reference 152
Chapter 8: Conclusions and future perspectives 163
8.1. Conclusions 165
8.2 Future perspectives 167
Annex 169
Annex I 171
Annex II 173
Annex III 175
Reference 176

Chapter 1: General introduction

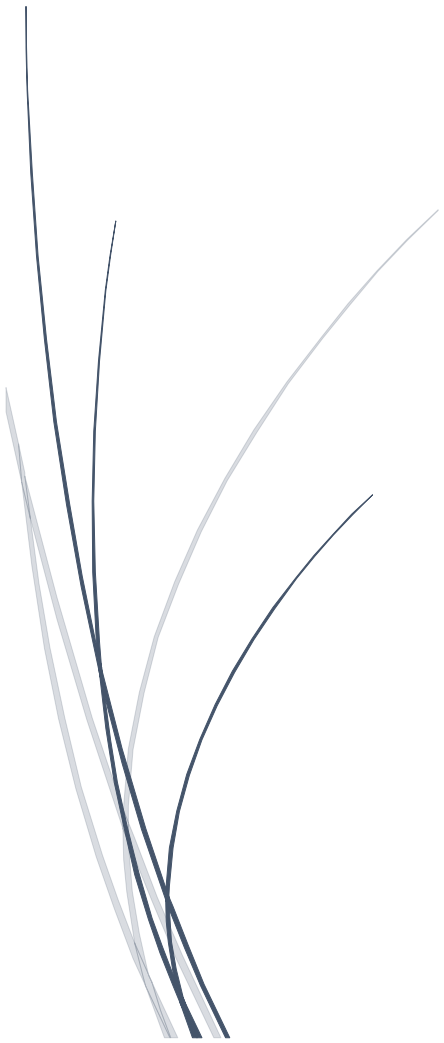

1.1 Background

Oxyanions are polyatomic negatively charged ions containing oxygen with the general formula $A_xO_y^{z-}$, where A denotes a chemical element and O denotes oxygen [1]. Arsenic (As), boron (B), selenium (Se), antimony (Sb) and chromium (Cr), among others, are common oxyanions that are found in various wastewater [2]. In addition, oxyanions in wastewater are difficult to break down like organic pollutants, but only to change their physical and chemical forms [3]. Thus, these elements can be harmful to human health not only through direct exposure to contaminated water but also through exposure to the food chains enriched with these elements.

Oxyanions are released into the environment by both natural processes and anthropogenic sources [4]. Although natural processes such as soil weathering and volcanic eruption introduce these elements into the environment, the main contribution comes from industrial activities [5]. These elements are widely used in many industrial processes, such as mining, electroplating, electrolysis, petroleum refining, agricultural chemicals, glass manufacturing [6]. The waste derived from this industrial use has not only contributed to the increment in environmental pollution but also caused the loss of valuable resources as the water and the elements themselves. Considering the toxic and carcinogenic properties of these oxyanions, their effective elimination from polluted water is becoming an important issue for environmental and public health protection.

1.2 Problem description

Despite the removal of these oxyanion pollutants from aqueous solutions is very important to the environment and human health, the amount of studies devoted to this topic are still much lower than those performed on cationic pollutants such as Hg and Pb [1].

Considering the research status of this topic as described in corresponding chapters, As and B were chosen as the target elements in this study.

Arsenic is a highly toxic and carcinogenic element. Even exposure to trace concentrations of As in long term can cause skin, lung, bladder cancers [7]. The World Health Organization (WHO) has established a maximum concentration of As in drinking water of 10 $\mu g \cdot L^{-1}$ [8,9]. The poisoning of As has occurred many times throughout history and remains a concern over large parts of the world and continues to threaten the safety of human life and health.

Boron is an essential element for humans, animals and plants. The concentration range between B deficiency and its toxicity is very narrow, it becomes hazardous for organisms when the amount is slightly higher and toxic effects caused by the excess are more common than boron deficiency in the environment [10]. Excess of B may damage the cardiovascular, central nervous and reproductive systems in the long-term uptake [11]. Since a series of environmental and health issues caused by B has been found, World Health Organization (WHO) established a guideline value for the boron limit to be 2.4 $mg \cdot L^{-1}$ in drinking water [12].

Various methods for treating oxyanions pollutants contaminated water have been reported, such as precipitation, oxidation, extraction, ion exchange, adsorption and membrane techniques [13]. All these methods have their advantages and disadvantages [14]. When considering the low concentration property of these wastewaters, adsorption is considered to be one of the most promising methods among all the techniques because of its advantages of being fast, easy to operate, environmentally friendly and cost-effective [15–17]. The core part of the adsorption is the adsorbents. Although many efforts have been made by researchers around the world, ideal adsorbents with high adsorption capacity, good selectivity, promising to scale up to industrial use still need to

design and develop.

1.3 Bullet points for each case of study: As and B

Considering the previous studies of As removal in our group, the main aims of this research for As and B elements are different. The brief content is listed below, the detailed introduction is included in their corresponding chapters. For As, the main aim would be the successful synthesis of the cube-shaped sponge-loaded SPION, As(III) and As(V) adsorption behavior study, the coordination environment study of adsorbed As by using XAS technique, As(V) adsorption behavior study in experimental column and pilot plant experiments. For B, the main aim would be the successful synthesis of hierarchical alumina microspheres (HAM) with high adsorption capacity and good selectivity, and their adsorption behavior study.

1.4 Reference

[1] E. Weidner, F. Ciesielczyk, Removal of Hazardous Oxyanions from the Environment Using Metal-Oxide-Based Materials, Materials (Basel). 12 (2019) 927. https://doi.org/10.3390/ma12060927.

[2] R. Li, J.J. Wang, L.A. Gaston, B. Zhou, M. Li, R. Xiao, Q. Wang, Z. Zhang, H. Huang, W. Liang, H. Huang, X. Zhang, An overview of carbothermal synthesis of metal–biochar composites for the removal of oxyanion contaminants from aqueous solution, Carbon N. Y. 129 (2018) 674–687. https://doi.org/10.1016/j.carbon.2017.12.070.

[3] B.A. Marinho, R.O. Cristóvão, R.A.R. Boaventura, V.J.P. Vilar, As(III) and Cr(VI) oxyanion removal from water by advanced oxidation/reduction processes—a review, Environ. Sci. Pollut. Res. 26 (2019) 2203–2227. https://doi.org/10.1007/s11356-018-3595-5.

[4] C.B. Tabelin, T. Igarashi, M. Villacorte-Tabelin, I. Park, E.M. Opiso, M. Ito, N. Hiroyoshi, Arsenic, selenium, boron, lead, cadmium, copper, and zinc in naturally contaminated rocks: A review of their sources, modes of enrichment, mechanisms of release, and mitigation strategies, Sci. Total Environ. 645 (2018) 1522–1553. https://doi.org/10.1016/j.scitotenv.2018.07.103.

[5] S. Muthu Prabhu, K. Pandi, S.S. Elanchezhiyan, J. Choi, G. Paruthimal Kalaignan, C.M. Park, Ethylene glycol-induced metal alkoxides via phase-transfer catalyst as multi-talented adsorbents for boosted adsorption performance of toxic anions/oxyanions from waters, Sep. Purif. Technol. 235 (2020) 116247. https://doi.org/10.1016/j.seppur.2019.116247.

[6] S. Benzer, Concentrations of Arsenic and Boron in Water, Sediment and the Tissues of Fish in Emet Stream (Turkey), Bull. Environ. Contam. Toxicol. 98 (2017) 805–810. https://doi.org/10.1007/s00128-016-1996-z.

[7] G. Ghosh, D.K. Mukhopadhyay, Human Health Hazards Due to Arsenic and Fluoride Contamination in Drinking Water and Food Chain, in: Groundw. Dev. Manag., Springer International Publishing, Cham, 2019: pp. 351–369. https://doi.org/10.1007/978-3-319-75115-3_15.

[8] B.A. Roggenbeck, M. Banerjee, E.M. Leslie, Cellular arsenic transport pathways in mammals, J. Environ. Sci. (China). 49 (2016) 38–58.

https://doi.org/10.1016/j.jes.2016.10.001.

[9] E. Shaji, M. Santosh, K. V. Sarath, P. Prakash, V. Deepchand, B. V. Divya, Arsenic contamination of groundwater: A global synopsis with focus on the Indian Peninsula, Geosci. Front. 12 (2021) 101079. https://doi.org/10.1016/j.gsf.2020.08.015.

[10] Y. Hua, T. Zhou, G. Ding, Q. Yang, L. Shi, F. Xu, Physiological, genomic and transcriptional diversity in responses to boron deficiency in rapeseed genotypes, J. Exp. Bot. 67 (2016) 5769–5784. https://doi.org/10.1093/jxb/erw342.

[11] E.D. Farfán-García, N.T. Castillo-Mendieta, F.J. Ciprés-Flores, I.I. Padilla-Martínez, J.G. Trujillo-Ferrara, M.A. Soriano-Ursúa, Current data regarding the structure-toxicity relationship of boron-containing compounds, Toxicol. Lett. 258 (2016) 115–125. https://doi.org/10.1016/j.toxlet.2016.06.018.

[12] B. Tomaszewska, M. Bodzek, Desalination of geothermal waters using a hybrid UF-RO process. Part II: Membrane scaling after pilot-scale tests, Desalination. 319 (2013) 107–114. https://doi.org/10.1016/j.desal.2013.01.030.

[13] Y. John, V.E. David, D. Mmereki, A Comparative Study on Removal of Hazardous Anions from Water by Adsorption: A Review, Int. J. Chem. Eng. 2018 (2018) 1–21. https://doi.org/10.1155/2018/3975948.

[14] M. Gaouar-Yadi, K. Tizaoui, N. Gaouar-Benyelles, B. Benguella, Efficient and eco-friendly adsorption using low-cost natural adsorbents in waste water treatment, Indian J. Chem. Technol. 23 (2016) 204–209. http://hdl.handle.net/123456789/34259.

[15] S. Pathan, S. Bose, Arsenic Removal Using “green” Renewable Feedstock-Based Hydrogels: Current and Future Perspectives, ACS Omega. 3 (2018) 5910–5917. https://doi.org/10.1021/acsomega.8b00236.

[16] H. Zeng, L. Zhai, T. Qiao, Y. Yu, J. Zhang, D. Li, Efficient removal of As(V) from aqueous media by magnetic nanoparticles prepared with Iron-containing water treatment residuals, Sci. Rep. 10 (2020) 9335. https://doi.org/10.1038/s41598-020-65840-1.

[17] T. Sumathi, G. Alagumuthu, Adsorption studies for arsenic removal using activated Moringa oleifera, Int. J. Chem. Eng. 2014 (2014) 430417. https://doi.org/10.1155/2014/430417.

Part I: Arsenic

Chapter 2: Arsenic: sources, toxicity, chemistry and removal methods

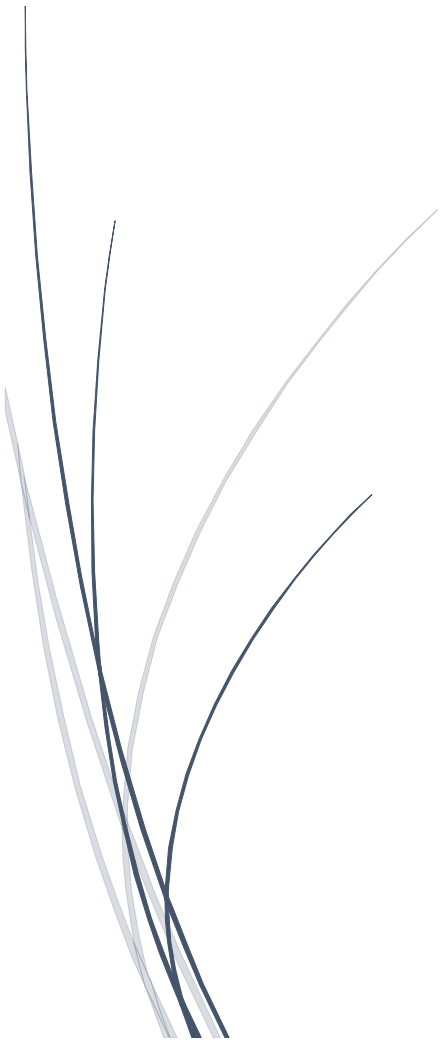

Arsenic (As) is a chemical element with the symbol As and an atomic number of 33 [1]. It is a metalloid, possessing both metallic and nonmetallic properties, and is the third element in Group VA of the periodic table [2]. As is a natural component of the earth's crust and is widely distributed throughout the environment in air, water and land [3,4]. In recent years, As contamination has become a major concern for environmental pollution and human health due to its high toxicity and carcinogenicity [5,6].

2.1. Arsenic sources and related problems

Arsenic is released into the environment from both natural and anthropogenic sources [7]. Although natural processes such as soil weathering and volcanic eruption introduce As into the environment, industrial processes are the primary source of As in the environment [8]. It is widely used in industry as alloy agents in the manufacturing of electronic components, as well as an additive in the processing of glass, pigments, textiles, paper, metal adhesives, wood preservatives, and ammunition [9–11]. According to statistics, 70% of global As production is used for wood preservation, 22% for pesticides and the rest for glass and non-ferrous alloys, etc [12,13].

Arsenic is a highly toxic element [14,15]. Short-term exposure to high concentrations of As can be fatal, while long-term exposure to trace concentrations of As can cause skin, lung, bladder cancers [16,17]. Arsenic can be transferred into the food chain through grains irrigated by As-containing wastewater and through seafood living in As-containing wastewater [18,19]. Exposure to contaminated drinking water is another direct pathway to humans [20].

Arsenic poisoning has occurred many times throughout history and remains a concern over large parts of the world and continues to threaten the safety of

human life and health [8,21]. In 1900, As-contaminated beer caused the poisoning of 6,000 people and some 71 deaths in northern England [22]. In 1995, Morinaga milk produced in Japan contained high levels of As, causing food poisoning in about 13,000 infants and killing 130 of them [23]. In recent years, it is estimated that tens of millions of people in Bangladesh have been reached by As-contaminated water, resulting in an estimated 24,000 deaths per year [24,25].

2.2. The standard of arsenic

The World Health Organization (WHO) has established a maximum concentration of As in drinking water of 10 $\mu g \cdot L^{-1}$ [26,27]. Unfortunately, there are still many people exposed to high levels of As pollution in some parts of the world, particularly in developing countries, such as India, Argentina, China, Pakistan, and Bangladesh [28,29]. As a result, more than 200 million people in the world are exposed to unacceptable levels of As in their drinking water [30]. Therefore, the effective removal of As from water is particularly important for environmental protection and human health.

2.3. Chemistry of arsenic in aqueous solution

Arsenic is a metalloid element, which means that it displays some properties of metal and non-metal at the same time [31]. It exists in both inorganic and organic forms in the environment [32,33]. Inorganic forms are more common and toxic.

In water, As is mostly found as oxyanions of trivalent arsenite, As(III), or pentavalent arsenate, As(V), [34]. As speciation in aqueous solutions is mostly controlled by redox potential (Eh) and pH [35]. The redox potential (Eh)-pH diagram for inorganic As is shown in Figure 2.1. Table 2.1 shows the dissociation constants of inorganic As compounds in water.

Under reducing conditions, As(III) is the dominant form [36,37]. On the other hand, As(V) is the thermodynamically stable form that generally predominates in oxic surface waters [38]. As for different pH values, As(III) compound exists as uncharged H_3AsO_3 below pH 9.2, negative $H_2AsO_3^-$ from pH 9.2~12.2 and $HAsO_4^{2-}$ from pH 12.2 ~13.4; however, As(V) exists as uncharged H_3AsO_4 below pH 2.2, negative $H_2AsO_4^-$ from pH 2.2~7.0 and negative $HAsO_4^{2-}$ from pH 7.0~11.5.

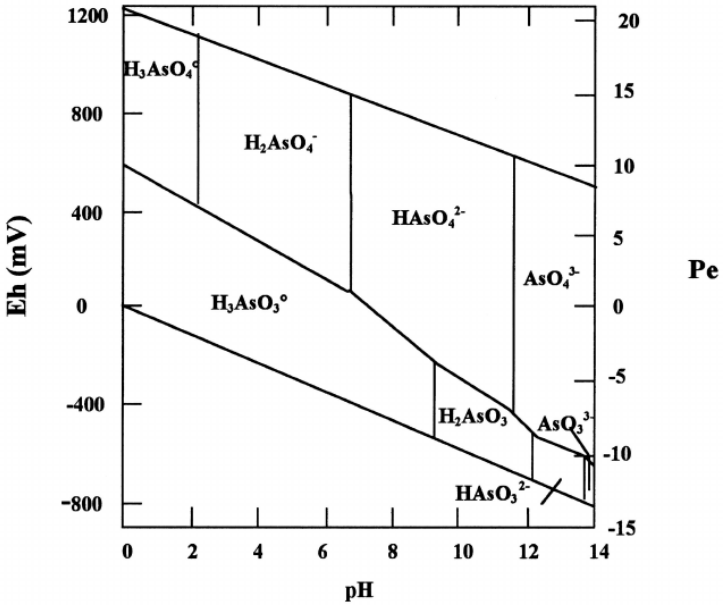

Figure 2.1. Eh-pH diagram for the system As-water at 25°C, modified from [39].

Table 2.1. Dissociation constants of inorganic arsenic compounds [40].

Compound	Pk_1	Pk_2	Pk_3
H_3AsO_3	9.2	12.2	13.4
H_3AsO_4	2.2	7.0	11.5

2.4. Arsenic removal methods

In the past decades, there are numerous technologies adopted for As removal

from contaminated water. The conventional methods are chemical precipitation [41,42], solvent extraction [43,44], ion exchange [45,46], electrodialysis [47,48], membrane separation [49,50], as well as adsorption [51,52].

All these methods have their advantages and disadvantages [53]. When considering the low concentration property, adsorption is considered to be one of the most promising methods among all the techniques because of its advantages of being fast, easy to operate, environmentally friendly and cost-effective [54–56].

2.5. Adsorbents used for arsenic removal

An ideal adsorbent for water remediation should be non-toxic, has excellent chemical resistance, and very low solubility in water. Many types of adsorbents have been reported for As removal, such as biomass [57], metal oxides nanoparticles (especially iron oxide) [58], polyurethane foam [59], graphene [60] and graphene oxide [61].

In recent years, magnetic iron oxide nanoparticles have attracted attention due to their specific affinity to As over other metals [62], large specific surface area [63] and easy separation from aqueous solution [64,65]. Various adsorption studies using magnetic iron oxide-based adsorbents for As removal have been reported [66–69]. However, the aggregation of nanoparticles in water greatly affects their adsorption performance [17,70,71]. Liu et al [17]. synthesized magnetic iron oxide nanoparticles for As removal with an average diameter of 34 nm; however, particles aggregate a lot under adsorption conditions reaching sizes over μm-size.

Some traditional materials like activated carbon [72], fly ash [73], sand [74,75], and biomass [76] were used as supports to reduce the aggregation and they

obtained good adsorption results in batch experiments. However, one of the drawbacks of these composite materials is that they are in powder form. This means that they are not suitable for direct industrial use and, in addition, they are very difficult to recover when used for on-site environmental remediation applications. Indeed, when used in a fixed-bed column, the powder adsorbents tend to clog the column and restrict the flow rate which limits their practical use. Alternatively, powders have been loaded on membranes and hybrid methods have been developed by combining adsorption with membrane filtration [77,78]. This approach greatly reduces the aggregation of nanoparticulate adsorbents; however, this methodology increases the cost of the initial nanoparticulate adsorbent, and it has other disadvantages such as membrane fouling that must be taken into consideration.

In conclusion, although many efforts have been made by researchers around the world, ideal adsorbents with high adsorption capacity, good selectivity, promising to scale up to industrial use for As removal still need to design and develop.

2.6. Previous studies in our group

As adsorption on superparamagnetic iron oxide nanoparticles (SPION) and commercial Metalzorb® sponge (previously named Forager® sponge) loaded SPION has been studied by different researchers in our group. Previously works were devoted their efforts in optimizing the design, synthesis, and usage of SPION to improve the structural stability, adsorption capacity, and adsorption selectivity [15–17]. One of the main drawbacks of nanoparticles is their easy aggregation when they are suspended in water. To overcome this issue, researchers in our group chose a commercial open-celled cellulose sponge as the support of SPION instead of traditional support materials such as sand [74,75], fly ash [79], and biomass [80,81]. The sponge has low

impedance of diffusion and it is light in weight. When used in a column, flow rates of three bed volumes per minute can be obtained at hydrostatic pressures only ~60 cm above the bed and without any additional pressurization. These properties make this porous material a good candidate for supporting nanoparticles in industrial water remediation applications. Good adsorption behaviors in batch experiments have been reported [82,83].

Morillo et al [84]. studied the As(III) and As(V) adsorption onto superparamagnetic iron oxide nanoparticles (SPION). The maximum adsorption for arsenate on SPION was obtained in an acid media (pH 3.6), while arsenite adsorption is not pH-dependent. For both As species, SPION showed a high selectivity while in presence of interfering. In order to increase the adsorption capacity of SPION, 3-mercaptopropionic acid was selected to do the modification. The maximum adsorption capacities of 3-MPA coated SPION are 1.03 mmol As/g SPION and 1.60 mmol As/g SPION for arsenite and arsenate, respectively. To overcome the drawbacks of aggregation, SPION was loaded on powder sponge. After loading, the adsorption capacities of composite material were 2.11 mmol As/g SPION and 12.09 mmol As/g SPION for arsenite and arsenate, respectively, much higher than those for unsupported SPION.

Liu et al [85]. studied the As adsorption-desorption study by using the powder sponge-loaded SPION composite material. Their research is focused on the As(V) adsorption-desorption process in continuous mode together with the adsorbent regeneration by thermal or redox processes, and a combination of both methods (thermo-tunning of redox potential). Their results proved that the reagent-less process of regeneration by thermo-tunning of redox potential was successfully developed.

Verdugo et al [86]. continue the study of developing a reagent-less system for

the regeneration of adsorbents. The main idea is to reduce the adsorbed As(V) to As(III) by using electrolytic technique and finally desorbed from adsorbents. When using the combination of Sn and Sn coating on stainless steel mesh as working and counter electrode, respectively, present the best results (60% of As(V) reduction).

Considering the previous results, one of the main limitations is that the authors used those composite materials in powdered form. Hence, when used in adsorption columns for industrial applications, they would limit the flow rate of the solution, even block the column and blocking the flow. The separation of powdered adsorbents from wastewater is a tedious job and requires sophisticated instrumentations that are hardly available in developing countries. This reduces the feasibility of its implementation at those places with serious contamination issues [87]. In this study, we propose to use SPION supported on the commercial cube-shaped open-celled cellulose sponge (hereafter referred to as "sponge-loaded SPION") as a composite material for the removal of As from aqueous solution. Fixed-bed lab column and pilot plant experiments were also performed to investigated the potential of the industrial applications.

Although the study of the macroscopic adsorption behavior of As onto SPION and sponge-loaded SPION has been widely studied by previous researchers, information about the oxidation state and coordination environment of As after being adsorbed is still missing. Indeed, the oxidation state and speciation of As determine its toxicity and mobility in the environment [88]. Thus, due to the different toxic risks associated with the release of As species [89], it is important to understand the fate of adsorbed As and to discern any possible redox processes that may take place upon adsorption. There have been some reports on the oxidation of As(III) to As(V) after adsorbed by iron-based adsorbents [90,91]. However, concerning environmental influences (such as temperatures,

different parts of adsorbent) during this process are few reported. In this study, As K-edge synchrotron-based X-ray absorption spectroscopy (XAS) measurements were performed to get a better insight of the adsorption process at the molecular scale.

2.7. Objectives

In this study, we propose a commercial cube-shaped open-celled cellulose sponge to support SPION as a composite adsorbent material for the removal of As from aqueous solutions. The main objectives are as follows:

- Successful synthesis and appropriate characterizations of the cube sponge-loaded SPION composite adsorbent.
- Characterization of As(III) and As(V) adsorption on the composite and comparison with adsorption on both sponge and SPION individual adsorbents.
- Exploring the coordination environment and potential redox transformation of adsorbed As on different adsorbents (SPION, sponge, sponge-loaded SPION) by using XAS technique.
- Exploring the adsorption performance and the possibility of industrial applications by performing fixed-bed column adsorption experiments.
- Develop a reagent-less As adsorption-desorption system and exploring the possibility of thermal desorption instead of chemical desorption.

2.8. Reference

[1] L.Y. Chai, Arsenic pollution control in nonferrous metallurgy, Springer Singapore, Singapore, 2019. https://doi.org/10.1007/978-981-13-6721-2.

[2] K.A. James, J.R. Meliker, J.O. Nriagu, Arsenic, in: Int. Encycl. Public Heal., Elsevier, 2016: pp. 170–175. https://doi.org/10.1016/B978-0-12-803678-5.00025-4.

[3] X. He, P. Li, Y. Ji, Y. Wang, Z. Su, V. Elumalai, Groundwater Arsenic and Fluoride and Associated Arsenicosis and Fluorosis in China: Occurrence, Distribution and Management, Expo. Heal. 12 (2020) 355–368.https://doi.org/10.1007/s12403-020-00347-8.

[4] I. Palma-Lara, M. Martínez-Castillo, J.C. Quintana-Pérez, M.G. Arellano-Mendoza, F. Tamay-Cach, O.L. Valenzuela-Limón, E.A. García-Montalvo, A. Hernández-Zavala, Arsenic exposure: A public health problem leading to several cancers, Regul. Toxicol. Pharmacol. 110 (2020) 104539. https://doi.org/10.1016/j.yrtph.2019.104539.

[5] P. Mandal, An insight of environmental contamination of arsenic on animal health, Emerg. Contam. 3 (2017) 17–22. https://doi.org/10.1016/j.emcon.2017.01.004.

[6] M. Argos, H. Ahsan, J.H. Graziano, Arsenic and human health: Epidemiologic progress and public health implications, Rev. Environ. Health. 27 (2012) 191–195. https://doi.org/10.1515/reveh-2012-0021.

[7] M.Z. Alam, M.A. Hoque, G.J. Ahammed, R. McGee, L. Carpenter-Boggs, Arsenic accumulation in lentil (Lens culinaris) genotypes and risk associated with the consumption of grains, Sci. Rep. 9 (2019) 1–9. https://doi.org/10.1038/s41598-019-45855-z.

[8] J. Bundschuh, J. Schneider, M.A. Alam, N.K. Niazi, I. Herath, F. Parvez, B. Tomaszewska, L.R.G. Guilherme, J.P. Maity, D.L. López, A.F. Cirelli, A. Pérez-Carrera, N. Morales-Simfors, M.T. Alarcón-Herrera, P. Baisch, D. Mohan, A. Mukherjee, Seven potential sources of arsenic pollution in Latin America and their environmental and health impacts, Sci. Total Environ. 780 (2021) 146274. https://doi.org/10.1016/j.scitotenv.2021.146274.

[9] C. Wang, L. Boithias, Z. Ning, Y. Han, S. Sauvage, J.M. Sánchez-Pérez, K. Kuramochi, R. Hatano, Comparison of Langmuir and Freundlich adsorption equations within the SWAT-K model for assessing potassium environmental losses at basin scale, Agric.

Water Manag. 180 (2017) 205–211. https://doi.org/10.1016/j.agwat.2016.08.001.

[10] P. Kumarathilaka, S. Seneweera, A. Meharg, J. Bundschuh, Arsenic speciation dynamics in paddy rice soil-water environment: sources, physico-chemical, and biological factors - A review, Water Res. 140 (2018) 403–414. https://doi.org/10.1016/j.watres.2018.04.034.

[11] V. Reis, A.C. Duarte, Occurrence, distribution, and significance of arsenic speciation, in: Compr. Anal. Chem., Elsevier, 2019: pp. 1–14. https://doi.org/10.1016/bs.coac.2019.03.006.

[12] V. Bencko, F. Yan Li Foong, The history of arsenical pesticides and health risks related to the use of Agent Blue, Ann. Agric. Environ. Med. 24 (2017) 312–316. https://doi.org/10.26444/aaem/74715.

[13] A.S. Jones, J. Marini, H.M. Solo-Gabriele, N.M. Robey, T.G. Townsend, Arsenic, copper, and chromium from treated wood products in the U.S. disposal sector, Waste Manag. 87 (2019) 731–740. https://doi.org/10.1016/j.wasman.2019.03.004.

[14] G. Retamal-Morales, M. Mehnert, R. Schwabe, D. Tischler, C. Zapata, R. Chávez, M. Schlömann, G. Levicán, Detection of arsenic-binding siderophores in arsenic-tolerating Actinobacteria by a modified CAS assay, Ecotoxicol. Environ. Saf. 157 (2018) 176–181. https://doi.org/10.1016/j.ecoenv.2018.03.087.

[15] G. Abbas, B. Murtaza, I. Bibi, M. Shahid, N. Niazi, M. Khan, M. Amjad, M. Hussain, Natasha, Arsenic Uptake, Toxicity, Detoxification, and Speciation in Plants: Physiological, Biochemical, and Molecular Aspects, Int. J. Environ. Res. Public Health. 15 (2018) 59. https://doi.org/10.3390/ijerph15010059.

[16] A. Mehri, Trace elements in human nutrition (II) - An update, Int. J. Prev. Med. 11 (2020) 2. https://doi.org/10.4103/ijpvm.IJPVM_48_19.

[17] C.H. Liu, Y.H. Chuang, T.Y. Chen, Y. Tian, H. Li, M.K. Wang, W. Zhang, Mechanism of Arsenic Adsorption on Magnetite Nanoparticles from Water: Thermodynamic and Spectroscopic Studies, Environ. Sci. Technol. 49 (2015) 7726–7734. https://doi.org/10.1021/acs.est.5b00381.

[18] F.J. Zhao, P. Wang, Arsenic and cadmium accumulation in rice and mitigation strategies, Plant Soil. 446 (2020) 1–21. https://doi.org/10.1007/s11104-019-04374-6.

[19] K. Karimyan, M. Alimohammadi, A. Maleki, M. Yunesian, R.N. Nodehi, A.R.

Foroushani, The mobility of arsenic from highly polluted farmlands to wheat: Soil–Plant transfer model and health risk assessment, L. Degrad. Dev. 31 (2020) 1560–1572. https://doi.org/10.1002/ldr.3552.

[20] N.I. Khan, G. Owens, D. Bruce, R. Naidu, Human arsenic exposure and risk assessment at the landscape level: A review, Environ. Geochem. Health. 31 (2009) 143–166. https://doi.org/10.1007/s10653-008-9240-3.

[21] J.J. Steffan, E.C. Brevik, L.C. Burgess, A. Cerdà, The effect of soil on human health: an overview, Eur. J. Soil Sci. 69 (2018) 159–171. https://doi.org/10.1111/ejss.12451.

[22] I. Suay-Matallana, X. Guillem-Llobat, Poisoned Wine: Regulation, Chemical Analyses, and Spanish-French Trade in the 1930s, Ambix. 65 (2018) 99–121. https://doi.org/10.1080/00026980.2018.1452838.

[23] D. Montet, R.C. Ray, eds., Food Traceability and Authenticity, CRC Press, Boca Raton, FL : CRC Press, 2017. | Series: Food biology series | "A science publishers book.," 2017. https://doi.org/10.1201/9781351228435.

[24] Y. Li, Y. Bi, W. Mi, S. Xie, L. Ji, Land-use change caused by anthropogenic activities increase fluoride and arsenic pollution in groundwater and human health risk, J. Hazard. Mater. 406 (2021) 124337. https://doi.org/10.1016/j.jhazmat.2020.124337.

[25] S.E. Amrose, K. Cherukumilli, N.C. Wright, Chemical Contamination of Drinking Water in Resource-Constrained Settings: Global Prevalence and Piloted Mitigation Strategies, Annu. Rev. Environ. Resour. 45 (2020) 195–226. https://doi.org/10.1146/annurev-environ-012220-105152.

[26] B.A. Roggenbeck, M. Banerjee, E.M. Leslie, Cellular arsenic transport pathways in mammals, J. Environ. Sci. (China). 49 (2016) 38–58. https://doi.org/10.1016/j.jes.2016.10.001.

[27] E. Shaji, M. Santosh, K. V. Sarath, P. Prakash, V. Deepchand, B. V. Divya, Arsenic contamination of groundwater: A global synopsis with focus on the Indian Peninsula, Geosci. Front. 12 (2021) 101079. https://doi.org/10.1016/j.gsf.2020.08.015.

[28] C. Jing, J. Cui, Y. Huang, A. Li, Fabrication, characterization, and application of a composite adsorbent for simultaneous removal of arsenic and fluoride, ACS Appl. Mater. Interfaces. 4 (2012) 714–720. https://doi.org/10.1021/am2013322.

[29] M. Raessler, The Arsenic Contamination of Drinking and Groundwaters in Bangladesh: Featuring Biogeochemical Aspects and Implications on Public Health, Arch. Environ. Contam. Toxicol. 75 (2018) 1–7. https://doi.org/10.1007/s00244-018-0511-4.

[30] M.F. Naujokas, B. Anderson, H. Ahsan, H. Vasken Aposhian, J.H. Graziano, C. Thompson, W.A. Suk, The broad scope of health effects from chronic arsenic exposure: Update on a worldwide public health problem, Environ. Health Perspect. 121 (2013) 295–302. https://doi.org/10.1289/ehp.1205875.

[31] I. Ben Fekih, C. Zhang, Y.P. Li, Y. Zhao, H.A. Alwathnani, Q. Saquib, C. Rensing, C. Cervantes, Distribution of Arsenic Resistance Genes in Prokaryotes, Front. Microbiol. 9 (2018). https://doi.org/10.3389/fmicb.2018.02473.

[32] A. Sarkar, B. Paul, The global menace of arsenic and its conventional remediation - A critical review, Chemosphere. 158 (2016) 37–49. https://doi.org/10.1016/j.chemosphere.2016.05.043.

[33] S. Mishra, J. Mattusch, R. Wennrich, Accumulation and transformation of inorganic and organic arsenic in rice and role of thiol-complexation to restrict their translocation to shoot, Sci. Rep. 7 (2017) 40522. https://doi.org/10.1038/srep40522.

[34] T.S. Singh, K.K. Pant, Equilibrium, kinetics and thermodynamic studies for adsorption of As(III) on activated alumina, Sep. Purif. Technol. 36 (2004) 139–147. https://doi.org/10.1016/S1383-5866(03)00209-0.

[35] K.F. Akter, G. Owens, D.E. Davey, R. Naidu, Arsenic Speciation and Toxicity in Biological Systems, in: 2005: pp. 97–149. https://doi.org/10.1007/0-387-27565-7_3.

[36] M.R. Akanda, I.S. Kim, D. Ahn, H.J. Tae, W. Tian, H.H. Nam, B.K. Choo, B.Y. Park, In Vivo and In Vitro Hepatoprotective Effects of Geranium koreanum Methanolic Extract via Downregulation of MAPK/Caspase-3 Pathway, Evidence-Based Complement. Altern. Med. 2017 (2017) 8137627. https://doi.org/10.1155/2017/8137627.

[37] S. Das, R. Mandal, V.N. Rabidas, N. Verma, K. Pandey, A.K. Ghosh, S. Kesari, A. Kumar, B. Purkait, C.S. Lal, P. Das, Chronic Arsenic Exposure and Risk of Post Kala-azar Dermal Leishmaniasis Development in India: A Retrospective Cohort Study, PLoS Negl. Trop. Dis. 10 (2016) e0005060–e0005060. https://doi.org/10.1371/journal.pntd.0005060.

[38] H. Genç-Fuhrman, J.C. Tjell, D. McConchie, Adsorption of Arsenic from Water Using

Activated Neutralized Red Mud, Environ. Sci. Technol. 38 (2004) 2428–2434. https://doi.org/10.1021/es035207h.

[39] P. Lu, C. Zhu, Arsenic Eh–pH diagrams at 25°C and 1 bar, Environ. Earth Sci. 62 (2011) 1673–1683. https://doi.org/10.1007/s12665-010-0652-x.

[40] X. Yu, W. Cui, Q. Wang, Y. Guo, T. Deng, Speciation analysis of arsenic in samples containing high concentrations of chloride by LC-HG-AFS, Anal. Bioanal. Chem. 411 (2019) 7251–7260. https://doi.org/10.1007/s00216-019-02093-6.

[41] Z. Lu, X. Qi, X. Zhu, X. Li, K. Li, H. Wang, Highly effective remediation of high-arsenic wastewater using red mud through formation of AlAsO4@silicate precipitate, Environ. Pollut. (2021) 117484. https://doi.org/10.1016/j.envpol.2021.117484.

[42] F.G. Jahromi, A. Ghahreman, In-situ oxidative arsenic precipitation as scorodite during carbon catalyzed enargite leaching process, J. Hazard. Mater. 360 (2018) 631–638. https://doi.org/10.1016/j.jhazmat.2018.08.019.

[43] J. Guo, S. Luo, Z. Liu, T. Luo, Direct Arsenic Removal from Water Using Non-Membrane, Low-Temperature Directional Solvent Extraction, J. Chem. Eng. Data. 65 (2020) 2938–2946. https://doi.org/10.1021/acs.jced.9b00936.

[44] N. Jantunen, S. Virolainen, P. Latostenmaa, J. Salminen, M. Haapalainen, T. Sainio, Removal and recovery of arsenic from concentrated sulfuric acid by solvent extraction, Hydrometallurgy. 187 (2019) 101–112. https://doi.org/10.1016/j.hydromet.2019.05.008.

[45] B.S. Rathi, P.S. Kumar, R. Ponprasath, K. Rohan, N. Jahnavi, An effective separation of toxic arsenic from aquatic environment using electrochemical ion exchange process, J. Hazard. Mater. 412 (2021) 125240. https://doi.org/10.1016/j.jhazmat.2021.125240.

[46] C.-G. Lee, P.J.J. Alvarez, A. Nam, S.-J. Park, T. Do, U.-S. Choi, S.-H. Lee, Arsenic(V) removal using an amine-doped acrylic ion exchange fiber: Kinetic, equilibrium, and regeneration studies, J. Hazard. Mater. 325 (2017) 223–229. https://doi.org/10.1016/j.jhazmat.2016.12.003.

[47] M. Aliaskari, A.I. Schäfer, Nitrate, arsenic and fluoride removal by electrodialysis from brackish groundwater, Water Res. 190 (2021) 116683. https://doi.org/10.1016/j.watres.2020.116683.

[48] M.T. Pham, S. Nishihama, K. Yoshizuka, Effect of Operational Conditions on Arsenic

Removal from Aqueous Solution Using Electrodialysis, Solvent Extr. Ion Exch. (2021) 1–13. https://doi.org/10.1080/07366299.2021.1876987.

[49] Y. He, J. Liu, G. Han, T.-S. Chung, Novel thin-film composite nanofiltration membranes consisting of a zwitterionic co-polymer for selenium and arsenic removal, J. Memb. Sci. 555 (2018) 299–306. https://doi.org/10.1016/j.memsci.2018.03.055.

[50] S.K. Hubadillah, M.H.D. Othman, A.F. Ismail, M.A. Rahman, J. Jaafar, A low cost hydrophobic kaolin hollow fiber membrane (h-KHFM) for arsenic removal from aqueous solution via direct contact membrane distillation, Sep. Purif. Technol. 214 (2019) 31–39. https://doi.org/10.1016/j.seppur.2018.04.025.

[51] A.I.A. Sherlala, A.A.A. Raman, M.M. Bello, A. Buthiyappan, Adsorption of arsenic using chitosan magnetic graphene oxide nanocomposite, J. Environ. Manage. 246 (2019) 547–556. https://doi.org/10.1016/j.jenvman.2019.05.117.

[52] Q. Hu, Y. Liu, X. Gu, Y. Zhao, Adsorption behavior and mechanism of different arsenic species on mesoporous MnFe 2 O 4 magnetic nanoparticles, Chemosphere. 181 (2017) 328–336. https://doi.org/10.1016/j.chemosphere.2017.04.049.

[53] M. Gaouar-Yadi, K. Tizaoui, N. Gaouar-Benyelles, B. Benguella, Efficient and eco-friendly adsorption using low-cost natural adsorbents in waste water treatment, Indian J. Chem. Technol. 23 (2016) 204–209. http://hdl.handle.net/123456789/34259.

[54] S. Pathan, S. Bose, Arsenic Removal Using “green” Renewable Feedstock-Based Hydrogels: Current and Future Perspectives, ACS Omega. 3 (2018) 5910–5917. https://doi.org/10.1021/acsomega.8b00236.

[55] H. Zeng, L. Zhai, T. Qiao, Y. Yu, J. Zhang, D. Li, Efficient removal of As(V) from aqueous media by magnetic nanoparticles prepared with Iron-containing water treatment residuals, Sci. Rep. 10 (2020) 9335. https://doi.org/10.1038/s41598-020-65840-1.

[56] T. Sumathi, G. Alagumuthu, Adsorption studies for arsenic removal using activated Moringa oleifera, Int. J. Chem. Eng. 2014 (2014) 430417. https://doi.org/10.1155/2014/430417.

[57] C.T. Kamala, K.H. Chu, N.S. Chary, P.K. Pandey, S.L. Ramesh, A.R.K. Sastry, K.C. Sekhar, Removal of arsenic(III) from aqueous solutions using fresh and immobilized plant biomass, Water Res. 39 (2005) 2815–2826.

https://doi.org/10.1016/j.watres.2005.04.059.

[58] S. Kundu, A.K. Gupta, Arsenic adsorption onto iron oxide-coated cement (IOCC): Regression analysis of equilibrium data with several isotherm models and their optimization, Chem. Eng. J. 122 (2006) 93–106. https://doi.org/10.1016/j.cej.2006.06.002.

[59] S. Arpadjan, L. Vuchkova, E. Kostadinova, Sorption of arsenic, bismuth, mercury, antimony, selenium and tin on dithiocarbamate loaded polyurethane foam as a preconcentration method for their determination in water samples by simultaneous inductively coupled plasma atomic emission spectrometry and, Analyst. 122 (1997) 243–246. https://doi.org/10.1039/a606917g.

[60] A.K. Mishra, S. Ramaprabhu, Functionalized graphene sheets for arsenic removal and desalination of sea water, Desalination. 282 (2011) 39–45. https://doi.org/10.1016/j.desal.2011.01.038.

[61] K. Zhang, V. Dwivedi, C. Chi, J. Wu, Graphene oxide/ferric hydroxide composites for efficient arsenate removal from drinking water, J. Hazard. Mater. 182 (2010) 162–168. https://doi.org/10.1016/j.jhazmat.2010.06.010.

[62] B. Liu, J. Liu, DNA adsorption by magnetic iron oxide nanoparticles and its application for arsenate detection, Chem. Commun. 50 (2014) 8568–8570. https://doi.org/10.1039/c4cc03264k.

[63] C. Song, W. Sun, Y. Xiao, X. Shi, Ultrasmall iron oxide nanoparticles: synthesis, surface modification, assembly, and biomedical applications, Drug Discov. Today. 24 (2019) 835–844. https://doi.org/10.1016/j.drudis.2019.01.001.

[64] J.T. Mayo, C. Yavuz, S. Yean, L. Cong, H. Shipley, W. Yu, J. Falkner, A. Kan, M. Tomson, V.L. Colvin, The effect of nanocrystalline magnetite size on arsenic removal, Sci. Technol. Adv. Mater. 8 (2007) 71–75. https://doi.org/10.1016/j.stam.2006.10.005.

[65] A. Ali, H. Zafar, M. Zia, I. ul Haq, A.R. Phull, J.S. Ali, A. Hussain, Synthesis, characterization, applications, and challenges of iron oxide nanoparticles, Nanotechnol. Sci. Appl. 9 (2016) 49–67. https://doi.org/10.2147/NSA.S99986.

[66] H. Su, Z. Ye, N. Hmidi, High-performance iron oxide–graphene oxide nanocomposite adsorbents for arsenic removal, Colloids Surfaces A Physicochem. Eng. Asp. 522 (2017) 161–172. https://doi.org/10.1016/j.colsurfa.2017.02.065.

[67] Y. Yu, L. Yu, K. Shih, J.P. Chen, Yttrium-doped iron oxide magnetic adsorbent for enhancement in arsenic removal and ease in separation after applications, J. Colloid Interface Sci. 521 (2018) 252–260. https://doi.org/10.1016/j.jcis.2018.02.046.

[68] M. Usman, A.I. Belkasmi, I.A. Kastoyiannis, M. Ernst, Pre-deposited dynamic membrane adsorber formed of microscale conventional iron oxide-based adsorbents to remove arsenic from water: application study and mathematical modeling, J. Chem. Technol. Biotechnol. 96 (2021) 1504–1514. https://doi.org/10.1002/jctb.6728.

[69] S.I. Siddiqui, S.A. Chaudhry, Iron oxide and its modified forms as an adsorbent for arsenic removal: A comprehensive recent advancement, Process Saf. Environ. Prot. 111 (2017) 592–626. https://doi.org/10.1016/j.psep.2017.08.009.

[70] H. Wang, X. Zhao, X. Han, Z. Tang, S. Liu, W. Guo, C. Deng, Q. Guo, H. Wang, F. Wu, X. Meng, J.P. Giesy, Effects of monovalent and divalent metal cations on the aggregation and suspension of Fe3O4 magnetic nanoparticles in aqueous solution, Sci. Total Environ. 586 (2017) 817–826. https://doi.org/10.1016/j.scitotenv.2017.02.060.

[71] J. Liu, C. Dai, Y. Hu, Aqueous aggregation behavior of citric acid coated magnetite nanoparticles: Effects of pH, cations, anions, and humic acid, Environ. Res. 161 (2018) 49–60. https://doi.org/10.1016/j.envres.2017.10.045.

[72] P. Suresh Kumar, T. Prot, L. Korving, K.J. Keesman, I. Dugulan, M.C.M. van Loosdrecht, G.J. Witkamp, Effect of pore size distribution on iron oxide coated granular activated carbons for phosphate adsorption – Importance of mesopores, Chem. Eng. J. 326 (2017) 231–239. https://doi.org/10.1016/j.cej.2017.05.147.

[73] S. You, S.W. Ho, T. Li, T. Maneerung, C.H. Wang, Techno-economic analysis of geopolymer production from the coal fly ash with high iron oxide and calcium oxide contents, J. Hazard. Mater. 361 (2019) 237–244. https://doi.org/10.1016/j.jhazmat.2018.08.089.

[74] V.K. Gupta, V.K. Saini, N. Jain, Adsorption of As(III) from aqueous solutions by iron oxide-coated sand, J. Colloid Interface Sci. 288 (2005) 55–60. https://doi.org/10.1016/j.jcis.2005.02.054.

[75] Y.C. Park, J. Paulsen, R.J. Nap, R.D. Whitaker, V. Mathiyazhagan, Y.Q. Song, M. Hürlimann, I. Szleifer, J.Y. Wong, Adsorption of superparamagnetic iron oxide nanoparticles on silica and calcium carbonate sand, Langmuir. 30 (2014) 784–792.

https://doi.org/10.1021/la404387t.

[76] S. Sharma, A. Hasan, N. Kumar, L.M. Pandey, Removal of methylene blue dye from aqueous solution using immobilized Agrobacterium fabrum biomass along with iron oxide nanoparticles as bioadsorbent, Environ. Sci. Pollut. Res. 25 (2018) 21605–21615. https://doi.org/10.1007/s11356-018-2280-z.

[77] X. Zhang, X. Fang, J. Li, S. Pan, X. Sun, J. Shen, W. Han, L. Wang, S. Zhao, Developing new adsorptive membrane by modification of support layer with iron oxide microspheres for arsenic removal, J. Colloid Interface Sci. 514 (2018) 760–768. https://doi.org/10.1016/j.jcis.2018.01.002.

[78] M.H. Zeeshan, R.U. Khan, M. Shafiq, A. Sabir, Polyamide intercalated nanofiltration membrane modified with biofunctionalized core shell composite for efficient removal of Arsenic and Selenium from wastewater, J. Water Process Eng. 34 (2020) 101175. https://doi.org/10.1016/j.jwpe.2020.101175.

[79] S.M. Hosseini Asl, M. Masomi, M. Hosseini, H. Javadian, M. Ruiz, A.M. Sastre, Synthesis of hydrous iron oxide/aluminum hydroxide composite loaded on coal fly ash as an effective mesoporous and low-cost adsorbent for Cr(VI) sorption: Fuzzy logic modeling, Process Saf. Environ. Prot. 107 (2017) 153–167. https://doi.org/10.1016/j.psep.2017.02.012.

[80] S. Kirti, V.M. Bhandari, J. Jena, A.S. Bhattacharyya, Elucidating efficacy of biomass derived nanocomposites in water and wastewater treatment, J. Environ. Manage. 226 (2018) 95–105. https://doi.org/10.1016/j.jenvman.2018.08.028.

[81] S. Kirti, V.M. Bhandari, J. Jena, L.G. Sorokhaibam, A.S. Bhattacharyya, Exploiting functionalities of biomass in nanocomposite development: application in dye removal and disinfection along with process intensification, Clean Technol. Environ. Policy. 20 (2018) 981–994. https://doi.org/10.1007/s10098-018-1519-1.

[82] D. Morillo, G. Pérez, M. Valiente, Efficient arsenic(V) and arsenic(III) removal from acidic solutions with Novel Forager Sponge-loaded superparamagnetic iron oxide nanoparticles, J. Colloid Interface Sci. 453 (2015) 132–141. https://doi.org/10.1016/j.jcis.2015.04.048.

[83] D. Morillo, A. Uheida, G. Pérez, M. Muhammed, M. Valiente, Arsenate removal with 3-mercaptopropanoic acid-coated superparamagnetic iron oxide nanoparticles, J. Colloid

Interface Sci. 438 (2015) 227–234. https://doi.org/10.1016/j.jcis.2014.10.005.

[84] D. Morillo Martín, Superparamagnetic iron oxide nanoparticles as arsenic adsorbent development of nanofiber SPION supports and arsenic speciation using synchrotron and hyphenated techniques, Universitat Autònoma de Barcelona, 2014. https://hdl.handle.net/10803/129335.

[85] L. He, Development of Reagent-less Processes for Water Decontamination. Tuning of Temperature and Redox Parameters to Remove Toxic Oxyanions., Universitat Autònoma de Barcelona, 2015. https://hdl.handle.net/10803/326753.

[86] V. Verdugo Andrés, Studies on As and Sb oxoanions adsorption: use of mass spectroscopy and synchrotron techniques on process characterisation, 2019. https://hdl.handle.net/10803/667798.

[87] M. Kaljurand, M. Koel, Recent advancements on greening analytical separation, Crit. Rev. Anal. Chem. 41 (2011) 2–20. https://doi.org/10.1080/10408347.2011.539420.

[88] Y. Wu, R.K. Kukkadapu, K.J.T. Livi, W. Xu, W. Li, D.L. Sparks, Iron and Arsenic Speciation during As(III) Oxidation by Manganese Oxides in the Presence of Fe(II): Molecular-Level Characterization Using XAFS, Mössbauer, and TEM Analysis, ACS Earth Sp. Chem. 2 (2018) 256–268. https://doi.org/10.1021/acsearthspacechem.7b00119.

[89] R. Amen, H. Bashir, I. Bibi, S.M. Shaheen, N.K. Niazi, M. Shahid, M.M. Hussain, V. Antoniadis, M.B. Shakoor, S.G. Al-Solaimani, H. Wang, J. Bundschuh, J. Rinklebe, A critical review on arsenic removal from water using biochar-based adsorbents: The significance of modification and redox reactions, Chem. Eng. J. 396 (2020) 125195. https://doi.org/10.1016/j.cej.2020.125195.

[90] X. Hu, Z. Ding, A.R. Zimmerman, S. Wang, B. Gao, Batch and column sorption of arsenic onto iron-impregnated biochar synthesized through hydrolysis, Water Res. 68 (2015) 206–216. https://doi.org/10.1016/j.watres.2014.10.009.

[91] N.K. Niazi, I. Bibi, M. Shahid, Y.S. Ok, S.M. Shaheen, J. Rinklebe, H. Wang, B. Murtaza, E. Islam, M. Farrakh Nawaz, A. Lüttge, Arsenic removal by Japanese oak wood biochar in aqueous solutions and well water: Investigating arsenic fate using integrated spectroscopic and microscopic techniques, Sci. Total Environ. 621 (2018) 1642–1651. https://doi.org/10.1016/j.scitotenv.2017.10.063.

Chapter 3: Adsorbents: synthesis and characterizations

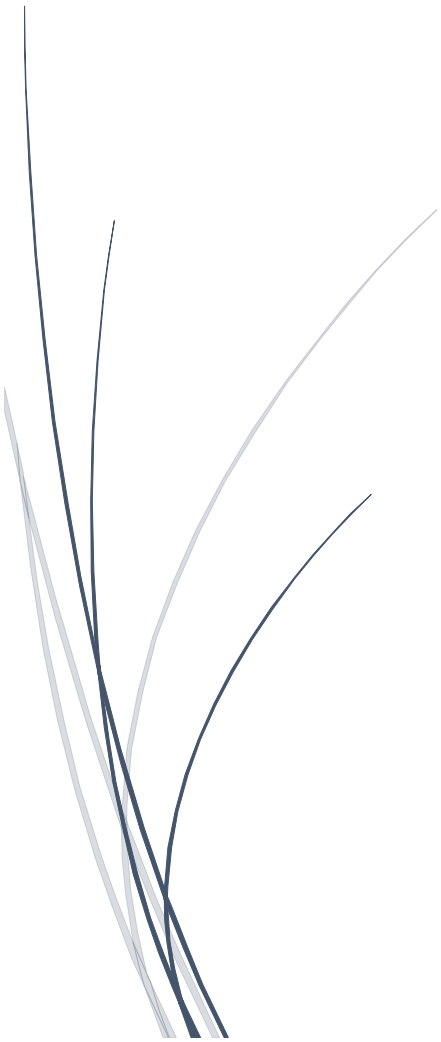

3.1. Materials and chemical reagents

Commercial cube-shaped MetalZorb® adsorbent was kindly supplied by CleanWay Environmental Partners, Inc. (Portland, USA). This material is an open-celled cellulose sponge (hereafter referred simply as "sponge") which incorporates a water-insoluble polyamide chelating polymer. The sponge contains free available ethyleneamine and iminodiacetate groups that interact with heavy metals ions by ion exchange mechanism and chelation, respectively [1]. The sponge has a low impedance of diffusion and it is light in weight. When used in a column, flow rates of three bed volumes per minute can be obtained at hydrostatic pressures only ~60 cm above the bed and without any additional pressurization. These properties make this porous material a good candidate for supporting nanoparticles in industrial water remediation applications. The averaged dimensions of the cube are (length x width x height): 12.8 ± 1.8 x 10.1 ± 1.1 x 7.3 ± 1.3 mm. Each cube has an average weight of 0.20 ± 0.02 g.

All reagents used were of analytical grade. Iron chloride hexahydrate ($FeCl_3 \cdot 6H_2O$) and ferrous chloride tetrahydrate ($FeCl_2 \cdot 4H_2O$) were used in the synthesis of SPION and sponge-loaded SPION.

3.2 Pre-treatment of sponge

Following the manufacturer's advice, the sponge was pretreated with dilute HCl to remove all possible pre-absorbed cations. This protonates the amino functional groups, which improves the adsorption capacity of the adsorbent. In addition, this activation step facilitates the immobilization of the nanoparticles on the sponge surface. The activation of the as-received sponge was performed in batches of 6 cubes in a 50 ml tube as follow: immersion of the cubes in Milli-Q water for 24 h, immersion in 1.0 $mol \cdot L^{-1}$ HCl solution for 4 h to fully protonate the iminodiacetate group, rinsing with Milli-Q water until the pH value was

4.0, immersion in HCl solution at pH 2.5 for 2 h to equilibrate the pH value, and washing 5 times with Milli-Q water to remove the excess of acid solution. Afterwards, the water was decanted and the cubes were dried in an oven at 50°C for 24 h.

3.3. Synthesis of SPION and cube-loaded SPION

SPION was synthesized by co-precipitation using an alkaline mixture of iron chloride hexahydrate ($FeCl_3 \cdot 6H_2O$) and ferrous chloride tetrahydrate ($FeCl_2 \cdot 4H_2O$) solution as has been described previously [2,3]. The synthesis was carried out while bubbling nitrogen gas to avoid SPION oxidization and while stirring at 300 rpm to ensure proper mixing of all the reagents during the synthesis. The loading of SPION on the cube sponge was carried out in-situ as follows: first, 100 ml Milli-Q water was added to 500 ml Erlenmeyer flask, deoxygenated for 30 mins and heated at 40°C. Then, the Fe(II) and Fe(III) precursors (0.02 and 0.04 M, respectively), and six sponge cubes were added to the solution and leave it stirring for 30 min. Afterward, 120 ml of 0.5 $mol \cdot L^{-1}$ NaOH was added to the solution drop by drop and the mixture was stirred for an hour to leave enough time for completing the reaction. The resulting composite material was separated by decanting, washed three times with 50 ml deoxygenated Milli-Q water and dried in an oven at 50°C for 24 h.

3.4. Characterizations of the adsorbents

Scanning electron microscope (SEM, Merlin, Carl Zeiss AG, Oberkochen, Germany) images were collected to get information about the morphology of the materials. The morphology and size of the SPION were characterized by Transmission Electron Microscope (TEM, JEM-1400, JEOL, Tokyo, Japan). Fourier transform infrared spectroscopy (FT-IR, Tensor 27, Bruker, Massachusetts, USA) measurements were performed to identify the functional

groups of SPION, sponge, and sponge-loaded SPION. X-ray powder diffraction (XRD, X-Pert, Philips, Amsterdam, Netherlands) was carried out to identify the iron oxide phase and crystallinity of the nanoparticles. X-ray absorption spectroscopy (XAS) measurements at the Fe K-edge were performed in transmission mode at room temperature to study the iron oxide phase in SPION and sponge-loaded SPION (Si(111) double crystal monochromator, BL22 CLÆSS beamline of ALBA CELLS synchrotron) [4].

Cube samples were cut and divided into three parts: surface (1.5 mm from the surface), quarter (1.5-3.0 mm from the surface) and center (remaining part of the cube), as shown in Figure 3.1. These parts account for ~68%, ~28% and ~4% of the cube volume, respectively.

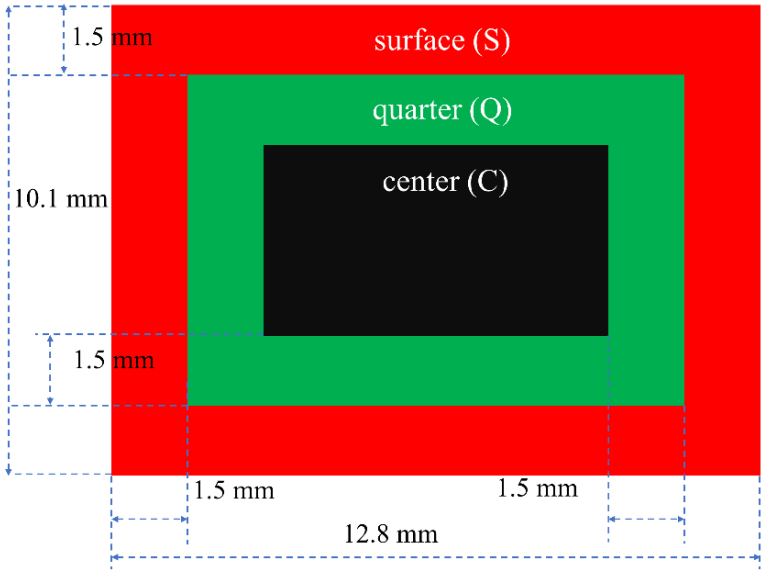

Figure 3.1. Spilt method of cube adsorbents to investigate different depth parts (cross-sectional section).

3.4.1 SEM and TEM

The SEM images (top panels in Figure 3.2) revealed the microstructure and morphology of the adsorbent materials. A severe aggregation of the nanoparticles was found for SPION sample when synthesized without support,

see Figure 3.2a. The open-celled structure of sponge composed by connected pores can be seen in Figure 3.2b. The loading of SPION into sponge is clearly indicated by the darkening of the final material with respect to the original sponge (see Figure 3.3). After loading the nanoparticles, the surface of sponge becomes more heterogeneous, see Figure 3.3c. It is clear that having the sponge as support helps in reducing the nanoparticle aggregation to a large extent. SEM images of sponge and sponge-loaded SPION with smaller magnification are also shown in Figure 3.4.

The TEM images of sponge-loaded SPION and the corresponding particle size distribution histograms calculated using Image-Pro Plus software (Media Cybernetics, Silver Spring, USA) are shown in Figure 3.2 (middle and bottom panels). The nanoparticles are coating the surface of the sponge and they are not blocking the pores, which preserves the advantageous diffusion properties of the original sponge material. The nanoparticles are mostly spherical, and the mean nanoparticle size found for the surface and the center parts of the cube sponge-loaded SPION were 12.7 and 13.8 nm, respectively. The histogram shows that the particle size dispersion, considering a normal distribution, has similar width for both, surface and center parts of the cube, see Figure 3.2f and 3.2g. However, almost a bimodal distribution is found at the surface part which highlights the important contribution of the smaller particles. Indeed, a detailed analysis of the particle size data revealed that, in average, due to the smaller particle size, the surface/volume ratio is 10% larger at the surface part.

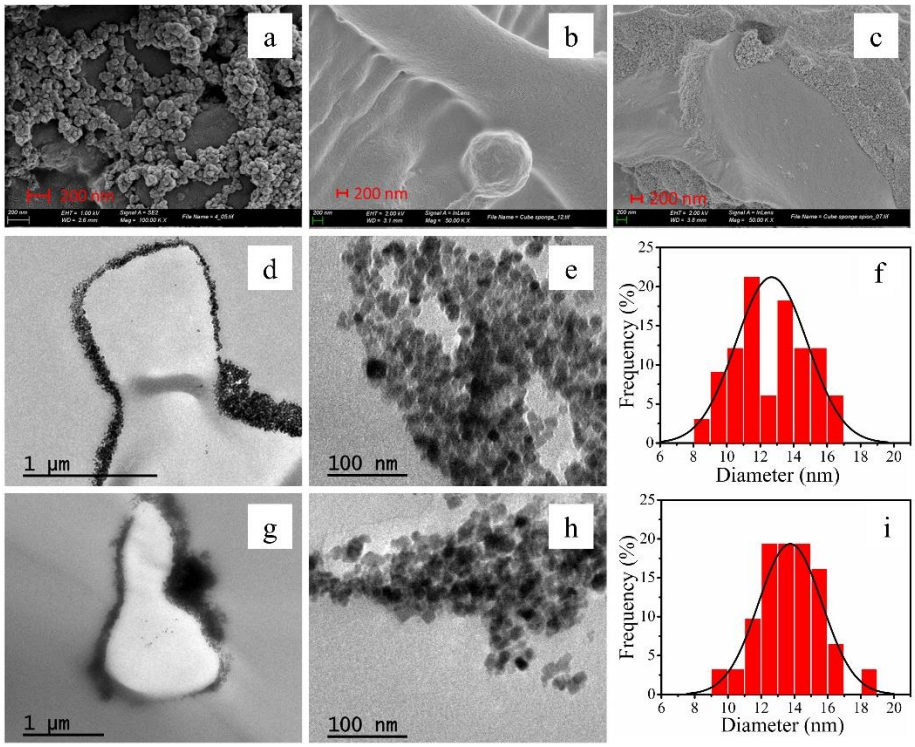

Figure 3.2. SEM images for SPION (a), sponge (b) and sponge-loaded SPION (c). TEM images and particle size histogram for surface (d, e, f) and center parts of sponge-loaded SPION (g, h, i).

Figure 3.3. Pictures of SPION (a), sponge (b) and sponge-loaded SPION (c).

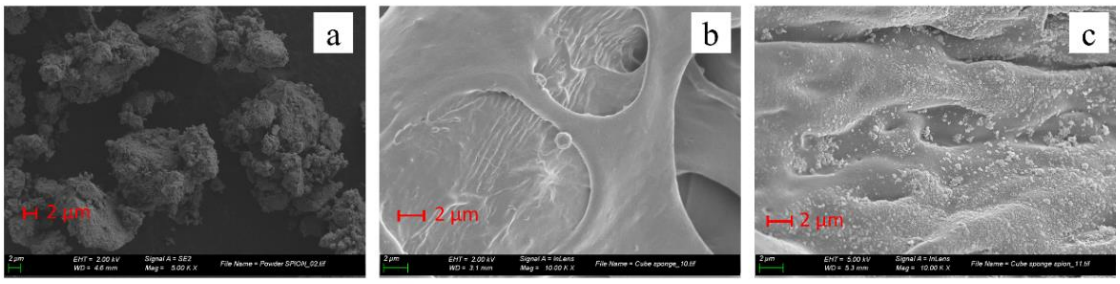

Figure 3.4. SEM images of SPION(a), sponge (b) and sponge-loaded SPION (c).

3.4.2 FT-IR

FT-IR analysis was performed to identify the functional groups present on the adsorbent materials. The spectra comparison is shown in Figure 3.5. The spectra have been shifted vertically for shake of comparison. For the unloaded sponge, the peak centers appeared at 3332, 2879, 1637, 1358, and 1018 cm^{-1} which could be -NH_2/-OH, -CH_2, -C=O/-OH, C=C, and -C=O/-C-O-C stretching vibrations, respectively. These results are consistent with the sponge containing free available ethyleneamine (-NH_2-CH_2-CH_2-) and iminodiacetate (–(C=O)-NH-(C=O)-) groups as claimed by the supplier. The spectrum of SPION shows a very intense band at 560 cm^{-1} which is characteristic of the Fe-O bond [5]. As for sponge-loaded SPION, the Fe-O band is much less intense than the one of SPION sample due to the low loading amount (~ 2.6 wt.%) of nanoparticles in the composite material.

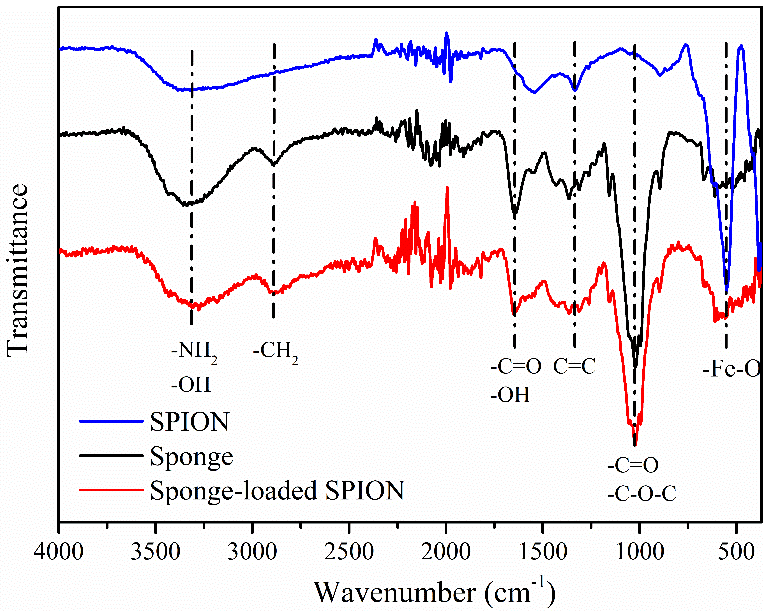

Figure 3.5. FT-IR spectrum of SPION, sponge, and sponge-loaded SPION.

3.4.3 XRD

X-ray diffraction (XRD) measurements were performed on SPION and cube sponge-loaded SPION to identify the iron oxide phase. Figure 3.6 shows the comparison of the experimental diffraction patterns with the simulated ones for Fe_2O_3 (American Mineralogist Crystal Structure Database, code: 0007898) [5] and Fe_3O_4 (American Mineralogist Crystal Structure Database, code: 0002400) [6].

The diffraction pattern of both samples displayed the characteristic reflections of the spinel structure; however, it was not possible to determine the iron phase since the diffraction patterns of maghemite, γ-Fe_2O_3, and magnetite, Fe_3O_4, were very similar and the widths of the diffraction peaks yield by the nanoparticles were quite wide.

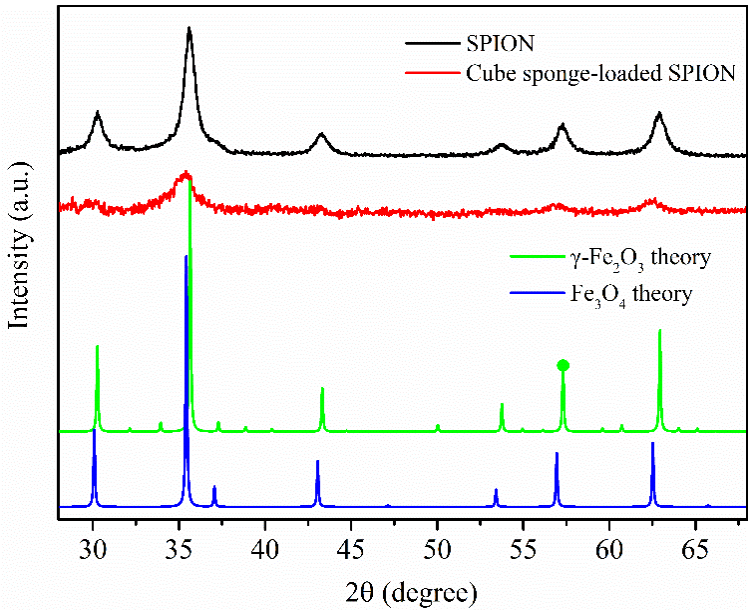

Figure 3.6. XRD spectra of SPION, cube sponge-loaded SPION, theory γ-Fe_2O_3 and theory Fe_3O_4.

3.4.4 Fe K-edge XANES measurements

In order to further identify the iron oxide phase, XAS analysis at the Fe K-edge was performed. Figure 3.7 shows the comparison of the X-ray absorption near edge structure (XANES) region of the Fe K-edge XAS spectra collected on SPION, sponge-loaded SPION (surface) and the reference bulk iron oxide materials, maghemite (Fe_3O_4) and maghemite (γ-Fe_2O_3). Magnetite and maghemite references show a clearly different XANES spectra. The position of the absorption rising edge, which is highly influenced by the oxidation state of the Fe ions, appears at higher energy for maghemite which contains only Fe(III) ions. Indeed, magnetite can be considered as a Fe(II)-deficient magnetite. In addition, the energy shift of the edge is also influenced by the Fe–O bond length (the shorter the interatomic distance, the higher the edge energy) and this can account for bond length expansion in non-stochiometric iron oxide nanoparticles due to the reduced coordination [7].

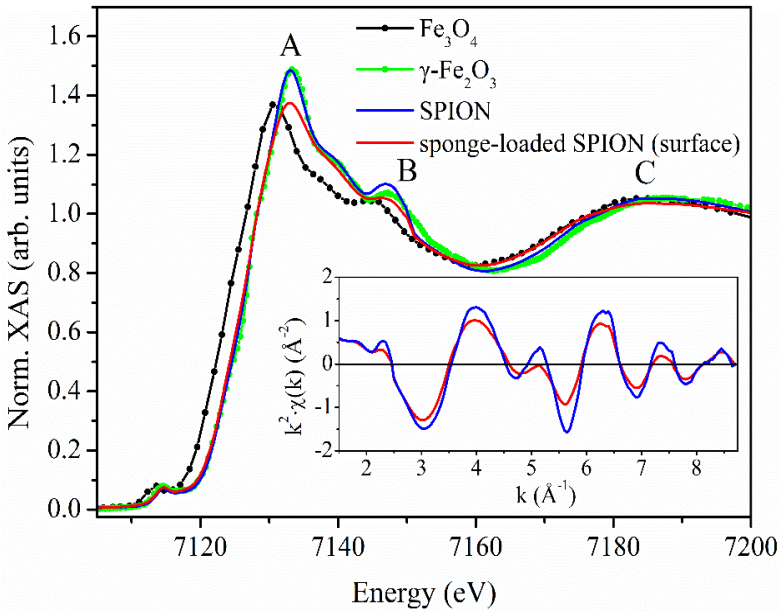

Figure 3.7. Fe K-edge XAS spectra of SPION, sponge-loaded SPION (surface) and the two iron oxide reference materials (Fe_3O_4, γ-Fe_2O_3). Inset includes the extracted EXAFS signal.

In our case, the XANES spectrum of SPION is almost identical to the maghemite reference reflecting the bulk character of the nanoparticle aggregates. On the other side, the spectrum of the SPION nanoparticles loaded in the sponge is slightly different from the one of the SPION sample. It also resembles the spectral profile of the maghemite reference, but the spectral features A, B and C are smeared out respect to SPION.

In a similar fashion, we found that, when comparing the extracted extended X-ray absorption fine structure (EXAFS) signal for both samples (see inset in Figure 3.7), the amplitude of the oscillation is smaller for sponge-loaded SPION. This is related with the decrease of the coordination number of Fe atoms close to the surface of the iron oxide nanoparticles and the increase of disorder respect to the bulk structure. These observations point out that the main iron phase of the nanoparticles in the sponge-loaded SPION is maghemite, i.e. the Fe oxidation state is dominated by Fe(III). This is beneficial in terms of the adsorption capacity maghemite provides a higher adsorption capacity and a more stable Fe-As complex after As(V) adsorption than magnetite [8]. Regarding the different parts of the cube, no significant change in the chemical state of the iron oxide was found at different parts of the cube as shown in Figure 3.8. A rough estimation of the atomic Fe concentration obtained from the absorption jump of the XAS spectrum revealed that there is an average of ~15% less Fe in the surface part than in the center part. This observation agrees with the results regarding the particle size distribution and the surface/volume ratio estimation along the cube depth and supports the idea that smaller particles are loaded at the surface part.

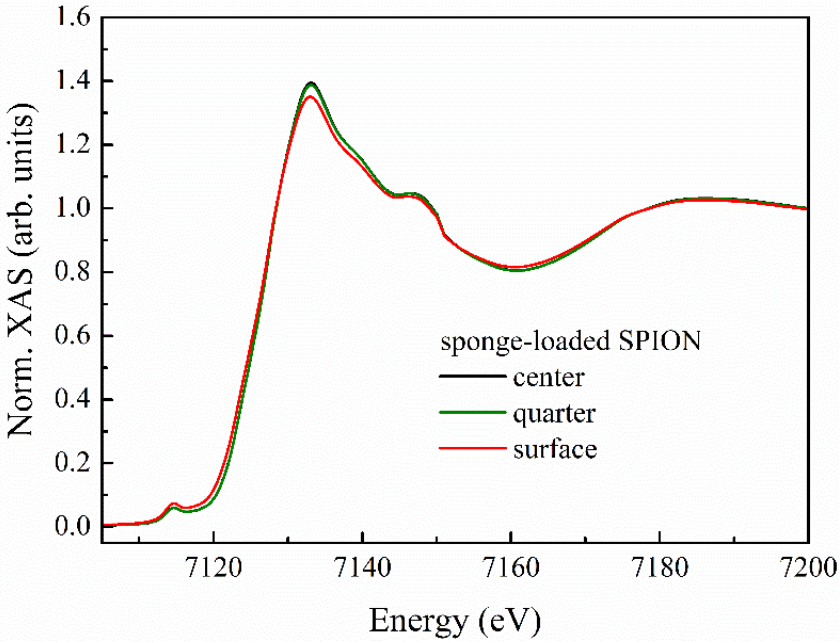

Figure 3.8. Fe K-edge XAS spectra of the different sponge-loaded SPION parts.

3.5. Conclusions

1) In this study, the composite material cube-shaped open-celled cellulose sponge-loaded SPION was successfully synthesized by the in-situ co-precipitation method.

2) TEM images analysis showed that the mean nanoparticle size found for the surface and the center parts of the cube sponge-loaded SPION were 12.7 and 13.8 nm, respectively.

3) XAS of Fe K-edge analysis pointed out that the main iron phase of the nanoparticles is maghemite.

3.6. Reference

[1] J.A. Muñoz, A. Gonzalo, M. Valiente, Arsenic adsorption by Fe(III)-loaded open-celled cellulose sponge. Thermodynamic and selectivity aspects, Environ. Sci. Technol. 36 (2002) 3405–3411. https://doi.org/10.1021/es020017c.

[2] A. Uheida, G. Salazar-Alvarez, E. Björkman, Z. Yu, M. Muhammed, Fe3O4 and γ-Fe2O3 nanoparticles for the adsorption of Co2+ from aqueous solution, J. Colloid Interface Sci. 298 (2006) 501–507. https://doi.org/10.1016/j.jcis.2005.12.057.

[3] D. Morillo, A. Uheida, G. Pérez, M. Muhammed, M. Valiente, Arsenate removal with 3-mercaptopropanoic acid-coated superparamagnetic iron oxide nanoparticles, J. Colloid Interface Sci. 438 (2015) 227–234. https://doi.org/10.1016/j.jcis.2014.10.005.

[4] L. Simonelli, C. Marini, W. Olszewski, M. Ávila Pérez, N. Ramanan, G. Guilera, V. Cuartero, K. Klementiev, CLÆSS: The hard X-ray absorption beamline of the ALBA CELLS synchrotron, Cogent Phys. 3 (2016) 1231987. https://doi.org/10.1080/23311940.2016.1231987.

[5] V. Barrón, J. Torrent, E. De Grave, Hydromaghemite, an intermediate in the hydrothermal transformation of 2-line ferrihydrite into hematite, Am. Mineral. 88 (2003) 1679–1688. https://doi.org/10.2138/am-2003-11-1207.

[6] C. Haavik, S. Stølen, H. Fjellvåg, M. Hanfland, D. Häusermann, Equation of state of magnetite and its high-pressure modification: Thermodynamics of the Fe-O system at high pressure, Am. Mineral. 85 (2000) 514–523. https://doi.org/10.2138/am-2000-0413.

[7] C. Piquer, M.A. Laguna-Marco, A.G. Roca, R. Boada, C. Guglieri, J. Chaboy, Fe K-edge X-ray absorption spectroscopy study of nanosized nominal magnetite, J. Phys. Chem. C. 118 (2014) 1332–1346. https://doi.org/10.1021/jp4104992.

[8] M.E. Mejia-Santillan, N. Pariona, J. Bravo-C., M. Herrera-Trejo, F. Montejo-Alvaro, A. Zarate, D.L. Perry, A.I. Mtz-Enriquez, Physical and arsenic adsorption properties of maghemite and magnetite sub-microparticles, J. Magn. Magn. Mater. 451 (2018) 594–601. https://doi.org/10.1016/j.jmmm.2017.11.111.

Chapter 4: As(V) adsorption behavior and mechanism studies by cube sponge-loaded SPION

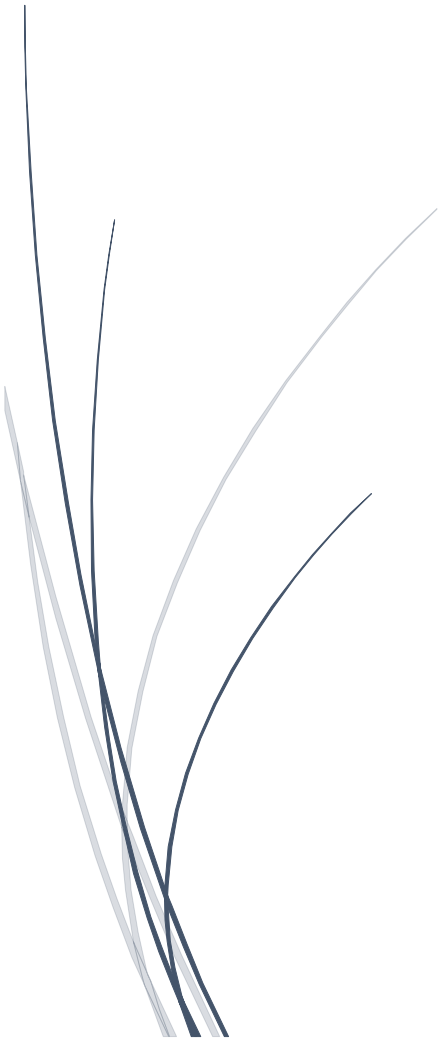

4.1. Materials and methodology

4.1.1 Chemical reagent

All reagents used were of analytical grade and purchased from Sigma-Aldrich (Missouri, USA), Panreac (Barcelona, Spain), Scharlab (Barcelona, Spain) or Honeywell, (Charlotte, USA).

The stock aqueous solution of 1000 mg·L^{-1} As(V) was prepared from sodium arsenate dibasic heptahydrate ($Na_2HAsO_4 \cdot H_2O$). The pH was adjusted to 3.6 prior to the adsorption experiments by adding the appropriate amount of hydrogen chloride (HCl) or sodium hydroxide (NaOH) in order to optimize the adsorption in accordance with previous works [1,2].

Ammonium molybdate, $(NH_4)_6Mo_7O_{24} \cdot 4H_2O$]; antimony potassium tartrate $C_8H_4K_2O_{12}Sb_2 \cdot 1/2H_2O$; sulfuric acid, H_2SO_4; and ascorbic acid, $C_6H_8O_6$; were used as color reagents for the detection of As(V) by molybdenum blue method as described elsewhere [3,4].

4.1.2 Adsorption experiments

The experiments were performed in 50 ml plastic tubes containing 25 ml As(V) solution and one cube of the adsorbent material (sponge or sponge-loaded SPION, 0.20 g). The tubes were agitated mechanically at 300 rpm and at 293, 318 or 343 K by using a shaker inside a temperature-controlled incubator. The solutions were separated from the adsorbents by filtration and As(V) concentration in the solution was determined by UV-visible spectrometric technique based on the molybdenum blue method (See section 4.1.4). The adsorption capacity at the equilibrium was calculated using the following equation:

$$q_e = (C_o - C_e)\frac{V}{m} \quad (4.1)$$

where q_e ($mg \cdot g^{-1}$) is the adsorption capacity, V (L) is the volume of the arsenic solution, m (g) is the weight of the adsorbent, C_o and C_e ($mg \cdot L^{-1}$) are initial and equilibrium concentrations of As(V) solution, respectively.

4.1.3 Adsorption-desorption cycle experiments

For regenerating the adsorbent material after adsorption, the cubes of sponge-loaded SPION were separated by filtration, washed three times with Milli-Q water, and immersed in 25 ml 0.5 M NaOH solution to desorb the arsenic. After shaking at 300 rpm for 60 min, the adsorbent was separated by filtration and rinsed with 25 ml Milli-Q water. Finally, cube sponge-loaded SPION was dried at 50℃ for 24 h before carrying out the next adsorption run. This adsorption/desorption cycle was repeated five times to determine the regeneration capacity of the composite adsorbent material.

4.1.4 Determination of As(V) concentration by UV-Visible

As(V) concentration in the solution was determined by UV-visible spectrometric technique based on the molybdenum blue method. The detection range was 0.5-4 $mg \cdot L^{-1}$. The detailed steps are as follows:

1) Color solution A preparation: 6.9 g Ammonium Molybdate [$(NH_4)_6Mo_7O_{24} \cdot 4H_2O$] was dissolved in 50 ml Milli-Q water; 0.175 g Antimony Potassium Tartrate was dissolved ($C_8H_4K_2O_{12}Sb_2 \cdot 1/2H_2O$) in 50 ml Milli-Q water; 150 ml 17.74 $mol \cdot L^{-1}$ Sulfuric Acid (H_2SO_4) was prepared; Three solutions above were mixed together to get the color solution A.
2) Color solution B preparation: 5.0 g Ascorbic acid ($C_6H_8O_6$) was diluted to 50 ml Milli-Q water to get color solution B.
3) Prepare a series of arsenic standard solutions (0, 0.5, 1.0, 2.0, 3.0, 4 $mg \cdot L^{-1}$) with Milli-Q water. Pipet 8.8 ml of each standard solution into a 10 ml test tube. Then add 0.8 ml color solution A and 0.4 ml color solution B.

4) Dilute the sample concentration in the range of 0.5-4 mg·L^{-1}. Then pipet 8.8 ml of each diluted solution into a 10 ml test tube. Then add 0.8 ml color solution A and 0.4 ml color solution B.
5) After at least 60 minutes of color development, absorbance was detected at 855 nm, using the blank as the reference.

4.1.5 As K-edge XAS measurements

XAS measurements at the As K-edge were performed to study the chemical state and coordination environment of the adsorbed arsenic after exposing the adsorbents to an initial concentration of 200 mg·L^{-1} As(V). In order to get information at different depths of both materials, cube sponge and sponge-loaded SPION, the cubes were split into three regions as mentioned before: surface, quarter and center.

The XAS experiment was carried out at BL22 CLÆSS beamline of ALBA CELLS synchrotron using a Si(311) double crystal monochromator [5]. Measurements of As-sponge, As-sponge-loaded SPION adsorbents and As reference samples were performed in transmission mode using ionization chambers. All the samples were milled and pressed into pellets without using any binder. A multi-element silicon drift detector with Xspress3 electronics was used for collecting the spectra in fluorescence mode of As-SPION sample. To reduce the self-absorption effects, As-SPION was homogeneously mixed with cellulose using a 1:10 ratio. Special care was taken when setting up the fluorescence mode to minimize the dead-time effect. The measurements were carried out at liquid nitrogen temperature to minimize any radiation damage. XAS data analysis was performed according to standard procedures using ATHENA and ARTEMIS software of the Demeter package [6].

4.1.6 As K-edge XAS analysis

XAS data analysis was performed by using Athena and Artemis programs included in the Demeter software package (version 0.9.26) [6]. In the EXAFS linear combination fitting (LCF) the fitting range in k-space was set to 2.75~15.0 $Å^{-1}$. The spectra of sponge-loaded SPION (S) were fitted by using sponge (S) and SPION as references.

Fourier transformation of the EXAFS signal was performed to generate the radial distribution function (k-range, 2.75 ~ 13.0 $Å^{-1}$). Theoretical As-O, As–Fe and As-O-O scattering paths were calculated from the structural model of scorodite [7]. The spectra of SPION were fitted including the second shell (R-range 1-3.5 Å), while only the first shell was fitted for sponge and sponge-loaded SPION samples (R-range 1-1.9 Å. In the shell-by-shell fitting, the coordination number (CN) of As-O was fixed to 4 because of the tetrahedron structure and CN of As-Fe was fixed to 2 assuming a binuclear corner-sharing, ^2C, configuration. For the multiple scattering (MS) path (As-O-O), the CN was fixed to 12 according to the structure of AsO_4 tetrahedron. In a regular tetrahedron, the distance between vertices is related to the distance from the center to a vertex by a geometrical factor. Therefore, the distance of MS path was constrained geometrically to be 1.82 times of the single scattering As-O path ($R_{As\text{-}O\text{-}O} = 1.82*R_{As\text{-}O}$). The addition of this MS path improved the goodness-of-fit parameter, but did not affect the fit parameters obtained for the As–Fe second shell [8].

4.2. Adsorption behaviors

To assess the As(V) adsorption performance of cube sponge and cube sponge-loaded SPION, batch adsorption experiments with different initial concentrations, different contact times and different temperatures were performed.

As can be seen in Figure 4.1a, the adsorption capacity of sponge and sponge-loaded SPION increase when increasing the As(V) initial concentration. Both adsorbents show better adsorption at 293 K than at 343 K, while sponge-loaded SPION has a higher adsorption capacity than sponge alone. These adsorption experiments did not reach saturation within the concentration range studied. However, the maximum initial concentration used in this study is 800 mg·L^{-1}, which is much higher than the concentration found in polluted groundwater [9].

Adsorption results with different contact times, Figure 4.1b, revealed that there is a transient initial stage in which the adsorption capacity sharply increases. This can be attributed to a large number of adsorption sites initially available on the surface of the adsorbent. The adsorption capacity becomes almost constant after ~60 min. When comparing different adsorbents, sponge-loaded SPION showed a higher equilibrium adsorption capacity and a slightly faster adsorption process.

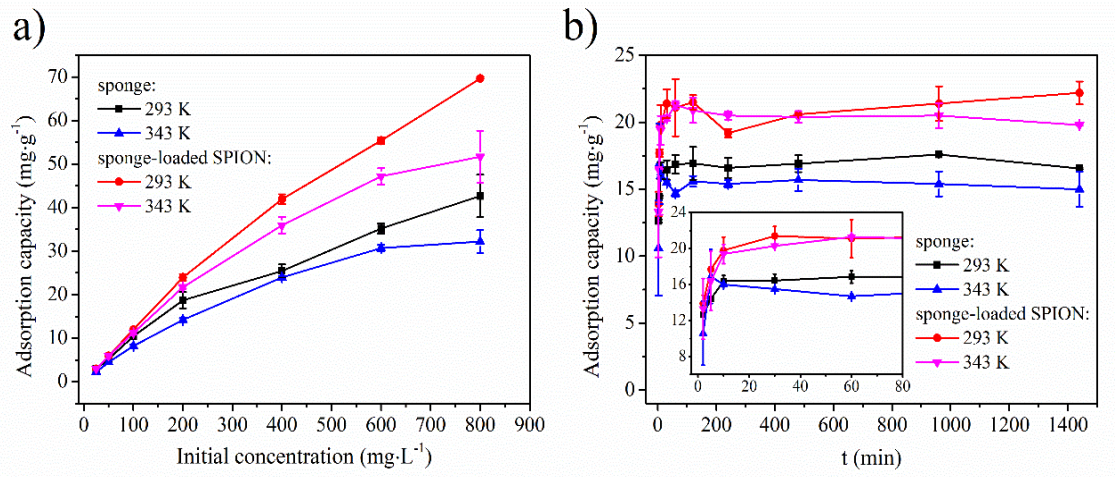

Figure 4.1. As(V) adsorption capacity using cube sponge and sponge-loaded SPION: initial concentration (a); contact time (b).

Our results show that the adsorption capacity of the sponge increases notably after loading SPION. Considering an initial concentration of 200 mg·L^{-1} and at

293 K, the adsorption capacity increases from 18.7 to 24.0 $mg \cdot g^{-1}$ after loading SPION. This means that the adsorption capacity of sponge increases 28.3% after loading only 2.6 wt.% mass fraction of SPION (63.2% at 800 $mg \cdot L^{-1}$ initial concentration). This adsorption capacity is considerably higher than the ones reported for other iron-based composite materials, see Table 4.1.

Table 4.1. Comparison of adsorption capacities with similar system.

Support material	Size (mm)	Iron loading (wt. %)	Iron phase	Maximum adsorption capacity ($mg \cdot g^{-1}$)	Reference
Cellulose sponge	cube (13 x 10 x 7)	1.80	γ-Fe_2O_3	69.68*	This work
Sponge	half-cylinder (30 Ø x 15)	~12	iron oxide	4.6	[10]
NONE	0.3~2	52~62	$Fe(OH)_3$; β-FeO(OH)	25.24	[11]
Corn straw biochar	0.5~1	6.05	Fe	6.80	[12]
Activated carbon	0.85	3.5	iron oxyhydroxides	4.96	[13]
Red oak biochar	<0.04	59.64	Zero-valent iron	15.66	[14]
Switchgrass biochar	<0.04	55.72	Zero-valent iron	6.48	[14]
Clay-activated carbon	2-3	-	iron oxide	5.0	[15]
Fungal biomass	<0.4	-	iron oxide	10.3	[16]
Darco 20 X 50	0.3~0.85	4.22	β-FeOOH	1.95	[17]

(*) at 200 $mg \cdot L^{-1}$

For example, Bakshi and coworkers reported a maximum adsorption capacity of 15.66 $mg \cdot g^{-1}$ when loading 59.64 wt.% zero-valent iron on red oak biochar (particle size < 0.04 mm) [18]. A widely used iron-hydroxide based granulate commercial adsorbent GEH-102 ($Fe(OH)_3$ and β-FeO(OH), size 0.3~2 mm) shows a maximum As(V) adsorption capacity of 25.24 $mg \cdot g^{-1}$ [11]. In our case, the mass fraction of the iron nanoparticulate adsorbent loaded is much lower than in those works, and, in addition, we are not quoting the calculated

maximum adsorption capacity as it is usually reported by several authors. In this study, for a maximum initial As(V) concentration of 800 $mg \cdot L^{-1}$ an adsorption capacity of 69.68 $mg \cdot g^{-1}$ is obtained for sponge-loaded SPION which outperforms those other Fe-based adsorbents.

Table 4.2. Adsorption capacity compare and analysis of different adsorbents.

Adsorbent	Adsorption capacity ($mg \cdot g^{-1}$)		Variation as temperature increases (%)
	293 K	343 K	
SPION	27.7	33.7	21.7
sponge	18.7	14.2	-24.1
sponge-loaded SPION	24.0	21.7	-9.6
sponge in composite material	18.3	13.9	-24.0
SPION in composite material	5.7	7.9	38.6
2.6 wt.% of aggregated SPION	0.7	0.9	28.6
sponge + 2.6 wt.% of aggregated SPION	18.9	14.7	-22.2

The independent adsorption performance of SPION supported in the sponge can be assessed when the adsorption capacities of the two materials forming the composite adsorbent are disentangled. When comparing with the adsorption capacity of the SPION sample, 27.7 $mg \cdot g^{-1}$, we found that, in proportion, the supported SPION adsorbs ~8 times more As(V) than the unsupported nanoparticles. This reflects the reduction of the surface area due to the aggregation of the unsupported nanoparticles in the SPION samples as it has been shown above in the SEM images. Indeed, the different behavior of the SPION when loaded in the sponge is also reflected in the temperature variation of the adsorption capacity. For SPION sample, there is a 21.7% adsorption increase when going from 293 to 343 K, whereas the SPION loaded in the sponge displays a larger increase, 38.6%, see Table 4.2. This explains why the temperature variation of the whole composite adsorbent decreases less, -

9.6%, than the value that can be proportionally estimated from the individual components, -22.2%.

4.3. Adsorption isotherm and kinetic study

4.3.1 Isotherm modeling

Adsorption isotherms were measured to understand the adsorption mechanism of cube sponge-loaded SPION. For modeling, the adsorption of heavy metals and metalloids from aqueous solution, Langmuir, Freundlich, and Temkin are the most commonly used isotherm models because of the usefulness of their parameters, their simplicity, and their easy interpretability. The forms of those three models are displayed in Annex I.

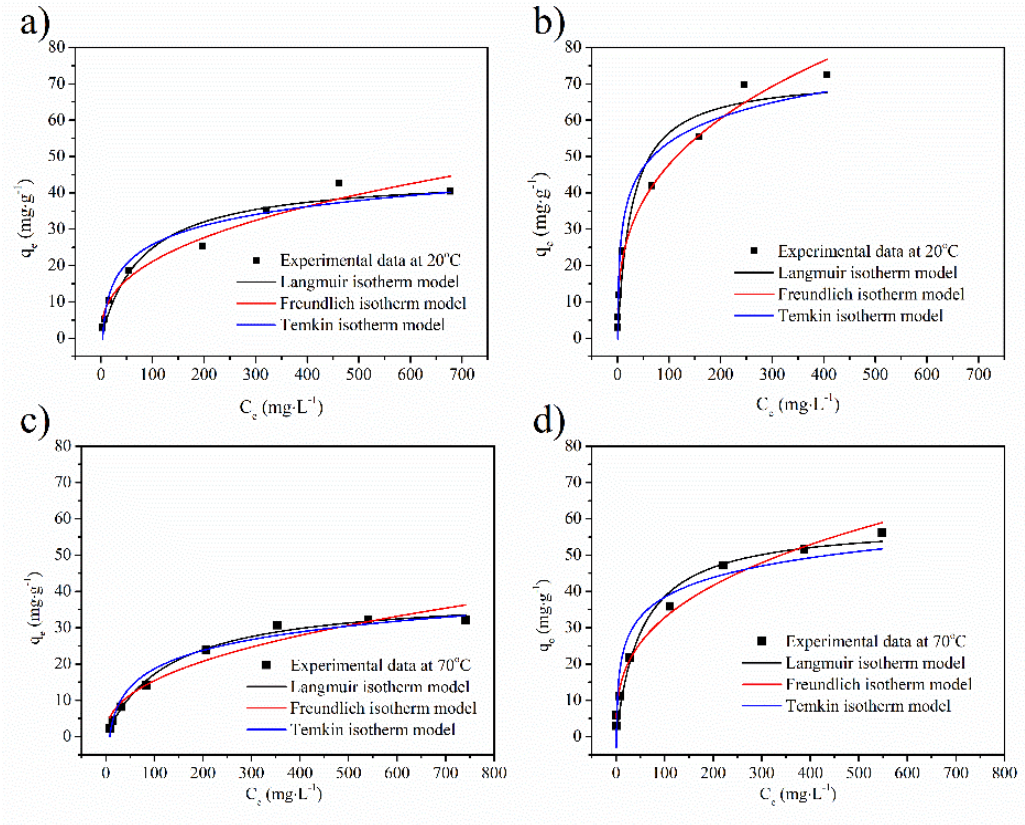

Figure 4.2. Isotherm fitting of experimental data: sponge at 293 K (a), sponge-loaded SPION at 293 K (b), sponge at 343 K (c), and sponge-loaded SPION at 343 K (d).

The adsorption isotherm data of sponge and sponge-loaded SPION at 293 and 343 K were fitted to these models, see Figure 4.2. The results from the fits are displayed in Table 4.3. A relatively good fit was found for the three models (R^2 >0.90), however, the best model is Freundlich which highlights the importance of the heterogeneous surface of the adsorbents. In Freundlich isotherm model, the values of $\frac{1}{n}$ are less than 1 for both adsorbents which indicates that the As(V) adsorption is favorable for both materials. Besides, significant higher K_F values for the sponge-loaded SPION system at both temperatures means that adsorption capacity increased after loading the nanoparticles.

Table 4.3. The parameters of different isotherms models for sponge and sponge-loaded SPION. The parameters are expressed in the following units: T (K), q_m (mg·g^{-1}), K_L (L·mg^{-1}), K_F [(mg·g^{-1}) (L·mg^{-1})$^{1/n}$], A_T (L·g^{-1}), b_T (K·Jmol^{-1}).

Adsorbents	T	Langmuir isotherm			Freundlich isotherm			Temkin isotherm		
		q_m	K_L	R^2	K_F	1/n	R^2	A_T	b_T	R^2
sponge	293	45.00	0.012	0.95	3.49	0.39	0.96	0.31	0.32	0.95
	343	39.36	0.008	0.99	2.16	0.43	0.94	0.13	0.39	0.97
Sponge-loaded SPION	293	72.24	0.036	0.94	10.12	0.34	0.98	2.21	0.24	0.96
	343	58.97	0.019	0.98	6.69	0.35	0.98	1.35	0.36	0.93

4.3.2 Kinetic modeling

Kinematic parameters are important to determine the efficiency and mechanism of the adsorption process [22]. To study the rate and mechanism of As(V) adsorption onto sponge-loaded SPION, the experimental kinetic data were fitted to the pseudo-first order kinetic model and pseudo-second order kinetic model. The forms of those two models are displayed in Annex II.

Sponge and sponge-loaded SPION adsorption data at 293 and 343 K were fitted to these kinetic models, see Figure 4.3. Regression coefficients and rate constants are shown in Table 4.4.

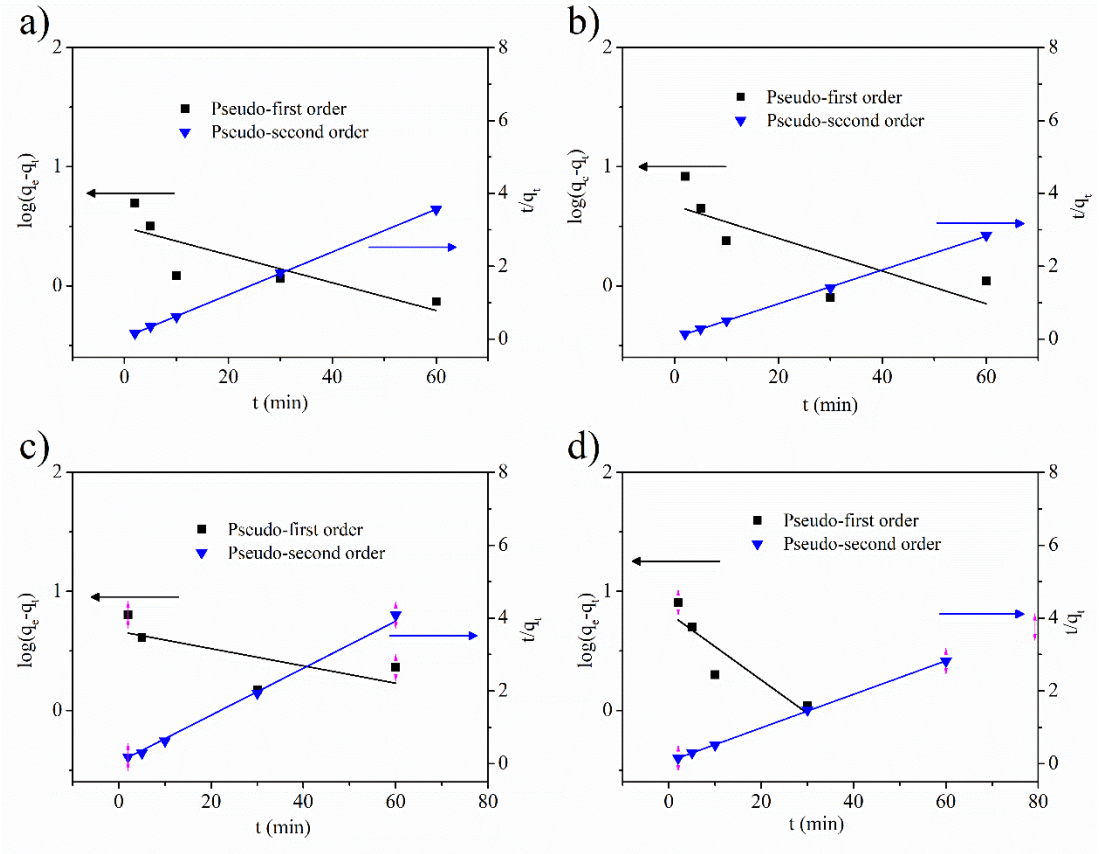

Figure 4.3. Kinetic models for As(V) adsorption: sponge at 293 K (a), sponge-loaded SPION at 293 K (b), sponge at 343 K (c), and sponge-loaded SPION at 343 K (d).

The regression coefficients of the pseudo-second order model are higher than 0.99 for both sponge and sponge-loaded SPION, while regression coefficients of pseudo-first order were below 0.80. Hence, the adsorption kinetics of both systems are better described by the pseudo-second order model. Therefore, chemisorption is controlling the speed of the adsorption process. FT-IR results in chapter 3.4.2 confirm the existence of free available hydroxyl group (-OH),

ethyleneamine (-NH_2-CH_2-CH_2-) and iminodiacetate (–(C=O)-NH-(C=O)-) groups in the adsorbents. This implies the influence of ligand exchange and ion exchange mechanisms through the sharing/exchange of electrons between adsorbent functional groups and As(V) during adsorption [23,24].

Table 4.4. Kinetic parameters for As(V) adsorption by sponge and sponge-loaded SPION.

Adsorbent	Temperature (K)	Pseudo-first order		Pseudo-second order	
		K_1 (min^{-1})	R^2	K_2 ($g \cdot mg^{-1} \cdot min^{-1}$)	R^2
sponge	293	0.0268	0.5671	0.0782	0.9999
	343	0.0167	0.2468	0.0929	0.9964
Sponge-loaded SPION	293	0.0316	0.4977	0.0519	0.9996
	343	0.0645	0.7299	0.0297	0.9997

The activation energy E_a for adsorption of As(V) onto sponge-loaded SPION can be calculated from the pseudo-second order rate constant, K_2, using the following Arrhenius equation [25]:

$$ln\, K_2 = ln\, A - \frac{E_a}{RT} \quad (4.2)$$

where K_2 is the adsorption rate constant, A is the Arrhenius constant, E_a ($kJ \cdot mol^{-1}$) is the activation energy, R is the ideal gas constant 8.3145 ($J \cdot mol^{-1} \cdot K^{-1}$) and T (K) is the absolute temperature. The E_a values obtained for sponge and sponge-loaded SPION were 9.86 and 17.69 $kJ \cdot mol^{-1}$, respectively. This indicates that sponge-loaded SPION shows higher dominance of chemical adsorption than sponge.

4.4. Thermodynamics analysis

Thermodynamic parameters such as Gibbs' free energy change (ΔG^o), enthalpy

change (ΔH^o) and entropy change (ΔS^o) can predict the feasibility and nature of the adsorption process [25]. The relations of these thermodynamic parameters are displayed in Annex III.

By constructing a plot of $ln\,K$ versus $1/T$, $\Delta S°$ can be calculated from the intercept and $\Delta H°$ can be obtained from the slope. The results are displayed in Figure 4.4 and Table 4.5.

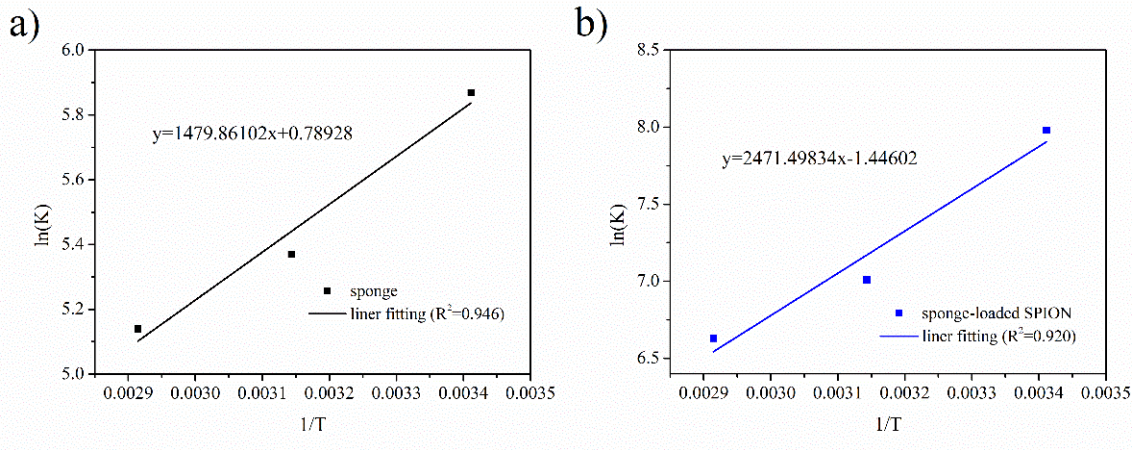

Figure 4.4. Results from fitting analysis for determining $\Delta S°$ and $\Delta H°$: sponge (a); sponge-loaded SPION (b).

Table 4.5. Thermodynamic parameters for As(V) adsorption onto the sponge and sponge-loaded SPION.

Adsorbent	Temperature (K)	ΔG^o (kJ·mol^{-1})	ΔH^o (kJ·mol^{-1})	ΔS^o (J·mol^{-1})
sponge	293	-14.22	-12.30	6.56
	318	-14.39		
	343	-14.55		
sponge-loaded SPION	293	-19.28	-22.80	-12.02
	318	-18.98		
	343	-18.68		

The negative ΔG^o values obtained for sponge and sponge-loaded SPION at

three temperatures indicate that the adsorption of As(V) onto both adsorbent materials is spontaneous. Values of $\Delta H°$ are -12.30 and -22.80 $kJ \cdot mol^{-1}$ for sponge and sponge-loaded SPION respectively, which indicates the As(V) adsorption on these two adsorbents is an exothermic process. The loading of 2.6 wt.% SPION on sponge did not change the exothermic nature of As(V) adsorption on the sponge, although the adsorption on iron oxide is an endothermic process as previously reported [27]. The spontaneous and exothermic nature of As(V) adsorption imply that adsorption of As(V) on the adsorbents is favorable, which agrees with the results obtained from fitting of Freundlich model.

4.5. Chemical state of As determined by XAS

Although the study of the macroscopic adsorption behavior and the thermodynamic calculations provides some evidence that the arsenic is chemically adsorbed on sponge and sponge-loaded SPION, information about the oxidation state and coordination environment of As after being adsorbed is still missing. As K-edge XAS measurements were performed to get a better insight of the adsorption process at the molecular scale.

Figure 4.5a displays the As K-edge XANES spectra collected on the adsorbent materials and the As reference compounds (arsenic trioxide, As(III); and arsenic pentoxide, As(V)). These two As reference compounds display a markedly different spectral profile. The pentoxide is shifted ~3.7 eV towards higher energy respect to the trioxide. Thus, the white-line feature (first resonance after the rising absorption edge) appears at 11875.5 and 11871.7 eV for pentoxide and trioxide, respectively. The direct comparison of the spectra collected on the adsorbent samples with the As reference compounds reveals that the arsenic adsorbed in the materials remains as As(V). Hence, no major redox reaction occurred upon As(V) adsorption on any of the materials. The

spectral feature after the white line appears at different energy for sponge and SPION reflecting the different coordination environment of As(V) in the two adsorbents. As expected, the spectrum for the composite adsorbent sample, sponge-loaded SPION, lies in between the two, being more similar to sponge due to the low nanoparticles loading. As shown in Figure 4.6, the XANES spectra do not change much when increasing the adsorption temperature from 293 to 343 K, therefore, the temperature does not affect much the oxidation state of the adsorbed As. In addition, no change in the oxidation state of the adsorbed As was found as a function of the penetration depth of the cube neither in sponge nor in sponge-loaded SPION, see Figure 4.6. Hence, the same adsorption process takes place at the different parts of the cube due to the good diffusion properties of the sponge material and the rather homogeneity of the composite adsorbent material.

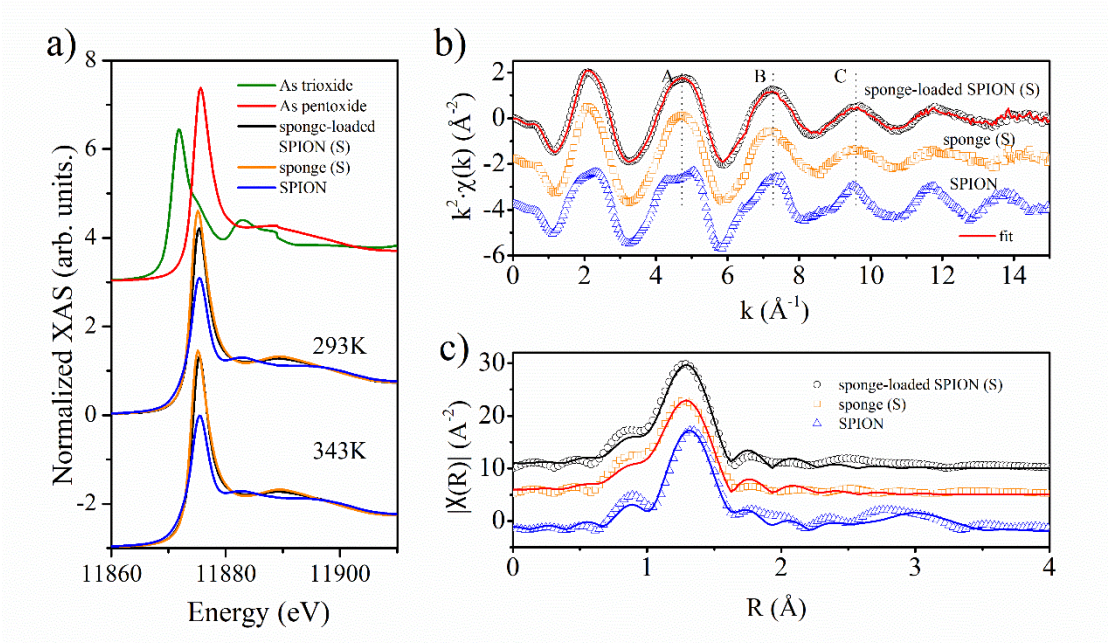

Figure 4.5. As K-edge XAS spectra of SPION, sponge and sponge-loaded SPION after adsorbing As(V): (a) XANES spectra collected on the adsorbent materials and the As reference compounds; (b) EXAFS spectra for adsorbents after As(V) adsorption at 293K and results of the linear combination fitting

analysis for surface part of sponge-loaded SPION (line); (c) Pseudo-radial distribution function for adsorbents after As(V) adsorption at 293 K. (symbols are experimental data and lines are fits.)

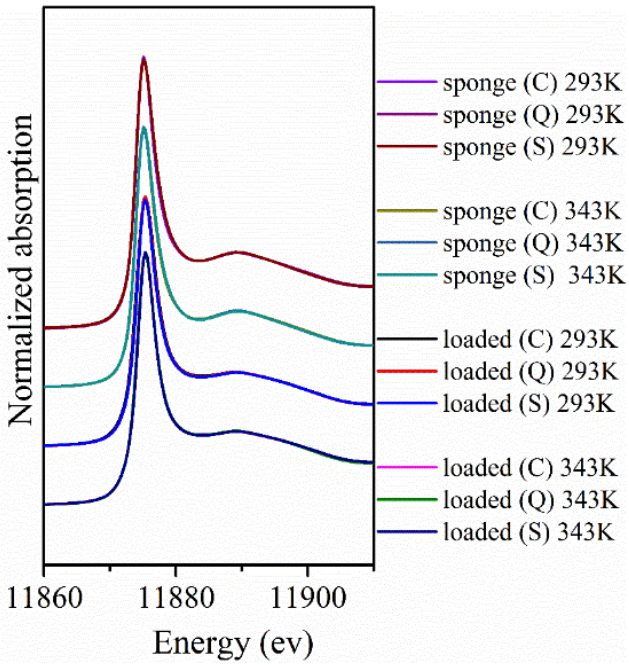

Figure 4.6. As K-edge XANES of sponge and sponge-loaded SPION at different penetration depth and As(V) adsorption temperatures.

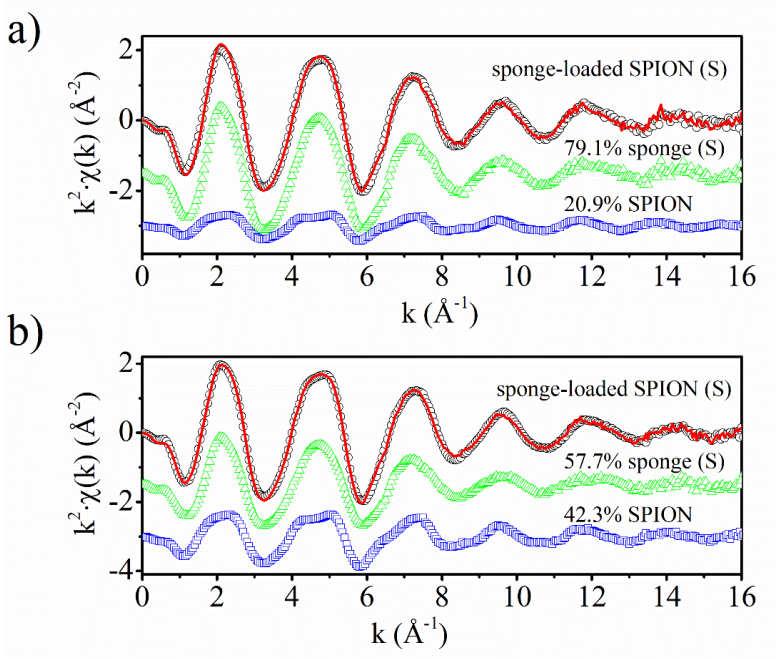

Figure 4.7. Results from the linear combination fitting analysis of the EXAFS

signal of sponge-loaded SPION (S) for As(V) adsorption at 293 (a) and 343 K (b) by using the spectra of sponge (S) and SPION as references. (Symbols are experimental data and lines are fits.)

Table 4.6. EXAFS fitting results of SPION, sponge (S) and loaded (S) at 293K.

Sample	Atomic Pairs	S_0^2	CN	R(Å)	σ^2 (Å^2)	ΔE_0 (eV)	R-factor
SPION	As-O	0.85	4	1.70 (0.02)	0.001 (0.0005)	5.7 (1.1)	0.031
	As-O-O		12	1.82*(R_{As-O}) =3.10	σ^2(As-O)		
	As-Fe		2	3.39 (0.04)	0.004 (0.003)		
sponge (S)	As-O	1.1	4	1.69 (0.01)	0.003 (0.001)	5.4 (1.8)	0.009
loaded (S)	As-O	1.1	4	1.69 (0.01)	0.004 (0.002)	5.9 (2.0)	0.010

The different local coordination environment of As in SPION and sponge adsorbents is more evident when representing the EXAFS signal and the pseudo-radial distribution function, Figure 4.5b and 4.5c, respectively. SPION displays a more structured EXAFS signal than sponge. As can be seen in Figure 4.5b, feature A from sponge is a double feature in SPION, and features B and C are sharper and have a shoulder at lower k for SPION whereas those features are smoother in the case of sponge. As expected, the EXAFS for the sponge-loaded SPION is similar to the one for sponge, but it has some resemblance to SPION as can be noticed by the slight flattening of feature A and the change in shape of features B and C. A semiquantitative analysis of the ratio between the two components, sponge and SPION, in the sponge-loaded SPION sample can be obtained from the linear combination fitting analysis of the EXAFS signal. The results show that, at 293 K, around 21% of As(V) is adsorbed into the loaded nanoparticles (Figure 4.5b and Figure 4.7a), whereas this amount

increases to ~42% at 343 K (see Figure 4.7b). These results are in good agreement with those obtained from the adsorption data reported above and confirm that the As(V) adsorbed on the loaded nanoparticles increases when increasing the temperature.

The Fourier-transformed spectra in R-space, see Figure 4.4c, is dominated by the As−O first-neighbor contribution. The modelling of the EXAFS signals revealed that the As-O bond distance in sponge and SPION are 1.69 and 1.70 Å, respectively (see section S12 for further details about the EXAFS modelling). In addition, for SPION and sponge-loaded SPION, there are relatively weak features beyond the first coordination shell that can be attributed to the As−Fe contributions. The different arrangements of the As(V) tetrahedron with the surface of the iron oxide nanoparticle are related to the arsenic surface coverage [28,29]. Among all, binuclear corner-sharing, ^{2}C, is found to be the dominant configuration, because it is strongly favored thermodynamically and kinetically, and it is also the most energetically stable. Some authors have reported the presence of the mononuclear corner-sharing, ^{1}V, when arsenic has a relatively low surface coverage, but we can safely exclude this possibility in our case. The mononuclear edge-sharing configuration, ^{2}E, is reported to be present in some cases with the high arsenic surface coverage. In our study, the high initial concentration of arsenic (200 mg·L^{-1}) and the good affinity of SPION for As(V) results in a high surface coverage. The fitting results are compatible with a dominant contribution of the ^{2}C configuration (see Table 4.6). In this case, two of the four As–O bonding structures are complexed to Fe atoms (i.e., As–O–Fe) by corner-sharing with the FeO_6 octahedron and the remaining two As atoms are present either both as unprotonated As–O or one as unprotonated As–O and the other one as protonated As–O–H [30]. Despite the differences regarding particle aggregation, both SPION and sponge-loaded SPION samples are composed by maghemite and it can be assumed that the

coordination on the composite will follow similar trend as in the case of the unsupported nanoparticles.

4.6. Life-cycle investigation

To assess the regeneration capacity of cube sponge-loaded SPION, several cycles of adsorption and desorption experiments were performed. As shown in Figure 4.8, the adsorption capacity of adsorbent did not show a significant decrease. Hence, the cube adsorbent maintains a high adsorption capacity even after five adsorption/desorption cycles. The slightly increase observed for the fourth and fifth cycles, can be ascribed to the loose powder which broke off from the sponge-loaded SPION during shaking which contributes to the increase of the effective As adsorption from the solution. Besides its good regeneration capabilities, one of the main benefits of this composite adsorbent is that, after its life-time span, it could be easily compressed into a very small volume which hugely facilitates its transport and ultimately waste disposal.

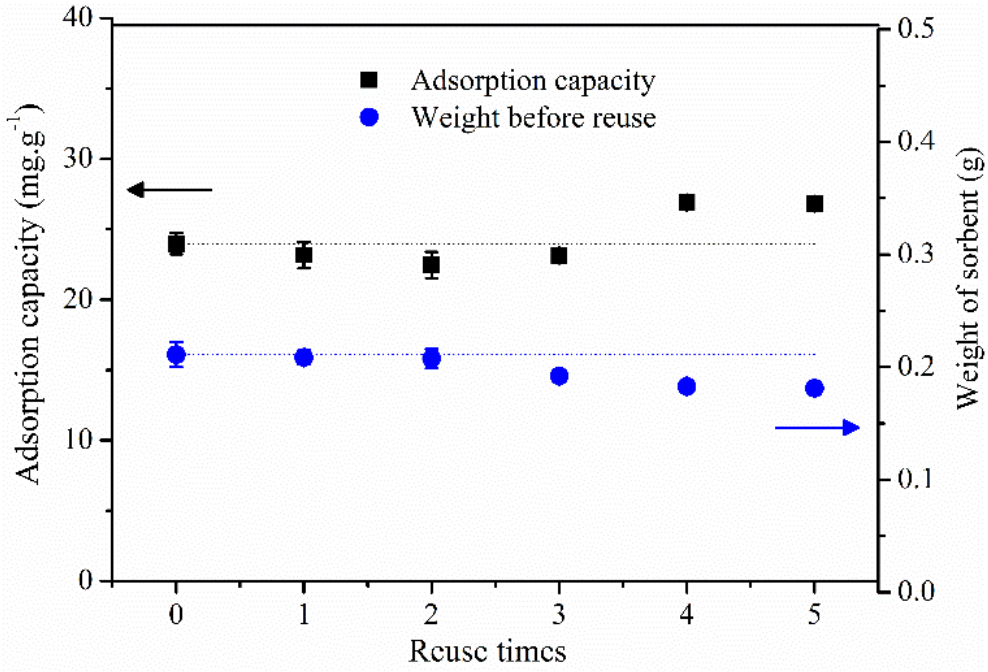

Figure 4.8. The weight and adsorption capacity of adsorbent in different regeneration circle.

4.7. Conclusions

Batch adsorption experiments showed the adsorption capacity of sponge had a 28.3% enhancement after loading 2.6 wt.% mass fraction of SPION. Cube sponge-loaded SPION had a higher adsorption capacity compared with similar system adsorbents reported.

The adsorption of As(V) by sponge-loaded SPION fitted well by Freundlich isotherm, indicating a multilayer and heterogeneous adsorption. Kinetic studies showed As(V) adsorption followed pseudo-second order kinetic model, suggesting chemical adsorption was the controlling step. Thermodynamics calculation indicates the adsorption was a spontaneous and exothermic process.

In addition, we have observed that As(V) was not reduced to more toxic As(III) after adsorbed on the surface of adsorbents, which is desirable for the treatment of As(V) contaminated waters. The modeling of the EXAFS signals revealed that the binuclear corner-sharing, ^{2}C, configuration is the main one. Moreover, we have shown that the cube-shaped sponge-loaded SPION has good regenerative performance and can be used over several adsorption/desorption cycles.

4.8. Reference

[1] D. Morillo, A. Uheida, G. Pérez, M. Muhammed, M. Valiente, Arsenate removal with 3-mercaptopropanoic acid-coated superparamagnetic iron oxide nanoparticles, J. Colloid Interface Sci. 438 (2015) 227–234. https://doi.org/10.1016/j.jcis.2014.10.005.

[2] D. Morillo, G. Pérez, M. Valiente, Efficient arsenic(V) and arsenic(III) removal from acidic solutions with Novel Forager Sponge-loaded superparamagnetic iron oxide nanoparticles, J. Colloid Interface Sci. 453 (2015) 132–141. https://doi.org/10.1016/j.jcis.2015.04.048.

[3] A. Shahat, H.M.A. Hassan, H.M.E. Azzazy, M. Hosni, M.R. Awual, Novel nano-conjugate materials for effective arsenic(V) and phosphate capturing in aqueous media, Chem. Eng. J. 331 (2018) 54–63. https://doi.org/10.1016/j.cej.2017.08.037.

[4] M. Navarrete-Magaña, A. Estrella-González, L. May-Ix, S. Cipagauta-Díaz, R. Gómez, Improved photocatalytic oxidation of arsenic (III) with WO3/TiO2 nanomaterials synthesized by the sol-gel method, J. Environ. Manage. 282 (2021) 111602. https://doi.org/10.1016/j.jenvman.2020.111602.

[5] L. Simonelli, C. Marini, W. Olszewski, M. Ávila Pérez, N. Ramanan, G. Guilera, V. Cuartero, K. Klementiev, CLÆSS: The hard X-ray absorption beamline of the ALBA CELLS synchrotron, Cogent Phys. 3 (2016) 1231987. https://doi.org/10.1080/23311940.2016.1231987.

[6] B. Ravel, M. Newville, ATHENA, ARTEMIS, HEPHAESTUS: Data analysis for X-ray absorption spectroscopy using IFEFFIT, J. Synchrotron Radiat. 12 (2005) 537–541. https://doi.org/10.1107/S0909049505012719.

[7] K. Kitahama, R. Kiriyama, Y. Baba, Refinement of the crystal structure of scorodite, Acta Crystallogr. Sect. B Struct. Crystallogr. Cryst. Chem. 31 (1975) 322–324. https://doi.org/10.1107/s056774087500266x.

[8] C.M. Van Genuchten, S.E.A. Addy, J. Peña, A.J. Gadgil, Removing arsenic from synthetic groundwater with iron electrocoagulation: An Fe and As K-edge EXAFS study, Environ. Sci. Technol. 46 (2012) 986–994. https://doi.org/10.1021/es201913a.

[9] W. Ali, A. Rasool, M. Junaid, H. Zhang, A comprehensive review on current status, mechanism, and possible sources of arsenic contamination in groundwater: a global

perspective with prominence of Pakistan scenario, Environ. Geochem. Health. 41 (2019) 737–760. https://doi.org/10.1007/s10653-018-0169-x.

[10] T.V. Nguyen, S. Vigneswaran, H.H. Ngo, J. Kandasamy, Arsenic removal by iron oxide coated sponge: Experimental performance and mathematical models, J. Hazard. Mater. 182 (2010) 723–729. https://doi.org/10.1016/j.jhazmat.2010.06.094.

[11] B. Moraga, L. Toledo, L. Jelínek, J. Yañez, B.L. Rivas, B.F. Urbano, Copolymer–hydrous zirconium oxide hybrid microspheres for arsenic sorption, Water Res. 166 (2019) 115044. https://doi.org/10.1016/j.watres.2019.115044.

[12] R. He, Z. Peng, H. Lyu, H. Huang, Q. Nan, J. Tang, Synthesis and characterization of an iron-impregnated biochar for aqueous arsenic removal, Sci. Total Environ. 612 (2018) 1177–1186. https://doi.org/10.1016/j.scitotenv.2017.09.016.

[13] C. Nieto-Delgado, J. Gutiérrez-Martínez, J.R. Rangel-Méndez, Modified activated carbon with interconnected fibrils of iron-oxyhydroxides using Mn 2 + as morphology regulator, for a superior arsenic removal from water, J. Environ. Sci. (China). 76 (2019) 403–414. https://doi.org/10.1016/j.jes.2018.06.002.

[14] S. Bakshi, C. Banik, S.J. Rathke, D.A. Laird, Arsenic sorption on zero-valent iron-biochar complexes, Water Res. 137 (2018) 153–163. https://doi.org/10.1016/j.watres.2018.03.021.

[15] R.R. Pawar, Lalhmunsiama, M. Kim, J.G. Kim, S.M. Hong, S.Y. Sawant, S.M. Lee, Efficient removal of hazardous lead, cadmium, and arsenic from aqueous environment by iron oxide modified clay-activated carbon composite beads, Appl. Clay Sci. 162 (2018) 339–350. https://doi.org/10.1016/j.clay.2018.06.014.

[16] J.F. Cárdenas-González, I. Acosta-Rodríguez, Y. Téran-figueroa, A.S. Rodríguez-Pérez, Bioremoval of arsenic (V) from aqueous solutions by chemically modified fungal biomass, 3 Biotech. 7 (2017) 226. https://doi.org/10.1007/s13205-017-0868-5.

[17] Q. Chang, W. Lin, W. chi Ying, Preparation of iron-impregnated granular activated carbon for arsenic removal from drinking water, J. Hazard. Mater. 184 (2010) 515–522. https://doi.org/10.1016/j.jhazmat.2010.08.066.

[18] S. Bakshi, C. Banik, S.J. Rathke, D.A. Laird, Arsenic sorption on zero-valent iron-biochar complexes, Water Res. 137 (2018) 153–163. https://doi.org/10.1016/j.watres.2018.03.021.

[19] H.N. Tran, S.J. You, A. Hosseini-Bandegharaei, H.P. Chao, Mistakes and inconsistencies

regarding adsorption of contaminants from aqueous solutions: A critical review, Water Res. 120 (2017) 88–116. https://doi.org/10.1016/j.watres.2017.04.014.

[20] K.Y. Foo, B.H. Hameed, Insights into the modeling of adsorption isotherm systems, Chem. Eng. J. 156 (2010) 2–10. https://doi.org/10.1016/j.cej.2009.09.013.

[21] Y. Liu, Y. Xiong, P. Xu, Y. Pang, C. Du, Enhancement of Pb (II) adsorption by boron doped ordered mesoporous carbon: Isotherm and kinetics modeling, Sci. Total Environ. 708 (2020) 134918. https://doi.org/10.1016/j.scitotenv.2019.134918.

[22] S. Nethaji, A. Sivasamy, A.B. Mandal, Adsorption isotherms, kinetics and mechanism for the adsorption of cationic and anionic dyes onto carbonaceous particles prepared from Juglans regia shell biomass, Int. J. Environ. Sci. Technol. 10 (2013) 231–242. https://doi.org/10.1007/s13762-012-0112-0.

[23] X. Hu, L. Jia, J. Cheng, Z. Sun, Magnetic ordered mesoporous carbon materials for adsorption of minocycline from aqueous solution: Preparation, characterization and adsorption mechanism, J. Hazard. Mater. 362 (2019) 1–8. https://doi.org/10.1016/j.jhazmat.2018.09.003.

[24] S.K. Singh, T.G. Townsend, D. Mazyck, T.H. Boyer, Equilibrium and intra-particle diffusion of stabilized landfill leachate onto micro- and meso-porous activated carbon, Water Res. 46 (2012) 491–499. https://doi.org/10.1016/j.watres.2011.11.007.

[25] E.C. Lima, A. Hosseini-Bandegharaei, J.C. Moreno-Piraján, I. Anastopoulos, A critical review of the estimation of the thermodynamic parameters on adsorption equilibria. Wrong use of equilibrium constant in the Van't Hoof equation for calculation of thermodynamic parameters of adsorption, J. Mol. Liq. 273 (2019) 425–434. https://doi.org/10.1016/j.molliq.2018.10.048.

[26] T. Chen, T. Da, Y. Ma, Reasonable calculation of the thermodynamic parameters from adsorption equilibrium constant, J. Mol. Liq. 322 (2021) 114980. https://doi.org/10.1016/j.molliq.2020.114980.

[27] C.H. Liu, Y.H. Chuang, T.Y. Chen, Y. Tian, H. Li, M.K. Wang, W. Zhang, Mechanism of Arsenic Adsorption on Magnetite Nanoparticles from Water: Thermodynamic and Spectroscopic Studies, Environ. Sci. Technol. 49 (2015) 7726–7734. https://doi.org/10.1021/acs.est.5b00381.

[28] C.M. van Genuchten, T. Behrends, S.L.S. Stipp, K. Dideriksen, Achieving arsenic concentrations of <1 μg/L by Fe(0) electrolysis: The exceptional performance of magnetite, Water Res. 168 (2020). https://doi.org/10.1016/j.watres.2019.115170.

[29] C. Mikutta, J. Frommer, A. Voegelin, R. Kaegi, R. Kretzschmar, Effect of citrate on the local Fe coordination in ferrihydrite, arsenate binding, and ternary arsenate complex formation, Geochim. Cosmochim. Acta. 74 (2010) 5574–5592. https://doi.org/10.1016/j.gca.2010.06.024.

[30] K. Zhao, H. Guo, Behavior and mechanism of arsenate adsorption on activated natural siderite: Evidences from FTIR and XANES analysis, Environ. Sci. Pollut. Res. 21 (2014) 1944–1953. https://doi.org/10.1007/s11356-013-2097-8.

Chapter 5: As(III) adsorption-oxidation mechanism studies on cube sponge-loaded SPION

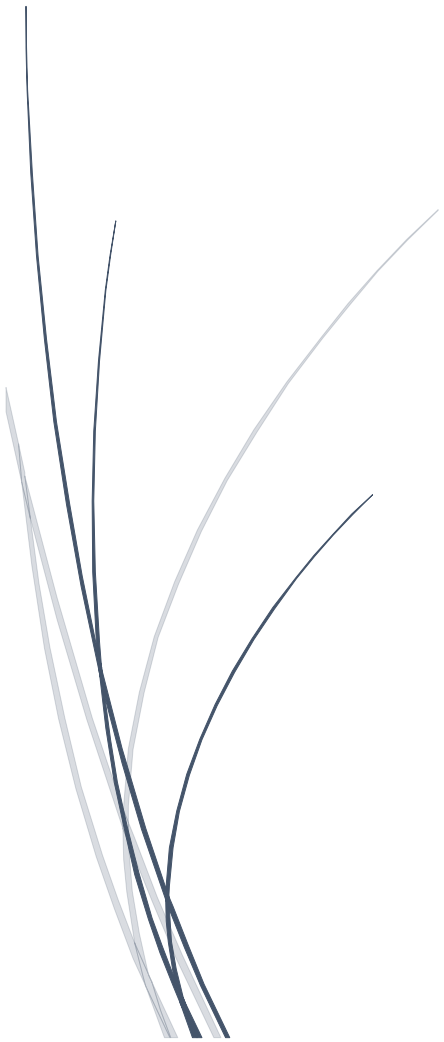

5.1. Materials and methodology

5.1.1 Chemical reagent

All reagents used were of analytical grade. Sodium arsenite ($NaAsO_2$) was used as the source of As(III). A 1000 $mg \cdot L^{-1}$ As(III) stock solution was initially prepared, and then diluted to the required concentration. Hydrogen chloride (HCl) and sodium hydroxide (NaOH) were used to adjust the pH during adsorption experiments.

When doing the detection of As(III) concentration by UV-vis, potassium permanganate (KMnO4) was used to oxidized As(III) to As(V) firstly. Ammonium molybdate, $(NH_4)_6Mo_7O_{24} \cdot 4H_2O$]; antimony potassium tartrate $C_8H_4K_2O_{12}Sb_2 \cdot 1/2H_2O$; sulfuric acid, H_2SO_4; and ascorbic acid, $C_6H_8O_6$; were used as color reagents for the detection of As(V) by molybdenum blue method as described elsewhere [1,2].

5.1.2 Adsorption experiments

Adsorption experiments were performed by putting 0.20 g adsorbent (SPION, cube sponge, cube sponge-loaded SPION) in contact with 25.0 ml of As(III) solution. The tubes were agitated mechanically at 300 rpm using a rotary shaker. Different temperature experiments were performed by putting the shaker inside of an incubator. Adsorption experiments of different initial concentrations were performed with concentrations ranging 10~1000 $mg \cdot L^{-1}$ As(III) at pH 7 shaking during 120 mins; experiments of different contact time were performed with 1~480 mins shaking at pH 7 and 200 $mg \cdot L^{-1}$ initial concentration; experiments of different pH values were performed by adjusting pH from 3~10 with 200 $mg \cdot L^{-1}$ initial concentration and agitating during 120 mins.

After adsorption, SPION were magnetically separated, and sponge and sponge-loaded SPION were separated by filtration. As(III) concentration in the solution was first oxidized to As(V) by adding potassium permanganate ($KMnO_4$) solution, and then, the As(V) concentration was determined by UV-visible spectrometric technique based on the molybdenum blue method (See section S4 in SI). The adsorption capacity at equilibrium was calculated using the following equation:

$$q_e = (C_o - C_e)\frac{V}{m} \quad (5.1)$$

where q_e ($mg \cdot g^{-1}$) is the adsorption capacity, V (L) is the volume of the arsenic solution, m (g) is the dry weight of the adsorbent, C_o and C_e ($mg \cdot L^{-1}$) are initial and equilibrium concentrations of As(III) solution, respectively.

5.1.3 Isotherm and kinetic models

To better understand and explain the As(III) adsorption behaviors, different isotherm and kinetic models were used. Experimental data of different initial concentrations were fitted to Langmuir, Freundlich and Temkin isotherm models. The forms of those three models are displayed in Annex I. Experiment data of different contact times were fitted to pseudo-first order and pseudo-second order. The forms of those two kinetic models are displayed in Annex II.

5.1.4 Determination of As(III) concentration by UV-Visible

There are two steps in the detection of As(III) by UV-vis spectra. First it is the oxidation of As(III) to As(V) by potassium permanganate ($KMnO_4$); Second it is the As(V) detection by molybdenum blue method.

5.1.4.1 Oxidation of As(III) to As(V) by KMnO4

a) Stander solutions and samples prepared: 10 ml As(III) stander solutions

(0.05, 1, 2, 3, 4, 5 mg·L^{-1}) were firstly prepared. All the samples were also diluted to prepared 10 ml solutions with the concentration range of 0.5~5 mg·L^{-1}.

b) 1000 mg·L^{-1} $KMnO_4$ solution was prepared.

c) 0.08 ml $KMnO_4$ solution was added to 10 ml As(III) solutions.

d) Wait at least 30 minutes for the reaction to complete.

5.1.4.2 As(V) detection by molybdenum blue method

a) Color solution A preparation: 6.9 g Ammonium Molybdate [$(NH_4)_6Mo_7O_{24}·4H_2O$] was dissolved in 50 ml Milli-Q water; 0.175 g Antimony Potassium Tartrate was dissolved ($C_8H_4K_2O_{12}Sb_2·1/2H_2O$) in 50 ml Milli-Q water; 150 ml 17.74 mol·L^{-1} Sulfuric Acid (H_2SO_4) was prepared; Three solutions above were mixed together to get the color solution A.

b) Color solution B preparation: 5.0 g Ascorbic acid ($C_6H_8O_6$) was dilute to 50 ml Milli-Q water to get color solution B.

c) Prepare a series of arsenic standard solutions (0, 0.5, 1, 2, 3, 4 mg·L^{-1}) with Milli-Q water. Pipet 8.8 ml of each standard solution into a 10 ml test tube. Then add 0.8 ml color solution A and 0.4 ml color solution B.

d) Dilute the sample concentration in the range of 0.5-4 mg·L^{-1}. Then pipet 8.8 ml of each diluted solution into a 10 ml test tube. Then add 0.8 ml color solution A and 0.4 ml color solution B.

e) After at least 60 minutes of color development, absorbance was detected at 855 nm, using the blank as reference.

5.1.5 As K-edge XAS measurements

X-ray absorption spectroscopy (XAS) technique was used to study the oxidation state of As upon adsorption on the adsorbents (SPION, cube sponge and sponge-loaded SPION). A initial concentration of 200 mg·L^{-1} As(III) and a contact time of 120 mins were used. The effect of the adsorption temperature

was also studied by performing adsorption experiments at 293 and 343 K. After solid-liquid separation and three times washing by Mili-Q water, adsorbents were dried in oven at 50°C for 24 h. Arsenic trioxide, As(III), and arsenic pentoxide, As(V), were used as reference materials. All samples and references were milled and pressed into a pellet for performing the measurements.

The XAS experiment at the As K-edge was carried out at BL22 CLÆSS beamline of ALBA CELLS synchrotron using a Si(311) double crystal monochromator [7]. Measurements of As-adsorbents were performed in fluorescence model, while As references were performed in transmission mode using ionization chambers. A multi-element silicon drift detector with Xspress3 electronics was used for collecting the spectra in fluorescence mode for sponge and SPION samples. To reduce the self-absorption effects, SPION was homogeneously mixed with cellulose using a 1:10 ratio. Special care was taken when setting up the fluorescence mode to minimize the dead-time effect. The measurements were carried out at liquid nitrogen temperature to minimize any radiation damage.

5.1.6 As K-edge XAS peak fitting analysis

XAS data analysis was performed according to standard procedures using ATHENA software of the Demeter package [8]. For the peak fitting analysis of the XANES spectra, the arctangent and Lorentzian functions were used for simulating the absorption step and the white-line peak features of As(III) and As(V) species. This allowed us to assess the variation of the species present in the adsorbent materials upon the As(III) adsorption-oxidation process.

Initially, a peak fitting analysis of the reference compounds was performed to evaluate the ratio between the white-line area and the absorption step of each As species. Two different pairs of references were tested: arsenic trioxide and arsenic pentoxide, and sodium arsenite and sodium arsenate. Arsenic trioxide and arsenic pentoxide were chosen as the final references for the peak fitting

analysis of the samples since the step values obtained from the fitting analysis were closer to 1 than those of the sodium salts references in the energy range used, 11861 – 11879 eV, this is (-10, 8) eV respect to the E_0 of As(III) reference. The inflection point of the arctangent (e_0) was fixed to the maximum of first derivative of the reference material.

To have a better understanding of the ratio between the two As species in terms of the relative intensity of the white-line features, As(III)/As(V). A set of spectra were built by fixing all the parameters of both step and peak functions, and keeping the peak height and step height ratio as determined for the arsenic trioxide and arsenic pentoxide references, ~9.8 and ~14.6, respectively. From that, by adjusting the relative amount of the As species, information about the white-line intensity ratio between species was obtained and the look-up table was built (see Table 5.1). The sum of the step heights was fixed to 1.15 as found for the references.

Table 5.1. Simulation of the white-line (w-l) intensity and white-line intensity ratio between species as function of the As(III) content.

As(III) (%)	w-l As(III)	w-l As(V)	w-l ratio As(III)/As(V)
10	0.838	4.052	0.207
20	1.068	3.740	0.286
30	1.341	3.444	0.389
40	1.581	3.158	0.500
50	1.876	2.86	0.656
60	2.114	2.547	0.830
70	2.363	2.252	1.049
80	2.610	1.974	1.322
90	2.866	1.657	1.730

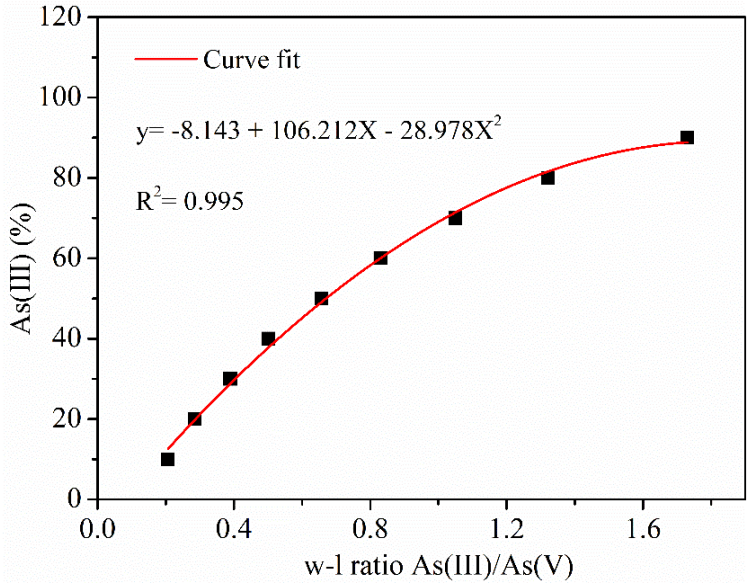

Figure 5.1. Simulation of the white-line (w-l) intensity ratio between species as function of the As(III) content.

Table 5.2. Assume value of the As(III) % and step calculated from the w-l ratio As(III)/As(V). (C, center; Q, quarter; S, surface).

Name	Temperature (K)	w-l ratio As(III)/As(V)	As(III) step	As(V) step
SPION	293	0.85	0.70	0.45
SPION	343	0.96	0.77	0.38
sponge (C)		0.51	0.44	0.71
sponge (Q)	293	0.54	0.47	0.68
sponge (S)		0.63	0.54	0.61
sponge (C)		0.75	0.63	0.52
sponge (Q)	343	0.80	0.67	0.48
sponge (S)		0.97	0.78	0.37
composite (C)		1.25	0.91	0.24
composite (Q)	293	1.25	0.91	0.24
composite (S)		1.25	0.91	0.24
composite (C)		1.31	0.93	0.22
composite (Q)	343	1.31	0.93	0.22
composite (S)		1.31	0.93	0.22

Accordingly, for each sample, the experimental white-line intensity ratio was used to guess the initial values of step height of the two species using the quadratic equation obtained from the fit of the data included in Table 5.1 (see Figure 5.1). The guessed initial data were listed in Table 5.2. Afterwards, the fitting was accomplished by fixing the step height of the species with highest white-line intensity and leaving free in the fit the step height of the other species. In other words, if the As(III)/As(V) white-line intensity ratio was below one, the step height of As(V) was kept fixed, otherwise, if the intensity ratio was over one, the step height of As(III) was kept fixed. In addition, the width of the step function and both the height and the sigma parameters of the peak function were also fitted. In all the cases, the position of the peak (center) and the step (e_0) functions were fixed to the values of the white-line maxima and first derivative of the references, respectively. The fitting was performed iteratively fixing and leaving free these groups of parameters and keeping the peak height to step height ratio of each species closer to the values that were obtained for the reference oxides.

5.2. Adsorption behaviors

Batch experiments were performed to study the adsorption behavior of the materials. Different parameters (initial concentration, contact time, pH values) that affect As(III) adsorption were investigated.

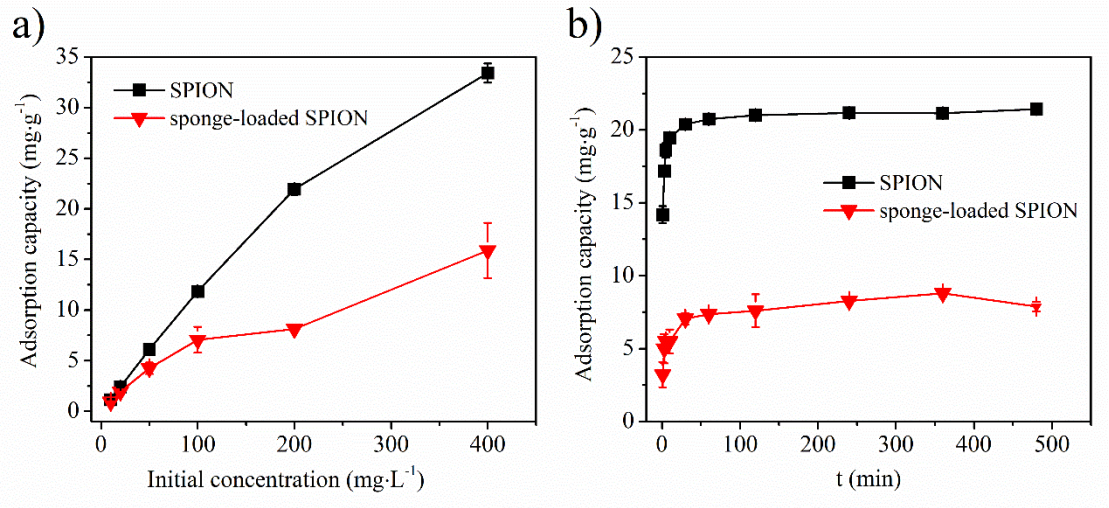

Figure 5.2. As(III) adsorption capacity of sponge and sponge-loaded SPION: initial concentration (a); contact time (b).

As can be seen in Figure 5.2a, the adsorption capacity of SPION and sponge-loaded SPION increased with As(III) initial concentration. Sponge-loaded SPION showed less adsorption capacity than SPION, however, the adsorption of As(III) in sponge can be considered negligible since it was below the detection limit of the colorimetric methodology used. This means that sponge acts mainly as a support for reducing the aggregation of SPION. The less adsorption capacity of the composite material can be explained by the low mass fraction of SPION loaded in the sponge, only 2.6 wt.%. Thus, considering only the mass fraction of SPION in the composite, see Figure 5.3, the adsorption capacity of SPION in composite reached 655.0 $mg \cdot g^{-1}$ with 1000 $mg \cdot L^{-1}$ initial concentration and still not statured. In other words, the SPION loaded in the sponge had 14.5 times adsorption capacity than the unsupported SPION. This difference is due to the nanoparticle aggregation of the unsupported SPION.

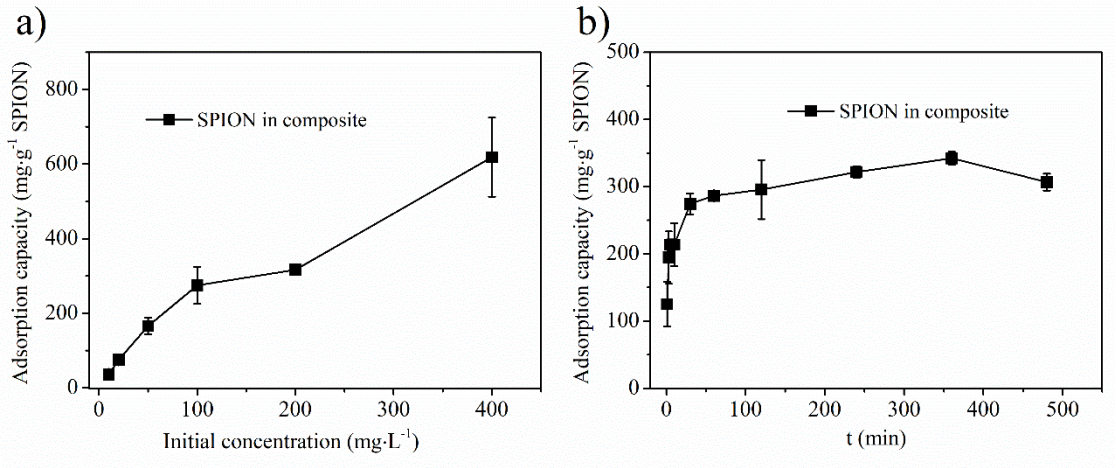

Figure 5.3. As(III) adsorption capacity of SPION in composite material (per gram of SPION): initial concentration (a); contact time (b).

The relationship of adsorption capacities with different contact times was shown in Figure 5.2b. There was a sharp increase in adsorption capacity during the 1-60 minutes. This can be attributed to the large number of adsorption sites initially available on the surface of the adsorbent. Adsorption capacity becomes almost constant after 60 mins. SPION showed a higher equilibrium adsorption capacity (21.0 $mg \cdot g^{-1}$) than sponge-loaded SPION (7.6 $mg \cdot g^{-1}$). When normalizing by the mass fraction of loaded SPION, the adsorption capacity of SPION in the composite material is 295.6 $mg \cdot g^{-1}$. This is 14.1 times higher than unsupported SPION. Furthermore, the adsorption behavior did not show a significant dependence with the pH in the working range, 3.0 to 10.0, see Figure 5.4. This was due to the fact that uncharged H_3AsO_3 (pKa=9.2) is the main species. Therefore, As(III) could not be adsorbed by electrostatic interaction. Similar results were also reported previously. [9,10]

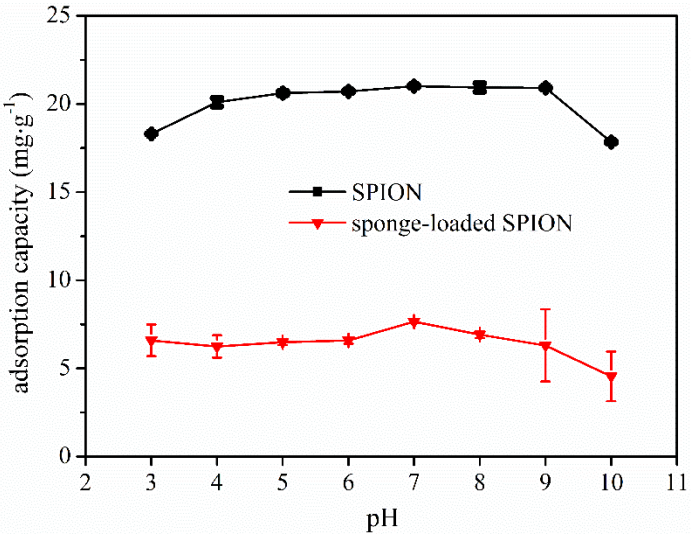

Figure 5.4. As(III) adsorption capacity of SPION and sponge-loaded SPION at different pH values.

5.3. Adsorption isotherm and kinetic study

5.3.1 Isotherm modeling

Langmuir, Freundlich, Temkin isotherm models were used to understand the adsorption behavior for the interaction of As ions on the adsorbent surface. Langmuir model assumes that the adsorption occurs on a homogeneous surface and that all binding sites have equal affinity for the adsorbate [3]. Freundlich isotherm assumes multilayer adsorption, with non-uniform distribution of adsorption heat and affinities over the heterogeneous surface [4]. Temkin isotherm contains a factor that explicitly considers the adsorbent–adsorbate interactions and it is mostly used for electrostatic interaction-based chemical adsorption [5]. The As(III) adsorption isotherms for SPION and sponge-loaded SPION are shown in Figure 5.5. The fitting of isotherm curve for the SPION in the composite is shown in Figure 5.6.

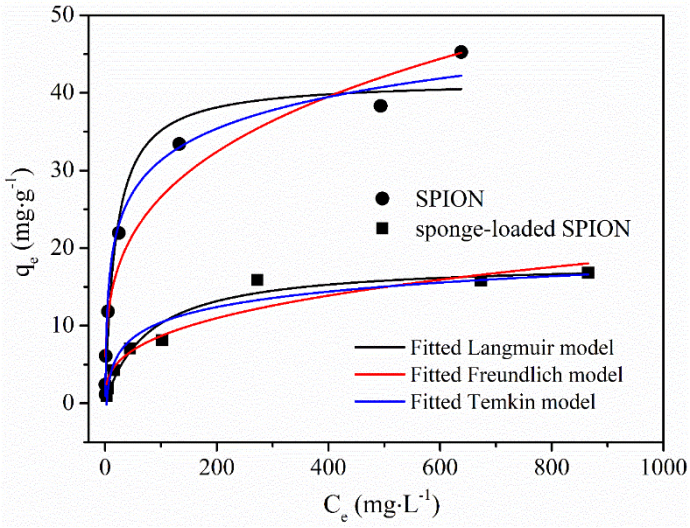

Figure 5.5. As(III) adsorption isotherms for SPION and sponge-loaded SPION at 293K.

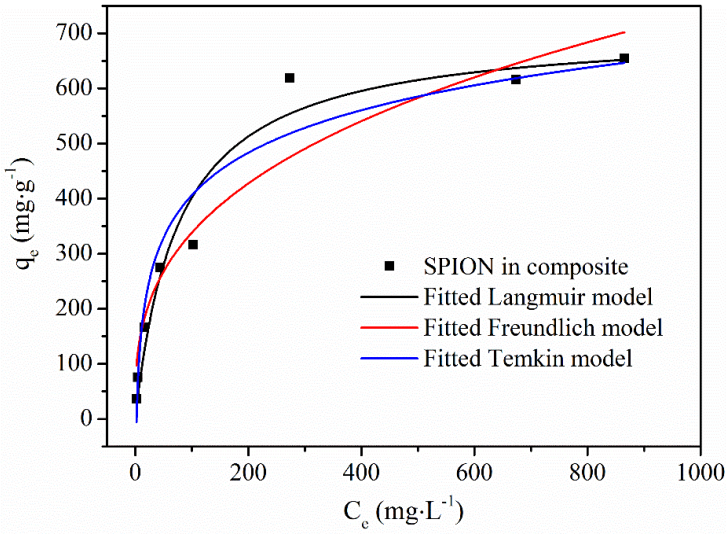

Figure 5.6. As(III) adsorption isotherms for calculated SPION in composite at 293K.

The fitting results are displayed in Table 5.3. For all adsorbents, relatively good fits were found for the three models (R^2 >0.90). However, the best fit would be Temkin model due to the homogeneous property of SPION and heterogeneous property of sponge-loaded SPION and SPION in composite. The good fitting results obtained with the Temkin model emphasized that the interaction is

based on the chemically reaction between As ions and the surface of adsorbents.

Table 5.3. The parameters of different isotherms models for sponge and sponge-loaded SPION. The parameters are expressed in the following units: T (K), q_m (mg·g^{-1}), K_L (L·mg^{-1}), K_F [(mg·g^{-1}) (L·mg^{-1})$^{1/n}$], A_T (L·g^{-1}), b_T (K·Jmol^{-1}).

Adsorbent	Langmuir isotherm			Freundlich isotherm			Temkin isotherm		
	q_m	K_L	R^2	K_F	$\frac{1}{n}$	R^2	A_T	b_T	R^2
SPION	41.67	0.054	0.96	7.11	0.29	0.95	2.05	0.41	0.98
Sponge-loaded SPION	18.24	0.013	0.96	1.82	0.34	0.92	0.38	0.85	0.94
SPION in composite	709.58	0.013	0.96	71.01	0.34	0.92	0.38	0.02	0.94

5.3.2 Kinetic modeling

Kinematic parameters are important to determine the efficiency and mechanism of the adsorption process [3,11]. In this study, pseudo-first order kinetic model and pseudo-second order kinetic model were used. Kinetic fitting of SPION and sponge-loaded SPION were shown in Figure 5.7. The fitting of calculated SPION in composite were shown in Figure 5.8.

Regression coefficients and rate constants are shown in Table 5.4. Kinetics modelling analysis showed that the adsorption process fitted better with pseudo-second order kinetic model for all the adsorbents. Hence, the As(III) adsorption kinetics by these three adsorbents are better described by the pseudo-second order model, which means that chemisorption is driving the speed of the adsorption process.

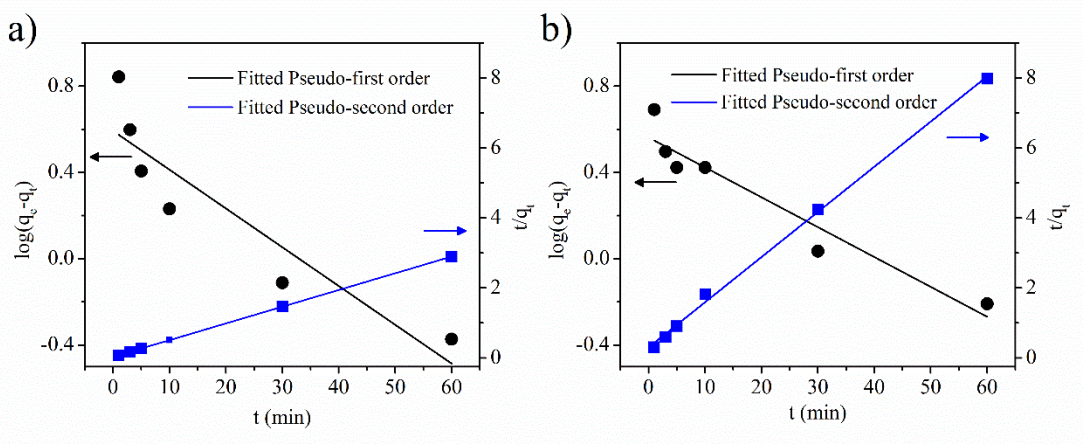

Figure 5.7. Kinetic models for As(III) adsorption at 293 K for SPION (a) and sponge-loaded SPION (b).

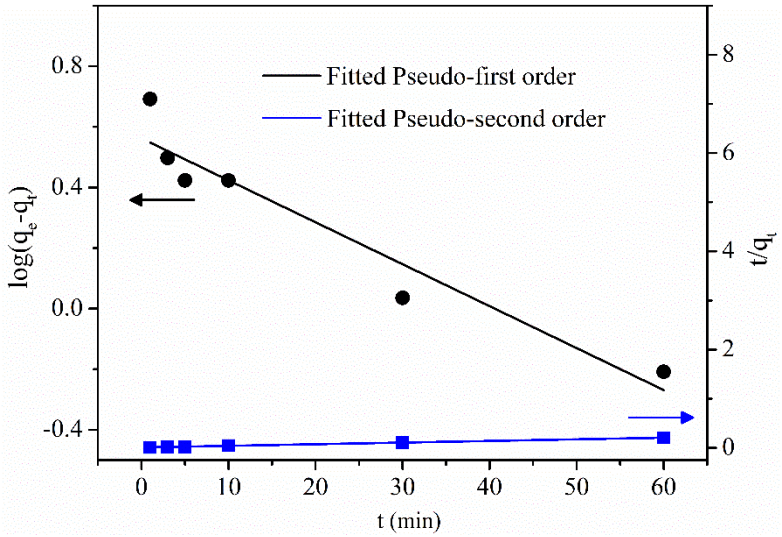

Figure 5.8. Kinetic models for As(III) adsorption at 293 K for calculated SPION in composite.

Table 5.4. Kinetic parameters for As(III) adsorption by SPION, sponge-loaded SPION and SPION in composite.

Adsorbent	Pseudo-first order		Pseudo-second order	
	K_1 (min^{-1})	R^2	K_2 ($g \cdot mg^{-1} \cdot min^{-1}$)	R^2
sponge	0.0414	0.8059	0.0745	0.9999
Sponge-loaded SPION	0.0319	0.9048	0.0555	0.9975
SPION in composite	0.0319	0.9048	0.0014	0.9975

5.4. Thermodynamics analysis

Thermodynamic parameters such as Gibbs free energy change (ΔG^o), enthalpy change (ΔH^o) and entropy change (ΔS^o) can predict the feasibility and nature of the adsorption process [12,13]. The relations of these thermodynamic parameters are displayed in Annex III. By constructing a plot of ln K versus 1/T (Figure 5.9.), $\Delta S°$ can be calculated from the intercept and $\Delta H°$ can be obtained from the slope. The calculated thermodynamic parameters of the adsorbents are displayed in Table 5.5.

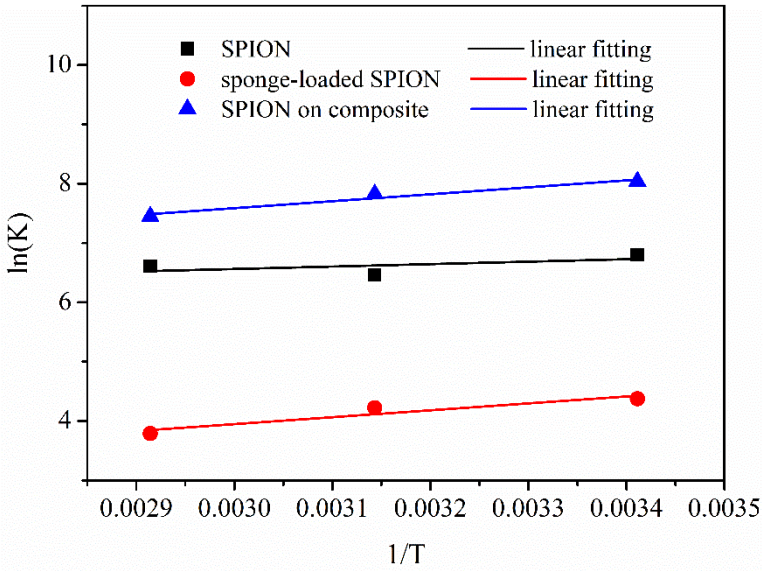

Figure 5.9. Results from fitting analysis for determining $\Delta S°$ and $\Delta H°$.

Table 5.5. Thermodynamic parameters for As(III) adsorption onto the SPION, sponge-loaded SPION, SPION in composite.

Adsorbent	Temperature (K)	ΔG^o (kJ·mol^{-1})	ΔH^o (kJ·mol^{-1})	ΔS^o (J·mol^{-1})
SPION	293	-16.43	10.50	91.88
	318	-18.73		
	343	-21.03		
Sponge-loaded SPION	293	-10.68	4.68	52.39
	318	-11.99		
	343	-13.30		
SPION in composite	293	-19.60	4.68	82.82
	318	-21.67		
	343	-23.74		

The adsorption of As(III) on composite adsorbent (2.6 wt.% SPION on sponge) has negative ΔG^o, positive $\Delta H°$ and positive $\Delta S°$ as SPION. This result is consistent with the behavior of that sponge do not adsorb As(III). The negative ΔG^o values indicate that the adsorption of As(III) onto is spontaneous. Values of $\Delta H°$ are 10.50, 4.68 and 4.68 kJ·mol^{-1} for SPION, sponge-loaded SPION and SPION in composite respectively, which means the As(III) adsorption on these three adsorbents are endothermic processes. The positive $\Delta S°$ likely resulted from the release of orderly structured hydration water and subsequent increase in randomness with increased concentration of adsorbed As(III) on the solid surface [15,16].

5.5. Compare of the adsorption capacity with similar adsorbent system

According to the Fe content in adsorbents, it could be calculated that the equilibrium adsorption capacities of SPION and sponge-loaded SPION with 1000 mg·L^{-1} As(III) initial concentration were 64.7 and 935.0 mg·g^{-1} Fe, respectively. This indicates that SPION loaded on the sponge can significantly

improve the adsorption capacity. This may be due to the fact that cube sponge as the support can effectively prevent SPION from aggregating in the composite, and then increase the effective surface in the adsorption process, resulting in the high adsorption capacity.

Table 5.6. As(III) adsorption capacities comparison of SPION in composite with similar system.

Support material	Size	Iron (wt. %)	Iron phase	q_e ($mg \cdot g^{-1}$ Fe)	Reference
None	12.0 nm	100	γ-Fe_2O_3	64.7 *	This work
Cube sponge	13 x 10 x 7 mm	1.80	γ-Fe_2O_3	935.0 *	This work
None	34 nm	100	Fe_3O_4	23.0	[17]
Cork	0.8~2 mm	2.4	iron (oxy)hydroxides	204.2	[18]
Cellulose	0.01~0.02 mm	36	Fe_2O_3	64.3	[19]
Alginate beads	0.5 mm	30	2-line ferrihydrite	159.3	[20]
Polyurethane foam	6.07 nm	19.33	Fe_3O_4	178.7	[21]

(*) at 800 $mg \cdot L^{-1}$

As shown in Table 5.6, adsorption capacities of both unsupported SPION and SPION as part of the composite are significantly higher when compared with similar Fe-based adsorbent system. For example, Liu et al. reported a maximum As(III) adsorption capacity of 23.0 $mg \cdot g^{-1}$ Fe of magnetite nanoparticles with 34 nm average size [17]; Pintor and coworkers reported a maximum adsorption capacity of 204.2 $mg \cdot g^{-1}$ Fe when loading iron (oxy)hydroxides (2.4 wt.% of Fe) on cork (particle size < 2 mm) [18].

5.6. As K-edge XAS measurements

Due to the different toxic risks associated with the As species [22], it is important to understand the fate of adsorbed As(III) and to discern any possible redox processes that may take place upon adsorption. Indeed, the oxidation state and speciation of As determine its toxicity and mobility in the

environment [23]. In that respect, X-ray absorption near-edge structure (XANES) experiments were performed to investigate the coordination environment and the chemical state of As(III) adsorbed on SPION, sponge and sponge-loaded SPION. The influence of the different temperatures and the different depths of cube adsorbents (C, Q, S) were also studied.

Figure 5.10a shows the comparison of the As K-edge XANES spectra of the adsorbent materials with As reference compounds for As(III), arsenic trioxide, and As(V), arsenic pentoxide. The As reference compounds display a markedly different spectral profile. The pentoxide is shifted ~3.7 eV towards high energy with respect to the trioxide. In addition, the white-line feature (first resonance after the absorption rising edge) appears at 11875.5 and 11871.7 eV for pentoxide and trioxide, respectively. By direct comparison of the position of the absorption edge and the white-line, we found that some of the As(III) were oxidized to As(V) upon adsorption. The oxidation process has been previously reported on iron-based adsorbents [24,25]. Ying and co-authors [24] reported the adsorption–oxidation of As(III) when adsorbed on Cr(VI)-incorporated schwertmannite. As(III) was adsorbed onto the Fe^{3+} adsorption sites and it was further oxidized by the Cr(VI) present on the surface. Zhong et al [25] reported the oxidation of As(III) by hydroxyl free radical (•OH) and hydrogen peroxide (H_2O_2) produced from the activation of molecular oxygen (O_2) at acid and neutral conditions when using a biochar adsorbent for As(III) removal. For our composite adsorbent, a combination of both processes may occur. Under neutral conditions, As(III) is firstly adsorbed on the surface of the adsorbents, and then oxidized by the generated reactive oxygen species (ROS), especially by •OH via the activation of H_2O_2 and O_2 by the Fe(III) and the hydroxyl groups (-OH) present in SPION and sponge adsorbents. The proposed mechanism of adsorption-oxidation is shown in Figure 5.11.

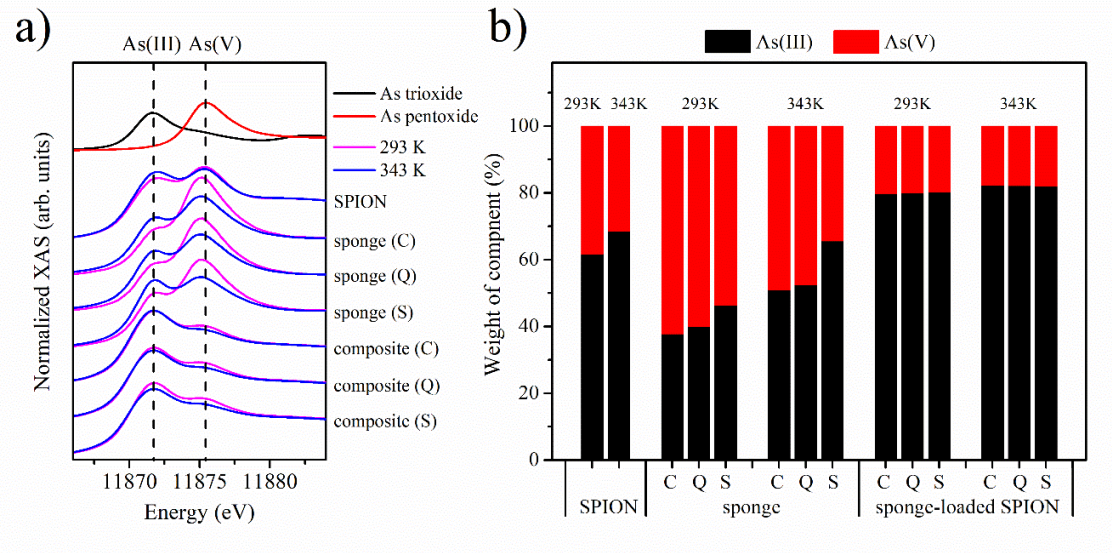

Figure 5.10. As K-edge XAS spectra of adsorbents after adsorbing As(III) at different temperatures (a) and corresponding peak fitting results (b). Arsenic trioxide and pentoxide compounds are also included for comparison and used for peak fitting references.

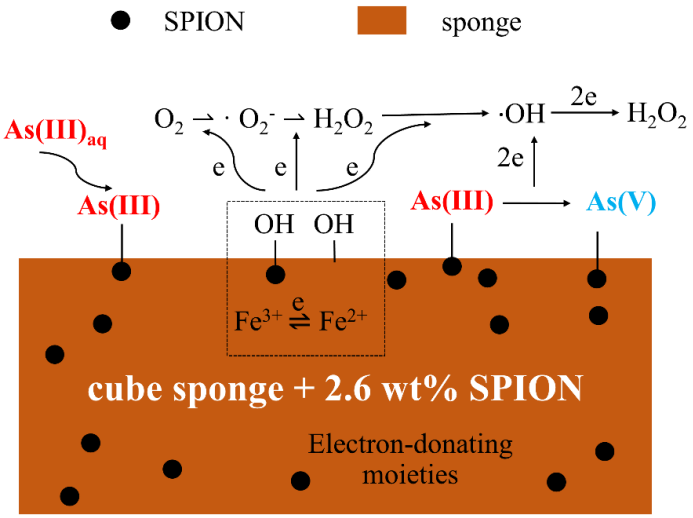

Figure 5.11. Proposed mechanism of As(III) adsorption-oxidation on the surface of adsorbents.

To unraveling the two As species, a peak fitting analysis of the XANES spectra was performed using the spectra of reference compounds. The fitted spectra of SPION, sponge (surface), sponge-loaded SPION (surface) for the As(III)

adsorption at 293 K are shown in Figure 5.12. The final fitted results of all samples are shown in Table 5.7 and Figure 5.10b.

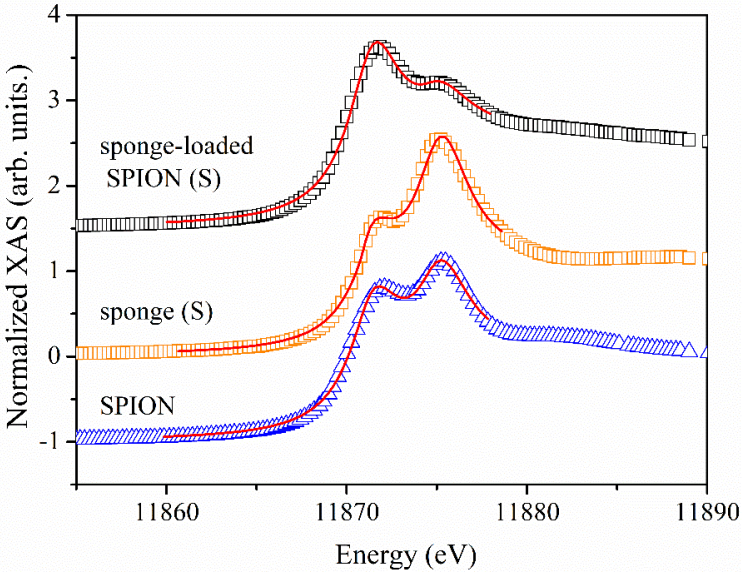

Figure 5.12. Peak fitting results for SPION, sponge (surface), sponge-loaded SPION (surface) for the As(III) adsorption at 293K. (symbols are experimental data and lines are fits.)

When comparing the different adsorbents it was found that the largest amount of As(III) oxidized to As(V) was taking place in sponge, 30-60%. This can be due to the large density of functional sites that can oxidize As(III) respect to low amount of As(III) adsorbed on the sponge. On the other hand, SPION showed a larger amount of As(V) than sponge-loaded SPION. This can be related with the low loading of the γ-Fe_2O_3 nanoparticles in the composite material (2.6 wt.%). In other words, the As:Fe ratio in the composite is much larger than in the unsupported SPION, which turns into less available Fe(III) species to contribute to the As(III) oxidation process after adsorption. In all the materials, the oxidization of As(III) to As(V) was more favorable at the lower temperature due to the decomposition of H_2O_2 at higher temperatures which resulted in the decrease of •OH [26]. However, the difference in sponge-loaded SPION caused by temperature was very small (only ~2%) because of the small

mass loading of SPION in the composite as mentioned above. After adsorption, the amount of -OH functional site available in the loaded SPION are much lower than in the case of unsupported SPION. When comparing different depths of the cube material, As(III) adsorbed in center part of the sponge showed a higher amount of As(V) species due to the diffusion constrains that increase towards the center of the cube, hence, reducing the recirculation of hydroxyl free radicals and favoring the interaction. However, the As(III) oxidation reaction in sponge-loaded SPION was controlled by the mass of SPION, which is rather constant in the whole cube and yields similar As(V) conversion in all parts of the cube.

Table 5.7. Peak fitting results of SPION, sponge and sponge-loaded SPION. (C, center; Q, quarter; S, surface). Fixed parameters for As(III) fittings: arctangent e_0 = 11871.0 eV, Lorentzian center = 11871.40 eV. Fixed parameters for As(V) fittings: arctangent e_0 = 11874.56 eV, Lorentzian center = 11875.22 eV.

Adsorbent	Temperature (K)	As(III)				As(V)				R-factor	**Final results**	
		step	height	width (eV)	sigma (eV)	step	height	width (eV)	sigma (eV)		**As(III) (%)**	**As(V) (%)**
SPION	293	0.670	6.274	0.744	3.628	0.415	5.823	0.806	3.726	0.0005	**61.75**	**38.25**
SPION	343	0.758	7.030	0.669	3.608	0.347	5.148	0.744	3.785	0.0006	**68.60**	**31.40**
sponge (C)		0.423	3.103	0.307	3.588	0.696	10.660	1.189	3.605	0.0008	**37.80**	**62.20**
sponge (Q)	293	0.442	3.434	0.345	3.551	0.664	10.040	1.33	3.657	0.0008	**39.96**	**60.04**
sponge (S)		0.521	4.324	0.314	3.466	0.603	8.835	0.959	3.705	0.0005	**46.35**	**53.65**
sponge (C)		0.565	5.318	0.544	3.749	0.543	7.646	1.303	3.921	0.0006	**50.99**	**49.01**
sponge (Q)	343	0.591	5.413	0.64	3.491	0.534	7.365	1.624	3.937	0.0005	**52.53**	**47.47**
sponge (S)		0.729	6.407	0.411	3.535	0.381	5.726	0.814	4.073	0.0003	**65.68**	**34.32**
composite (C)		0.891	8.351	1.002	3.623	0.224	3.146	0.602	4.273	0.0007	**79.91**	**20.09**
composite (Q)	293	0.885	8.445	1.072	3.665	0.222	3.061	0.59	4.285	0.0007	**79.95**	**20.05**
composite (S)		0.895	8.346	0.986	3.636	0.220	3.108	0.609	4.351	0.0006	**80.27**	**19.73**
composite (C)		0.913	8.756	1.072	3.714	0.196	2.454	0.587	4.429	0.0008	**82.33**	**17.67**
composite (Q)	343	0.900	8.592	1.235	3.831	0.194	2.324	0.517	4.559	0.0009	**82.27**	**17.73**
composite (S)		0.895	8.356	1.293	3.901	0.196	2.310	0.521	4.585	0.0009	**82.03**	**17.97**

5.7. Conclusions

In this work, we have shown that our cube-shaped open-celled cellulose sponge loaded with superparamagnetic iron oxide nanoparticles (SPION) synthesized via an in-situ co-precipitation method is an efficient adsorbent material for As(III) removal. The adsorption of As(III) on this composite adsorbent was best described by the Temkin isotherm model and the pseudo-second order kinetic model which indicates that chemisorption is controlling the speed of the adsorption process. The assessment of the thermodynamic parameters $\Delta H°$ and $\Delta G°$ indicated that the As(III) adsorption on the composite adsorbent kept the same properties (spontaneous and endothermic) as the unsupported SPION, but with the advantage of having greatly reduced the nanoparticle aggregation.

In addition, we have observed that the highly toxic and carcinogenic As(III) was oxidized to less toxic As(V), which is desirable for the treatment of As(III)-contaminated waters. Our XAS study supports that, after adsorption, As(III) was oxidized to As(V) by both the •OH radicals generated from Fe(III) and the -OH groups present in SPION and sponge adsorbents under neutral conditions.. Besides, similar oxidation level of the adsorbed As(III) was found at different cube depths which demonstrates that the same adsorption process takes place at the different parts of the cube due to the good diffusion properties of the sponge material and the rather homogeneity of the SPION loaded in the porous sponge.

5.8. Reference

[1] A. Shahat, H.M.A. Hassan, H.M.E. Azzazy, M. Hosni, M.R. Awual, Novel nano-conjugate materials for effective arsenic(V) and phosphate capturing in aqueous media, Chem. Eng. J. 331 (2018) 54–63. https://doi.org/10.1016/j.cej.2017.08.037.

[2] M. Navarrete-Magaña, A. Estrella-González, L. May-Ix, S. Cipagauta-Díaz, R. Gómez, Improved photocatalytic oxidation of arsenic (III) with WO3/TiO2 nanomaterials synthesized by the sol-gel method, J. Environ. Manage. 282 (2021) 111602. https://doi.org/10.1016/j.jenvman.2020.111602.

[3] H.N. Tran, S.J. You, A. Hosseini-Bandegharaei, H.P. Chao, Mistakes and inconsistencies regarding adsorption of contaminants from aqueous solutions: A critical review, Water Res. 120 (2017) 88–116. https://doi.org/10.1016/j.watres.2017.04.014.

[4] K.Y. Foo, B.H. Hameed, Insights into the modeling of adsorption isotherm systems, Chem. Eng. J. 156 (2010) 2–10. https://doi.org/10.1016/j.cej.2009.09.013.

[5] Y. Liu, Y. Xiong, P. Xu, Y. Pang, C. Du, Enhancement of Pb (II) adsorption by boron doped ordered mesoporous carbon: Isotherm and kinetics modeling, Sci. Total Environ. 708 (2020) 134918. https://doi.org/10.1016/j.scitotenv.2019.134918.

[6] S. Nethaji, A. Sivasamy, A.B. Mandal, Adsorption isotherms, kinetics and mechanism for the adsorption of cationic and anionic dyes onto carbonaceous particles prepared from Juglans regia shell biomass, Int. J. Environ. Sci. Technol. 10 (2013) 231–242. https://doi.org/10.1007/s13762-012-0112-0.

[7] L. Simonelli, C. Marini, W. Olszewski, M. Ávila Pérez, N. Ramanan, G. Guilera, V. Cuartero, K. Klementiev, CLÆSS: The hard X-ray absorption beamline of the ALBA CELLS synchrotron, Cogent Phys. 3 (2016) 1231987. https://doi.org/10.1080/23311940.2016.1231987.

[8] B. Ravel, M. Newville, ATHENA, ARTEMIS, HEPHAESTUS: Data analysis for X-ray absorption spectroscopy using IFEFFIT, J. Synchrotron Radiat. 12 (2005) 537–541. https://doi.org/10.1107/S0909049505012719.

[9] Y. Xiong, Q. Tong, W. Shan, Z. Xing, Y. Wang, S. Wen, Z. Lou, Arsenic transformation and adsorption by iron hydroxide/manganese dioxide doped straw activated carbon, Appl. Surf. Sci. 416 (2017) 618–627. https://doi.org/10.1016/j.apsusc.2017.04.145.

[10] J.O. De Marques Neto, C.R. Bellato, J.L. Milagres, K.D. Pessoa, E.S. De Alvarenga, Preparation and evaluation of chitosan beads immobilized with iron(III) for the removal of As(III) and As(V) from water, J. Braz. Chem. Soc. 24 (2013) 121–132. https://doi.org/10.1590/S0103-50532013000100017.

[11] Y. Tong, P.J. McNamara, B.K. Mayer, Adsorption of organic micropollutants onto biochar: A review of relevant kinetics, mechanisms and equilibrium, Environ. Sci. Water Res. Technol. 5 (2019) 821–838. https://doi.org/10.1039/c8ew00938d.

[12] B. Adane, K. Siraj, N. Meka, Kinetic, equilibrium and thermodynamic study of 2-chlorophenol adsorption onto Ricinus communis pericarp activated carbon from aqueous solutions, Green Chem. Lett. Rev. 8 (2015) 1–12. https://doi.org/10.1080/17518253.2015.1065348.

[13] E.C. Lima, A. Hosseini-Bandegharaei, J.C. Moreno-Piraján, I. Anastopoulos, A critical review of the estimation of the thermodynamic parameters on adsorption equilibria. Wrong use of equilibrium constant in the Van't Hoof equation for calculation of thermodynamic parameters of adsorption, J. Mol. Liq. 273 (2019) 425–434. https://doi.org/10.1016/j.molliq.2018.10.048.

[14] T. Chen, T. Da, Y. Ma, Reasonable calculation of the thermodynamic parameters from adsorption equilibrium constant, J. Mol. Liq. 322 (2021) 114980. https://doi.org/10.1016/j.molliq.2020.114980.

[15] J. Giménez, M. Martínez, J. de Pablo, M. Rovira, L. Duro, Arsenic sorption onto natural hematite, magnetite, and goethite, J. Hazard. Mater. 141 (2007) 575–580. https://doi.org/10.1016/j.jhazmat.2006.07.020.

[16] Z. Veličković, G.D. Vuković, A.D. Marinković, M.S. Moldovan, A.A. Perić-Grujić, P.S. Uskoković, M.D. Ristić, Adsorption of arsenate on iron(III) oxide coated ethylenediamine functionalized multiwall carbon nanotubes, Chem. Eng. J. 181–182 (2012) 174–181. https://doi.org/10.1016/j.cej.2011.11.052.

[17] C.H. Liu, Y.H. Chuang, T.Y. Chen, Y. Tian, H. Li, M.K. Wang, W. Zhang, Mechanism of Arsenic Adsorption on Magnetite Nanoparticles from Water: Thermodynamic and Spectroscopic Studies, Environ. Sci. Technol. 49 (2015) 7726–7734. https://doi.org/10.1021/acs.est.5b00381.

[18] A.M.A. Pintor, B.R.C. Vieira, S.C.R. Santos, R.A.R. Boaventura, C.M.S. Botelho, Arsenate

and arsenite adsorption onto iron-coated cork granulates, Sci. Total Environ. 642 (2018) 1075–1089. https://doi.org/10.1016/j.scitotenv.2018.06.170.

[19] X. Yu, S. Tong, M. Ge, J. Zuo, C. Cao, W. Song, One-step synthesis of magnetic composites of cellulose@iron oxide nanoparticles for arsenic removal, J. Mater. Chem. A. 1 (2013) 959–965. https://doi.org/10.1039/c2ta00315e.

[20] A. Sigdel, J. Park, H. Kwak, P.K. Park, Arsenic removal from aqueous solutions by adsorption onto hydrous iron oxide-impregnated alginate beads, J. Ind. Eng. Chem. 35 (2016) 277–286. https://doi.org/10.1016/j.jiec.2016.01.005.

[21] X. Song, Y. Wang, L. Zhou, X. Luo, J. Liu, Halloysite nanotubes stabilized polyurethane foam carbon coupled with iron oxide for high-efficient and fast treatment of arsenic(III/V) wastewater, Chem. Eng. Res. Des. 165 (2021) 298–307. https://doi.org/10.1016/j.cherd.2020.11.001.

[22] R. Amen, H. Bashir, I. Bibi, S.M. Shaheen, N.K. Niazi, M. Shahid, M.M. Hussain, V. Antoniadis, M.B. Shakoor, S.G. Al-Solaimani, H. Wang, J. Bundschuh, J. Rinklebe, A critical review on arsenic removal from water using biochar-based adsorbents: The significance of modification and redox reactions, Chem. Eng. J. 396 (2020) 125195. https://doi.org/10.1016/j.cej.2020.125195.

[23] Y. Wu, R.K. Kukkadapu, K.J.T. Livi, W. Xu, W. Li, D.L. Sparks, Iron and Arsenic Speciation during As(III) Oxidation by Manganese Oxides in the Presence of Fe(II): Molecular-Level Characterization Using XAFS, Mössbauer, and TEM Analysis, ACS Earth Sp. Chem. 2 (2018) 256–268. https://doi.org/10.1021/acsearthspacechem.7b00119.

[24] H. Ying, K. Huang, X. Feng, Y. Yan, M. Zhu, Z. Wang, Q. Huang, X. Wang, As(iii) adsorption–oxidation behavior and mechanisms on Cr(vi)-incorporated schwertmannite , Environ. Sci. Nano. (2021). https://doi.org/10.1039/d1en00104c.

[25] D. Zhong, Y. Jiang, Z. Zhao, L. Wang, J. Chen, S. Ren, Z. Liu, Y. Zhang, D.C.W. Tsang, J.C. Crittenden, PH Dependence of Arsenic Oxidation by Rice-Husk-Derived Biochar: Roles of Redox-Active Moieties, Environ. Sci. Technol. 53 (2019) 9034–9044. https://doi.org/10.1021/acs.est.9b00756.

[26] P. Pędziwiatr, F. Mikołajczyk, D. Zawadzki, K. Mikołajczyk, A. Bedka, Decomposition of hydrogen peroxide - kinetics and review of chosen catalysts, Acta Innov. (2018) 45–52. https://doi.org/10.32933/actainnovations.26.5.

Chapter 6: Arsenic fixed-bed column adsorption study

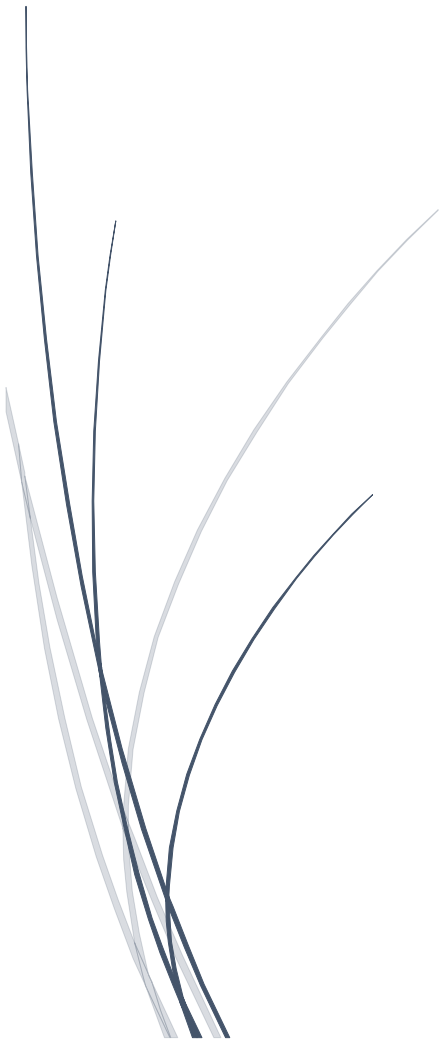

In previous chapters, batch adsorption experiments were performed to assess the adsorption performance of sponge and sponge-loaded SPION for As removal at different pH values, initial concentrations, and contact times. To explore the possibility of using these adsorbents for industrial applications, we have carried out fixed-bed column adsorption experiments.

6.1. Fixed-bed adsorption system

Among the existing adsorption systems such as batch, continuous fixed-bed, continuous moving bed, continuous fluidized bed and pulsed bed systems [1,2], batch and fixed-bed column adsorption systems are the most commonly used [3]. The batch adsorption system has the advantages of easy operation and being cost-effective, and it is usually used in exploratory research studies at laboratory scale and it is scarcely used for industrial applications [4–6]. The fixed-bed adsorption system consists of a fixed mass of adsorbent packed in the column through where the adsorbate continuously flows at constant rate [7,8]. Compared to the batch system, the fixed-bed column system is capable to treat much larger volume and it can be easily scaled up from laboratory-scale to industrial application [9,10].

For designing and optimizing the adsorption processes in fixed-bed systems, breakthrough curves are measured. In breakthrough experiments, the concentration at the outlet of the column is monitored and the outlet-to-inlet concentration ratio (C/C_o) is then represented against time (t) or throughput volume [11,12]. In most of the cases, the breakthrough curves exhibit a characteristic 'S' shape with varying degrees of steepness in the transient [13,14]. An ideal breakthrough curve is represented in Figure 6.1. Two characteristic points in a breakthrough curve are used to define the performance of the adsorbent material. These are the breakthrough point and exhaustion point, that, for convenience, are defined as the points at 5% and 90%

of the total C/C_o, respectively [15,16]. The amount of adsorbate in the outlet water can be calculated from the area under the breakthrough curve, thus the adsorbed amount of adsorbate until breakthrough point or exhaustion point can be calculated by subtracting that amount from the total adsorbate used in the process. In that respect, several parameters have been defined to evaluate the column's performance when doing breakthrough experiments with a fixed-bed system [17]:

1) The number of bed volume (BV) to reach the breakthrough point and exhaustion point.
2) The amount of adsorbate (q in mg) adsorbed on the adsorbents and its corresponding bed adsorption capacities (q_e in $mg \cdot g^{-1}$) until the breakpoint and the exhaustion point.
3) The time at which it is necessary to regenerated the adsorbent.

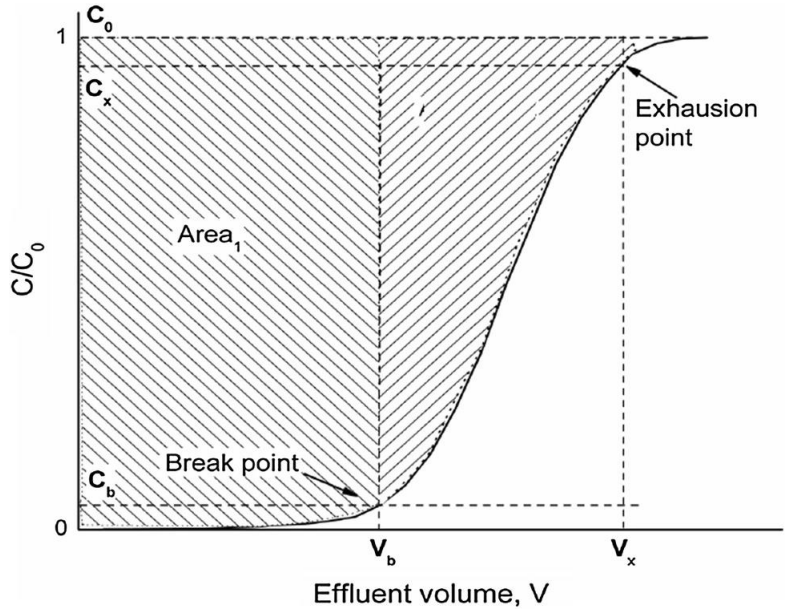

Figure 6.1. Ideal breakthrough curve reproduced from Ref. [6].

6.2. Arsenic adsorption by using laboratory fixed-bed column

The continuous fixed-bed adsorption experiments were firstly performed by

using a laboratory column set-up, see Figure 6.2. To control the temperature during the adsorption process, jacketed glass columns connected to a water bath were used. The diameter and length of the column are 1 and 20 cm, respectively

The effects of various process parameters like initial concentration, flow rate, and adsorption temperature were investigated and breakthrough points were measured. For adsorption, 1g of powder sponge (0.5~2 mm) is placed into the column (bed volume 3.5 ml). As(V) solutions with different initial concentrations (10, 50, 200 $mg \cdot L^{-1}$) were passed through the column using a peristaltic pump with different flow rates (1.0, 2.5, 4.0 $ml \cdot min^{-1}$) at 293 or 343 K. The elution samples (1 BV) were collected every 10 BV using 10 ml falcon tubes and analyzed by UV-vis.

Figure 6.2. Experimental set-up of a the fixed-bed column with water bath used for arsenic adsorption.

6.2.1. Effect of different initial concentrations

The initial concentration is an important factor that provides the appropriate driving force for the transport of adsorbate molecules through the adsorbent

bed in fixed-bed adsorption process [18,19]. The fixed-bed column adsorption experiments of different initial concentrations were performed at 293 K with a flow rate of 2.5 ml·min^{-1}. The breakthrough curves are shown in Figure 6.3, and the information extracted is reported in Table 6.1.

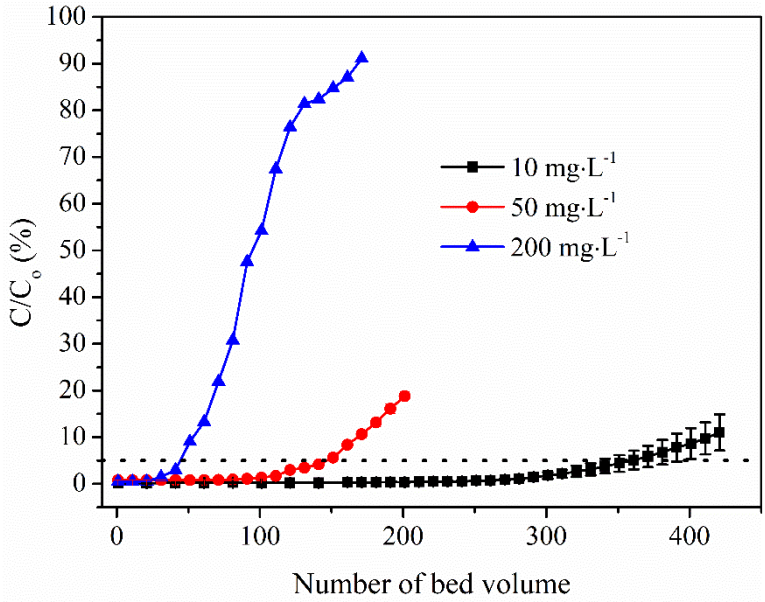

Figure 6.3. Breakthrough curve of laboratory column with different initial concentrations.

Table 6.1. Breakthrough point results with different initial concentrations.

Initial concentration (mg·L^{-1})	Time (h)	Number of BV	Volume (ml)	Adsorption capacity (mg·g^{-1})	Removal rate (%)
10	8.37	358.89	1256.12	12.45	99.1
50	3.43	146.84	513.94	25.31	98.5
200	1.03	44.10	154.35	30.48	98.7

The breakthrough points of 10, 50, 200 mg·L^{-1} initial concentrations occurred for 358.89, 146.84 and 44.10 bed volumes, respectively. This indicates that at high initial concentrations, the breakthrough point is reached earlier (see breakthrough times in Table 6.1). This behavior is related to the enhancement

of concentration gradient for mass transfer across the liquid film along with the acceleration of adsorption rate, which leads to an early saturation of the fixed bed [20].

The amount of adsorbate adsorbed by adsorbents was calculated from integrating the area over the breakthrough curve until the breakthrough point as explained above. The corresponding adsorption capacity was calculated by dividing the amount of adsorbent by the weight of adsorbent. We found that the adsorption capacity increased with the initial concentration as 12.45, 25.31 and 30.48 $mg \cdot g^{-1}$ for 10, 50, 200 $mg \cdot L^{-1}$, respectively. This is associated with the fact that the active sites of adsorbent were surrounded by a larger amount of As(V) ions at higher concentrations; hence the equilibrium adsorption capacity increases with increasing the As(V) ion concentration which enhances the adsorption process [21,22]. This result is consistent with those obtained from the batch experiments. In addition, all the adsorption processes for different initial concentrations maintained high As(V) removal rates (See Table 6.1).

6.2.2. Effect of different flow rates

Flow rate is another important factor affecting the efficiency of the fixed-bed column adsorption [22]. This parameter influences the contact time between the adsorbate and the adsorbent in the column [23]. In our case, different flow rates (1.0, 2.5, 4.0 $ml \cdot min^{-1}$) with 200 $mg \cdot L^{-1}$ initial concentration at 293 K were performed. The breakthrough curves are shown in Figure 6.4 and corresponding calculated results are listed in Table 6.2.

For different flow rates, the breakthrough points occur at very similar number of bed volumes. It is slightly faster to reach the breakthrough point when using higher flow rates (8%). This indicates that increasing the flow rate from 1 to 4 $ml \cdot min^{-1}$ has a small effect on the adsorption of As(V) ions. This is related with the fast adsorption kinetics of As(V) ions in the sponge. This result is consistent

with the results from the kinetic study results in batch experiments. Furthermore, the calculated adsorption capacities were around 30 mg·g^{-1} for all three flow rates and As(V) removal rates maintained above 95% during all the adsorption processes.

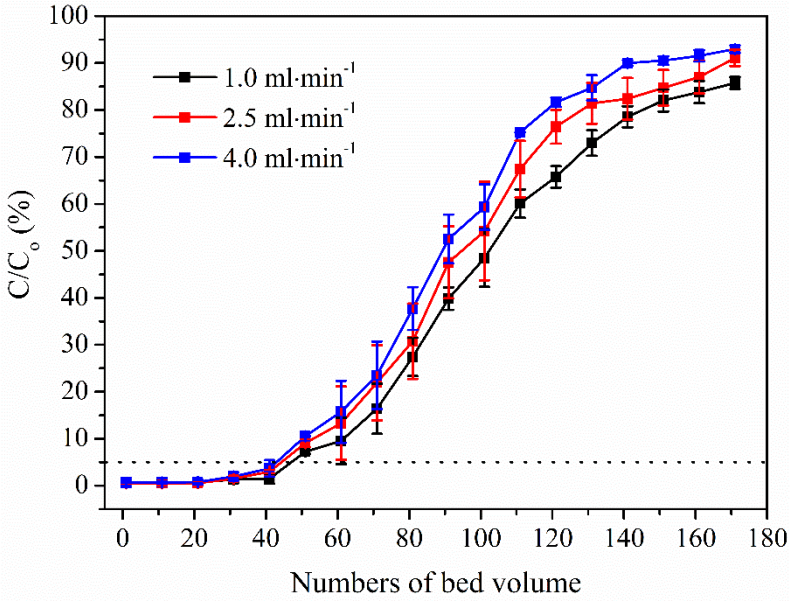

Figure 6.4. Breakthrough curves of laboratory column with different flow rates.

Table 6.2. Breakthrough point results with different flow rates.

Flow rate (ml·min^{-1})	Time (h)	Number of BV	Volume (ml)	Adsorption capacity (mg·g^{-1})	Removal rate (%)
1.0	2.73	46.85	163.98	32.26	98.4
2.5	1.03	44.10	154.35	30.48	98.7
4.0	0.63	42.94	150.29	28.84	95.9

6.2.3. Effect of different temperatures

Temperature is another parameter that affects the adsorption performance of fixed-bed column adsorption [25,26]. The effect of different temperatures (293, 343 K) with 200 mg·L^{-1} initial concentration was investigated. Since the flow rate does not affect much of the breakthrough curve, we have chosen an

intermediate flow rate (2.5 ml·min^{-1}) in this experiment. The results from the breakthrough experiments are shown in Figure 6.5. and Table 6.3.

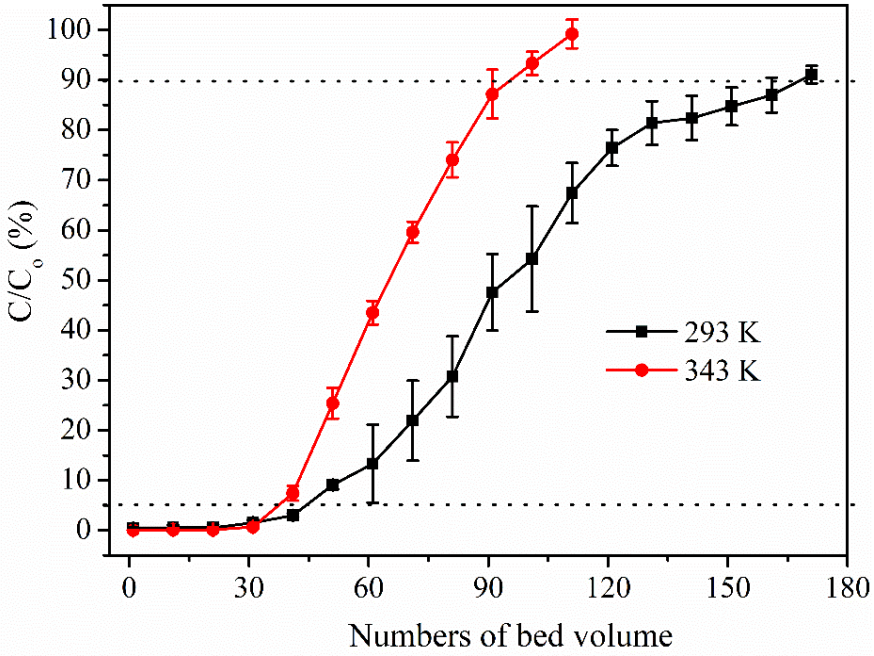

Figure 6.5. Breakthrough curves of laboratory column with different temperatures.

Table 6.3. Breakthrough point results at different temperatures.

Temperatures (K)	Time (h)	Number of BV	Volume (ml)	Adsorption capacity (mg·g^{-1})	Removal rate (%)
293	1.03	44.10	154.35	30.48	98.7
343	0.88	37.56	131.46	26.12	99.3

The breakthrough points at different temperatures were 44.10 BV for 293 K and 37.56 BV for 343 K, respectively. This indicated that the breakthrough curve reached the breakthrough point at higher temperatures. This can be attributed to the effect of the faster diffusion of As ions through the sponge bed at higher operating temperature [27]. Besides, according to the results of batch experiments and the thermodynamic analysis, the adsorption of As(V) on sponge is an exothermic process and its adsorption capacity decreases as the

temperature increases. Thus, the adsorption of As(V) onto sponge is favored at lower temperatures. As expected for the fixed-bed, the adsorption capacities at breakthrough point decreased from 30.48 to 26.12 when increasing the temperature from at 293 to 343 K. Hence, this temperature increase did not have a significant effect on the breakthrough point, although the breakthrough curve for 343 K has a much steeper rise than the one at lower temperature which influences the value of the exhaustion point.

6.2.4. Continue adsorption-thermo desorption experiments

In most of the reported studies, the regeneration of adsorbents is accomplished by adjusting the pH value benefiting by great variation of the adsorption capacity at different pH [28,29]. However, this method consumes a significant amount of chemical reagent, which has been proved to be expensive and not environmentally-friendly [29,30]. It is very necessary to develop new approaches for adsorbent regeneration with the new requirement of green chemistry. In the previous section (see 6.1.3), we find there is a difference (4.36 $mg \cdot g^{-1}$) in adsorption capacities when adsorption experiments performed at different temperatures. Thus, thermal desorption was used to perform continuous alternative adsorption-desorption experiments.

Adsorptions were performed at 293 K with 10 $mg \cdot L^{-1}$ initial concentration. To decrease the operate time, 4 $ml \cdot min^{-1}$ flow rate was used in this experiment. To monitor the concentration of As during the process, fractions of the eluted solution were collected every 20 BV at the beginning of the first adsorption cycle, and every 10 BV after that, this is during the second half of the first cycle and the rest of the cycles, and then analyzed by UV-vis afterwards. When the As concentration of outlet solution reached breakthrough concentration (5% of C_o, 0.5 $mg \cdot L^{-1}$), the adsorption step was stopped and the desorption process started. Desorption experiments were performed by pumping 10 BV of Milli-Q

waters at 343 K with 1 ml·min^{-1} flow rate. Desorption solutions were also analyzed to calculate the amount of desorbed As. Three cycles of adsorption-desorption experiments were performed. The breakthrough curves of three cycles are shown in Figure 6.6, and the information extracted is reported in Table 6.4.

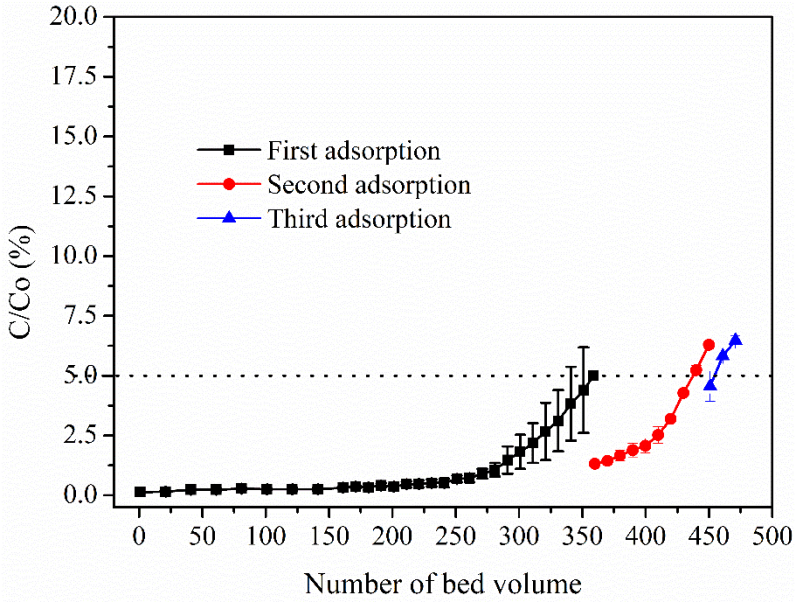

Figure 6.6. Adsorption breakthrough curves of laboratory column in three thermo adsorption-desorption cycles.

Table 6.4. Results of breakthrough point and thermo desorption amount in three cycles.

Cycles	Time (h)	Number of BV	Volume (ml)	Adsorption amount (mg)	Removal rate (%)	Desorption amount (mg·g^{-1})
First	5.23	358.89	1256.12	12.55	99.9	0.016
Second	1.15	78.93	276.26	2.76	99.9	0.018
Third	0.25	16.89	59.12	0.59	99.8	0.035

Results showed that the breakthrough points significantly decreased from 358.89 BV at the first adsorption cycle, to 78.93 BV at the second cycle, and 16.89

BV at the third adsorption cycle. All three cycles maintained high As(V) removal rates (~99.9 %). When comparing to the initial adsorption experiment (first cycle), the breakthrough point of continuous adsorption-desorption increased 26.70%. Thermal desorption amounts of As in three cycles were 0.016, 0.018, 0.035 $mg \cdot g^{-1}$, respectively. This slightly increase was mainly because adsorbed As in the sponge increased as the cyclic experiment progresses. All these results indicate that sponge could be regenerated for at least three cycles by thermal desorption; however, the regeneration is not as effective as the chemical desorption obtained by varying the pH of the solution. This is mainly due to the fact that the variation of the adsorption capacity for different temperatures is not as larger as for different pH values.

6.3. Arsenic adsorption and desorption by pilot plant

To assess the performance under more realistic operation conditions of the adsorbent materials for As removal investigated in this Thesis, the procedure developed for laboratory column was scaled up to perform the breakthrough experiments in our pilot plant. The pilot plant equipment is shown in Figure 6.7. The diameter of the column is 4.5 cm, the length is 77 cm and the flow rate can be varied within 0-180 $ml \cdot min^{-1}$.

Effect of different initial concentrations (10, 50, 200 $mg \cdot L^{-1}$) on the breakthrough response and the adsorption performance of different adsorbents (cube sponge, cube sponge-loaded SPION) were studied. For the adsorption experiments, 20 g of cube adsorbents (~100 cubes) were placed into the pilot plant column. The bed volume is 108 ml and the bed height is 7 cm. A peristaltic pump was used to set the flow rate through the column equal to 17.78 $ml \cdot min^{-1}$. The experiments were performed using the top to bottom method at room temperature. Desorption experiments were performed by flowing 0.5 M NaOH through the column bed. The eluted samples (0.25 BV) were collected every 10 BV using 50

ml falcon tubes and the As(V) concentration was determined by UV-vis colorimetric analysis.

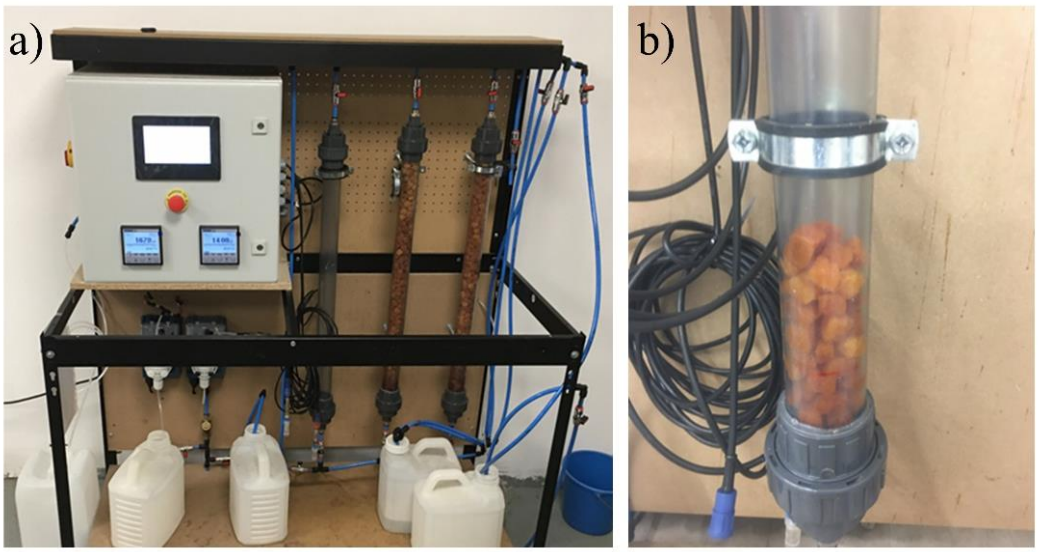

Figure 6.7. Fixed-bed pilot plant equipment for As adsorption.

6.3.1. Effect of different initial concentrations

The results from the breakthrough curves measured at different initial concentrations are shown in Figure 6.8 and Table 6.5. The breakthrough points notably decreased from 70.65 to 6.65 bed volume when increasing the As(V) concentration from 10 to 200 $mg \cdot L^{-1}$. The adsorption capacity had an increase from 3.71 to 6.54 $mg \cdot g^{-1}$ when increasing the initial concentration from 10 to 50 $mg \cdot L^{-1}$, but further increasing of the concentration to 200 $mg \cdot L^{-1}$ induce a little effect, 6.96 $mg \cdot g^{-1}$. The removal rates of As(V) maintained high in all three adsorption processes. All these results agree with the ones obtained for the laboratory column. A more detailed comparison will be shown in the following subsection 6.3.

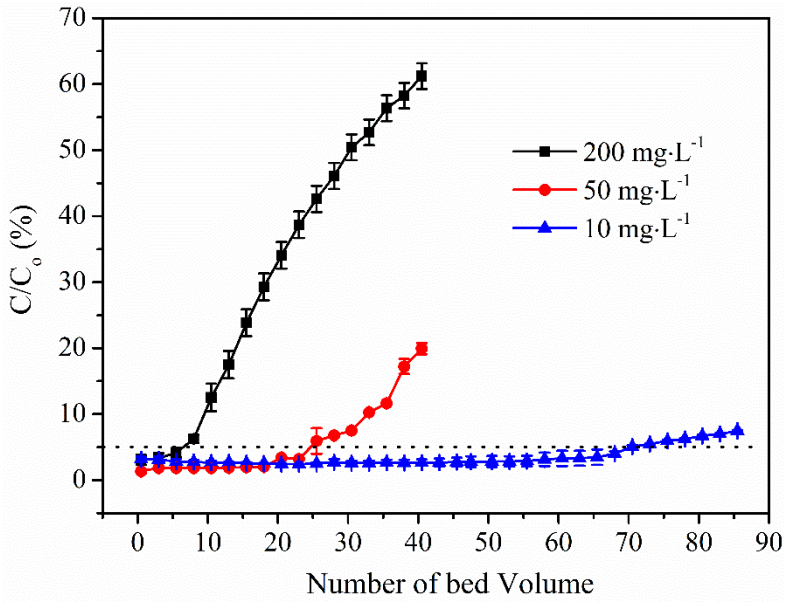

Figure 6.8. Adsorption breakthrough curves of pilot plant with different initial concentrations.

Table 6.5. Breakthrough point of pilot plant with different initial concentrations.

Initial concentration (mg·L^{-1})	Time (h)	Number of BV	Volume (L)	Adsorption capacity (mg·g^{-1})	Removal rate (%)
10	7.15	70.65	7.63	3.71	97.3
50	2.51	24.77	2.68	6.54	97.6
200	0.67	6.65	0.72	6.96	96.7

6.3.2. Compare of the sponge and sponge-loaded SPION

The adsorption performance of the cube sponge and cube sponge-loaded SPION when used as adsorbents in the pilot plant was assessed. For these experiments, the column was filled with ~20 g of adsorbent (~100 cubes) and the breakthrough was carried out setting flow rate of 17.78 ml·min^{-1} of a solution of 50 mg·L^{-1} of As(V). The results are displayed in Figure 6.9 and Table 6.6.

The numbers of bed volume to reach the breakthrough point for sponge and sponge-loaded SPION were 24.77 and 48.44 BV, respectively. The resulting adsorption capacities were 6.65 $mg \cdot g^{-1}$ for sponge and 12.89 $mg \cdot g^{-1}$ for sponge-loaded SPION. Hence, loading 2.6 wt.% SPION on cube sponge resulted in more than 95% enhancement in both the number of bed volume and the adsorption capacity respect to the sponge. The adsorption removal rate for both sponge and sponge-loaded SPION maintained high.

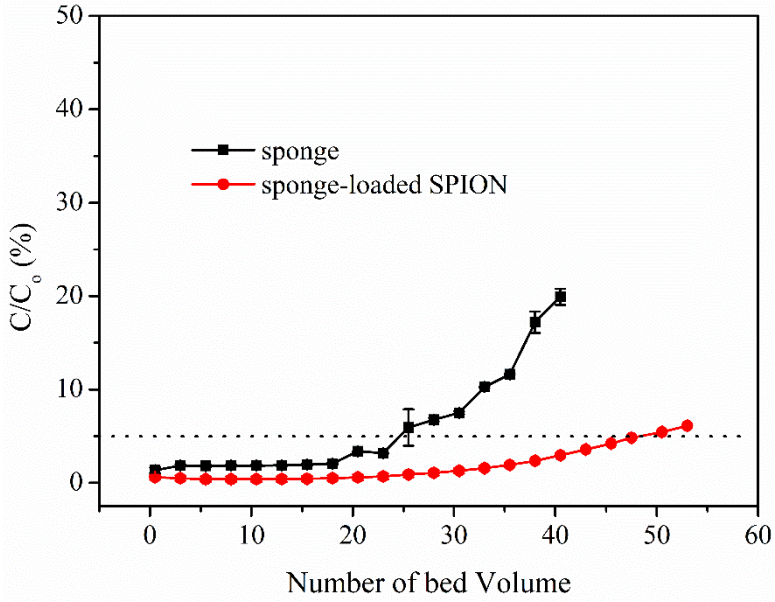

Figure 6.9. Adsorption breakthrough curves of pilot plant with adsorbents.

Table 6.6. Breakthrough point of pilot plant with different initial concentrations.

adsorbents	Time (h)	Number of BV	Volume (L)	Adsorption capacity ($mg \cdot g^{-1}$)	Removal rate (%)
Sponge	2.51	24.77	2.68	6.54	97.6
Sponge-loaded SPION	4.90	48.44	5.23	12.89	98.6

6.4. Compare of column and pilot plant adsorption

The performance of the laboratory column and pilot plant were also compared in the condition of similar residential time. The weight of adsorbent (cube sponge) and volume of As solution used in pilot plant was 20 times that of laboratory column experiment. Detailed parameters of laboratory column and pilot plant are listed in Table 6.7. The initial As concentration used was 1 $mg \cdot L^{-1}$. Due to the dilute concentration of the outlet samples, the detection of As concentration was carried out by ICP-MS analysis.

Table 6.7. Parameters of laboratory column and pilot plant with similar operate condition.

Fix-bed column	Weight of adsorbents (g)	Volume of solution (L)	Residential time (min)	Bed volume (ml)	Flow rate ($ml \cdot min^{-1}$)
Laboratory column	1	1	5.32	3.5	1.0
Pilot plant	20	20	5.47	108	17.78

The breakthrough curve of laboratory column and pilot plant are shown in Figure 6.10. It could be clearly seen that for both laboratory column and pilot plant during all operating process, the concentration of outlet arsenic was always below the breakthrough concentration (50 $mg \cdot ml^{-1}$). After calculation by integrating, the adsorption capacities of laboratory column and pilot plant were 0.975 and 0.964 $mg \cdot g^{-1}$, respectively, which was quite similar.

Desorption experiments were also performed to investigate the regeneration of the adsorbents. For laboratory column, both thermal desorption and chemical desorption were studied. Thermal desorption and chemical desorption were performed by passing 343 K Milli-Q water or 0.5 M NaOH solution, respectively. For each method, six samples of 5 ml were collected consecutively. For pilot plant, only chemical desorption was investigated by using 0.5 M

NaOH solution. Six samples were collected by plastic tubes every 50 ml. Arsenic concentrations of all the desorption samples were analyzed by UV-vis. The desorption results of laboratory column and pilot plant are shown in Figure 6.11 and extract information are calculated and listed in Table 6.8.

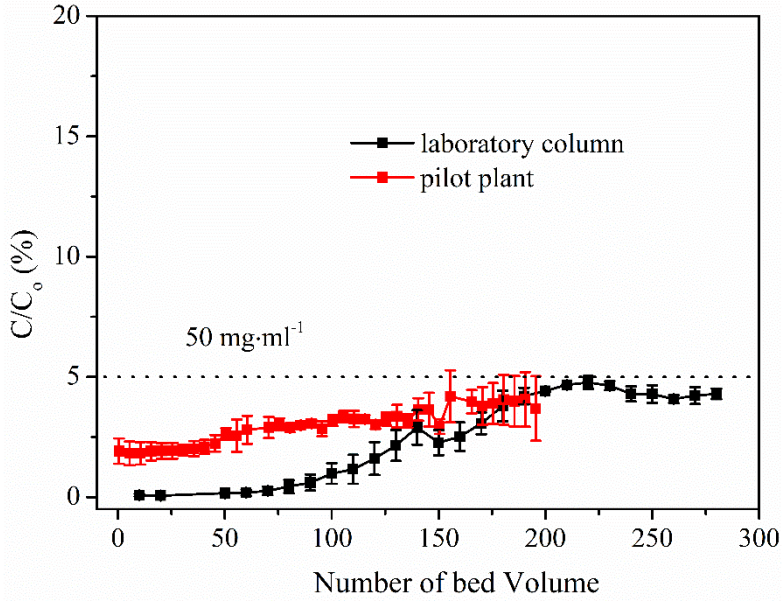

Figure 6.10. Adsorption breakthrough curves of laboratory column and pilot plant with 1 mg·L^{-1} initial concentration.

In the desorption of laboratory column experiments, it could be clearly seen that chemical desorption was much more effective than thermal desorption. According to the calculation results, thermal and chemical desorption regenerated 0.37% and 94.34% of the total As. The poor efficiency of the thermal desorption was mainly because the adsorbed As on adsorbents (0.975 mg·g^{-1}) was very small and the adsorption capacities with different temperatures (293 and 343 K) were quite similar in this situation, as consistent with the obtained results from adsorption performance and thermodynamic calculation in batch experiments. The maximum concentration of chemical desorption was obtained at the second sample (101.45 mg·g^{-1}), this was because there was still some low As solution left in the column when starting the desorption. For the

chemical desorption using the pilot plant, similar results as with the laboratory column were obtained. The maximum desorption concentration was obtained at the third sample (130.88 $mg \cdot g^{-1}$), which means that 1 $mg \cdot L^{-1}$ arsenic solution could be concentrated more than 100 times by using adsorption-desorption of the pilot plant. These results prove that the sponge adsorbent can be successfully use in both the laboratory column and the pilot plant system for achieving an effective removal of As.

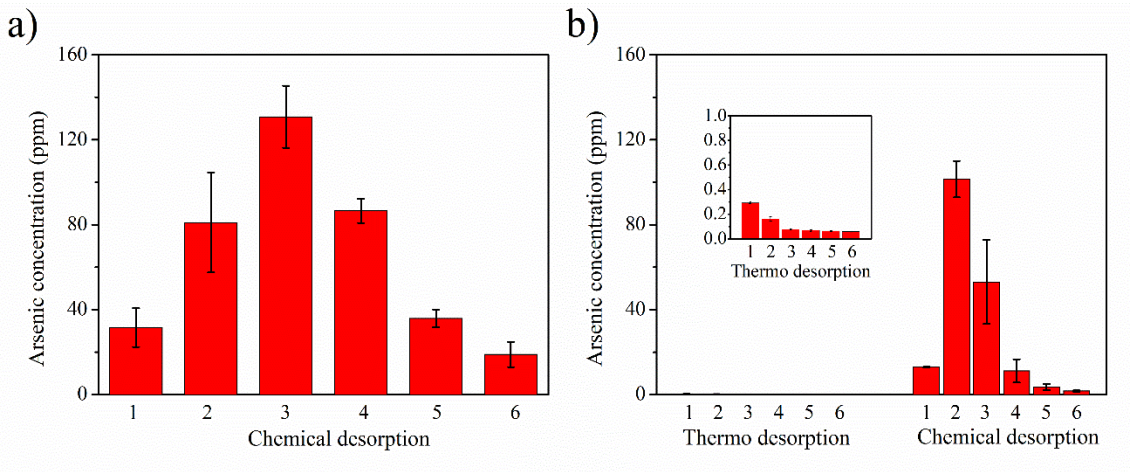

Figure 6.11. Compare of the desorption of laboratory column (a) and pilot plant (b).

Table 6.8. Desorption results of laboratory column and pilot plant.

Fix-bed column	Total amount (g)	Outlet amount (g)	As(V) in wet adsorbent (g)	Adsorbed amount (g)	Thermo desorption (g)	Chemical desorption (g)
Laboratory column	1	0.022	0.003	0.975	0.004	0.919
Pilot plant	20	0.630	0.092	19.278	no	19.240

6.5. Conclusions

In this chapter, As adsorption experiments were performed in a fixed-bed laboratory column and a pilot plant system. The number of bed volume and

adsorbed capacity of As at breakthrough point were studied under different conditions.

Several parameters of the fixed-bed breakthrough experiments such as initial concentration and the adsorbent material (sponge and sponge-loaded SPION) had a greater effect than the flow rate and/or the temperature. In both column system the As(V) removal rates were always higher than 95% for all the operating parameters studied. The results obtained for the composite material, sponge-loaded SPION, indicated that loading 2.6 wt.% SPION on the commercial cube sponge results in a 95.56% and 97.09% increment in the number of bed volume and adsorption capacity at breakthrough point, respectively, respect to sponge. For low concentrated As solutions, which are closer to more realistic polluted environmental scenarios, 1 $mg \cdot L^{-1}$, the maximum desorption concentrations obtained for both systems were higher than 100 $mg \cdot g^{-1}$. Hence, we were able to concentrate the inlet solution by 100 times which is rather relevant for industrial applications. All these results proved that both adsorbents, sponge and sponge-loaded SPION, have a great As adsorption performance when used as fixed-bed in both laboratory columns and pilot plant systems.

6.6. Reference

[1] H. Patel, Batch and continuous fixed bed adsorption of heavy metals removal using activated charcoal from neem (Azadirachta indica) leaf powder, Sci. Rep. 10 (2020) 16895. https://doi.org/10.1038/s41598-020-72583-6.

[2] N. Sureshkumar, S. Bhat, S. Srinivasan, N. Gnanasundaram, M. Thanapalan, R. Krishnamoorthy, H. Abuhimd, F. Ahmed, P.L. Show, Continuous phenol removal using a liquid–solid circulating fluidized bed, Energies. 13 (2020). https://doi.org/10.3390/en13153839.

[3] A. Negrea, M. Mihailescu, G. Mosoarca, M. Ciopec, N. Duteanu, P. Negrea, V. Minzatu, Estimation on fixed-bed column parameters of breakthrough behaviors for gold recovery by adsorption onto modified/functionalized amberlite xad7, Int. J. Environ. Res. Public Health. 17 (2020) 1–14. https://doi.org/10.3390/ijerph17186868.

[4] S. De Gisi, G. Lofrano, M. Grassi, M. Notarnicola, Characteristics and adsorption capacities of low-cost adsorbents for wastewater treatment: A review, Sustain. Mater. Technol. 9 (2016) 10–40. https://doi.org/10.1016/j.susmat.2016.06.002.

[5] A.B. Dichiara, S.J. Weinstein, R.E. Rogers, On the Choice of Batch or Fixed Bed Adsorption Processes for Wastewater Treatment, Ind. Eng. Chem. Res. 54 (2015) 8579–8586. https://doi.org/10.1021/acs.iecr.5b02350.

[6] H. Patel, Fixed-bed column adsorption study: a comprehensive review, Appl. Water Sci. 9 (2019) 45. https://doi.org/10.1007/s13201-019-0927-7.

[7] Z. Xu, J.G. Cai, B.C. Pan, Mathematically modeling fixed-bed adsorption in aqueous systems, J. Zhejiang Univ. Sci. A. 14 (2013) 155–176. https://doi.org/10.1631/jzus.A1300029.

[8] M.H. Marzbali, M. Esmaieli, Fixed bed adsorption of tetracycline on a mesoporous activated carbon: Experimental study and neuro-fuzzy modeling, J. Appl. Res. Technol. 15 (2017) 454–463. https://doi.org/10.1016/j.jart.2017.05.003.

[9] J. Lemus, C. Moya, M.A. Gilarranz, J.J. Rodriguez, J. Palomar, Fixed-bed adsorption of ionic liquids onto activated carbon from aqueous phase, J. Environ. Chem. Eng. 5 (2017) 5347–5351. https://doi.org/10.1016/j.jece.2017.10.014.

[10] E. Tetteh, Abstract Adsorption of Pharmaceuticals and Endocrine Disrupting

Compounds Using Unmodified and Surfactant Modified Palygorskite-Montmorillonite Clay Particles in Batch and Fixed Bed Column Modes, Miami University, 2018. http://rave.ohiolink.edu/etdc/view?acc_num=miami1543583842195458.

[11] M. Solgi, L.G. Tabil, L.D. Wilson, Modified biopolymer adsorbents for column treatment of sulfate species in saline aquifers, Materials (Basel). 13 (2020). https://doi.org/10.3390/ma13102408.

[12] F. Benstoem, A. Nahrstedt, M. Boehler, G. Knopp, D. Montag, H. Siegrist, J. Pinnekamp, Performance of granular activated carbon to remove micropollutants from municipal wastewater—A meta-analysis of pilot- and large-scale studies, Chemosphere. 185 (2017) 105–118. https://doi.org/10.1016/j.chemosphere.2017.06.118.

[13] M.R. Samarghandi, M. Hadi, G. McKay, Breakthrough curve analysis for fixed-bed adsorption of azo dyes using novel pine cone-derived active carbon, Adsorpt. Sci. Technol. 32 (2014) 791–806. https://doi.org/10.1260/0263-6174.32.10.791.

[14] M.S. Shafeeyan, W.M.A. Wan Daud, A. Shamiri, A review of mathematical modeling of fixed-bed columns for carbon dioxide adsorption, Chem. Eng. Res. Des. 92 (2014) 961–988. https://doi.org/10.1016/j.cherd.2013.08.018.

[15] Z.Z. Chowdhury, S.B. Abd Hamid, S.M. Zain, Evaluating design parameters for breakthrough curve analysis and kinetics of fixed bed columns for Cu(II) cations using lignocellulosic wastes, BioResources. 10 (2015) 732–749. https://doi.org/10.15376/biores.10.1.732-749.

[16] B. Manna, U.C. Ghosh, Adsorption of arsenic from aqueous solution on synthetic hydrous stannic oxide, J. Hazard. Mater. 144 (2007) 522–531. https://doi.org/10.1016/j.jhazmat.2006.10.066.

[17] Z.Z. Chowdhury, S.M. Zain, A.K. Rashid, R.F. Rafique, K. Khalid, Breakthrough curve analysis for column dynamics sorption of Mn(II) ions from wastewater by using Mangostana garcinia peel-based granular-activated carbon, J. Chem. 2013 (2013) 959761. https://doi.org/10.1155/2013/959761.

[18] F. Feizi, A.K. Sarmah, R. Rangsivek, Adsorption of pharmaceuticals in a fixed-bed column using tyre-based activated carbon: Experimental investigations and numerical modelling, J. Hazard. Mater. 417 (2021) 126010. https://doi.org/10.1016/j.jhazmat.2021.126010.

[19] S. Afroze, T.K. Sen, H.M. Ang, Adsorption performance of continuous fixed bed column for the removal of methylene blue (MB) dye using Eucalyptus sheathiana bark biomass, Res. Chem. Intermed. 42 (2016) 2343–2364. https://doi.org/10.1007/s11164-015-2153-8.

[20] C.R. Girish, V.R. Murty, Mass Transfer Studies on Adsorption of Phenol from Wastewater Using Lantana camara, Forest Waste, Int. J. Chem. Eng. 2016 (2016) 5809505. https://doi.org/10.1155/2016/5809505.

[21] M.A. Al-Ghouti, R.S. Al-Absi, Mechanistic understanding of the adsorption and thermodynamic aspects of cationic methylene blue dye onto cellulosic olive stones biomass from wastewater, Sci. Rep. 10 (2020) 15928. https://doi.org/10.1038/s41598-020-72996-3.

[22] S. Banerjee, M.C. Chattopadhyaya, Adsorption characteristics for the removal of a toxic dye, tartrazine from aqueous solutions by a low cost agricultural by-product, Arab. J. Chem. 10 (2017) S1629–S1638. https://doi.org/10.1016/j.arabjc.2013.06.005.

[23] H. Esfandian, A. Samadi-Maybodi, B. Khoshandam, M. Parvini, Experimental and CFD modeling of diazinon pesticide removal using fixed bed column with Cu-modified zeolite nanoparticle, J. Taiwan Inst. Chem. Eng. 75 (2017) 164–173. https://doi.org/10.1016/j.jtice.2017.03.024.

[24] M.Y. Prajitno, M. Taufiqurrakhman, D. Harbottle, T.N. Hunter, Kinetic studies of Cs+ and Sr2+ ion exchange using clinoptilolite in static columns and an agitated tubular reactor (Atr), ChemEngineering. 5 (2021) 1–16. https://doi.org/10.3390/chemengineering5010009.

[25] X. Cheng, X.T. Bi, Modeling NOx adsorption onto Fe/ZSM-5 catalysts in a fixed bed reactor, Int. J. Chem. React. Eng. 11 (2013) 19–30. https://doi.org/10.1515/ijcre-2012-0015.

[26] M.K. Al Mesfer, M. Danish, M.I. Khan, I.H. Ali, M. Hasan, A. El Jery, Continuous fixed bed co2 adsorption: Breakthrough, column efficiency, mass transfer zone, Processes. 8 (2020) 1–16. https://doi.org/10.3390/pr8101233.

[27] Y. Ye, J. Yang, W. Jiang, J. Kang, Y. Hu, H.H. Ngo, W. Guo, Y. Liu, Fluoride removal from water using a magnesia-pullulan composite in a continuous fixed-bed column, J. Environ. Manage. 206 (2018) 929–937. https://doi.org/10.1016/j.jenvman.2017.11.081.

[28] H. Paudyal, K. Ohto, H. Kawakita, K. Inoue, Recovery of fluoride from water through

adsorption using orange-waste gel, followed by desorption using saturated lime water, J. Mater. Cycles Waste Manag. 22 (2020) 1484–1491. https://doi.org/10.1007/s10163-020-01042-1.

[29] C.Y. Kuo, Desorption and re-adsorption of carbon nanotubes: Comparisons of sodium hydroxide and microwave irradiation processes, J. Hazard. Mater. 152 (2008) 949–954. https://doi.org/10.1016/j.jhazmat.2007.07.069.

[30] S. Lata, P.K. Singh, S.R. Samadder, Regeneration of adsorbents and recovery of heavy metals: a review, Int. J. Environ. Sci. Technol. 12 (2015) 1461–1478. https://doi.org/10.1007/s13762-014-0714-9.

Part II: Boron

Chapter 7: Boron adsorption by microwave-assisted synthesized HAM

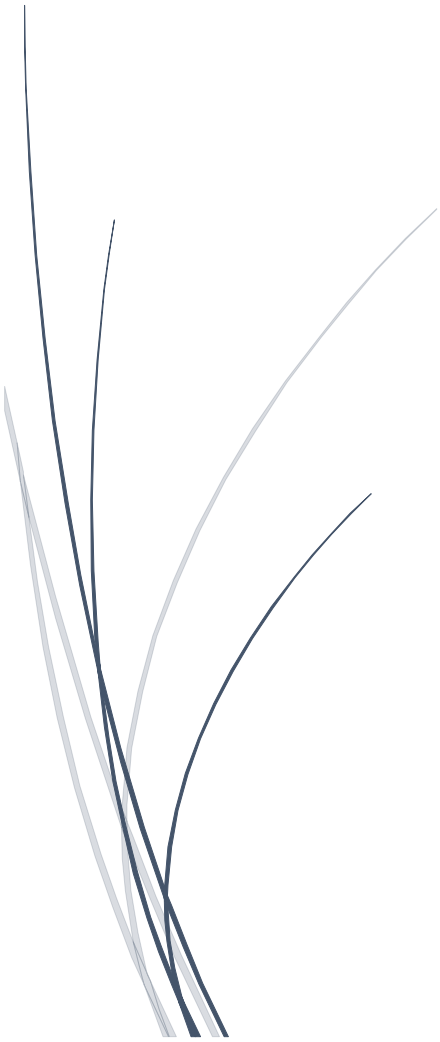

7.1. Introduction

7.1.1. Boron sources and environmental pollution.

Boron (B) is a non-metallic element that is mostly present in the earth's surface and water as boric acid and borates, but it is not found in nature in elemental form [1,2]. The average boron concentration found in the environment varies depending on the media: 30 $mg \cdot kg^{-1}$ (soil), 4.5 $mg \cdot L^{-1}$ (seawater), and 0.3~100 $mg \cdot L^{-1}$ (groundwater) [3].

Boron is released into the environment by both natural processes and anthropogenic activities [4–6]. The schematic diagram of boron turnover in the biosphere is shown in Figure 7.1. The most common naturally occurring boron compounds are borosilicate minerals, boroaluminosilicate minerals and borate minerals, which are generated from volcanic gases or hot springs [7,8]. Due to the weathering of rocks and the leaching of salt deposits, boron is released into the environment. Boron is also found naturally in seawater [9], and its concentration varies substantially depending on the geography and the location of the ocean bodies. It ranges from 0.52 $mg \cdot L^{-1}$ in the Baltic Sea to 9.6 $mg \cdot L^{-1}$ in the Mediterranean Sea [10]. Because of the geochemical nature of the drainage area, boron is also found in the rainfall in coastal areas [11]. The high volatility of boron when discharged to the environment may produce acid rainfall back to the ground, pollute the drinking water, be deposited in the soil, absorbed by plants, and lead to a series of environmental and health problems [12]. The industrial activity is another source of boron pollution [13,14]. Boric acid and boron salts are widely used in many industries devoted to the manufacture of glass, porcelain, wire drawing, semiconductors, leathers, pharmaceuticals, insecticides, catalysts, fuels, and cleaning products [15,16]. The glass industry is the biggest consumer using more than half of the total production of boron compounds [17]. Besides, the boron concentration in sewage wastewater can exceed 100 $mg \cdot L^{-1}$ [18].

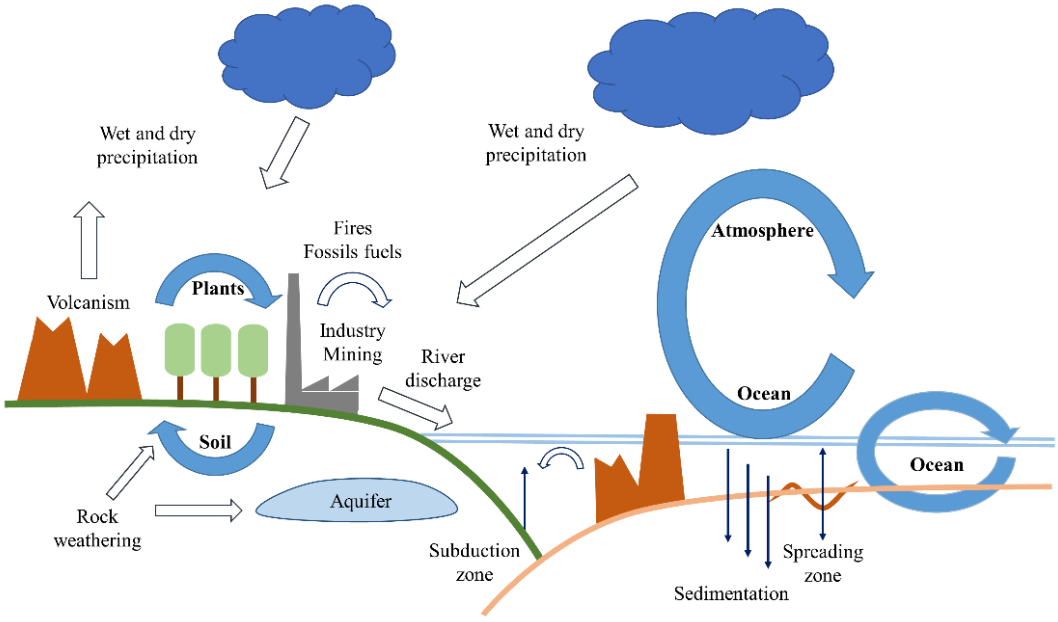

Figure 7.1. Schematic diagram of boron turnover in the environment. Adapted from [19].

7.1.2. The standard of boron

The concentration range between boron deficiency and its toxicity is very narrow [20]. Since a series of environmental and health issues caused by boron has been found, the World Health Organization (WHO) established a guideline value of 2.4 $mg \cdot L^{-1}$ as the upper limit in drinking water [21]. The European Commission regulation applies this level only when desalinated water is the main water supply or when high concentration of geologically originated boron is found in groundwater, otherwise, an overall level of 1.5 $mg \cdot L^{-1}$ is applied [22].

7.1.3. Chemistry of boron in aqueous solution

In aqueous solutions, the most common species of boron are boric acid, $B(OH)_3$, and various kinds of borates. Their fractions present in the solution depend on the pH of the solution and the element concentration [23]. Boric acid and borate oxyanion, $B(OH)_4^-$, are mainly present at low concentrations (<216 $mg \cdot L^{-1}$).

Besides, as shown in Figure 7.2, boric acid dominates at low pH, while borate ions dominate at high pH values.

At high concentration (270-6487 mg·L^{-1}), water-soluble polyborate ions such as $B_2(OH)_5^-$, $B_3O_3(OH)_4^-$ and $B_4O_5(OH)_4^{2-}$ are formed with an increase of pH value from 6.0 to 10.0 [24]. The formation of these polynuclear ions is attributed to the interaction of boric acid and borate ions in solution.

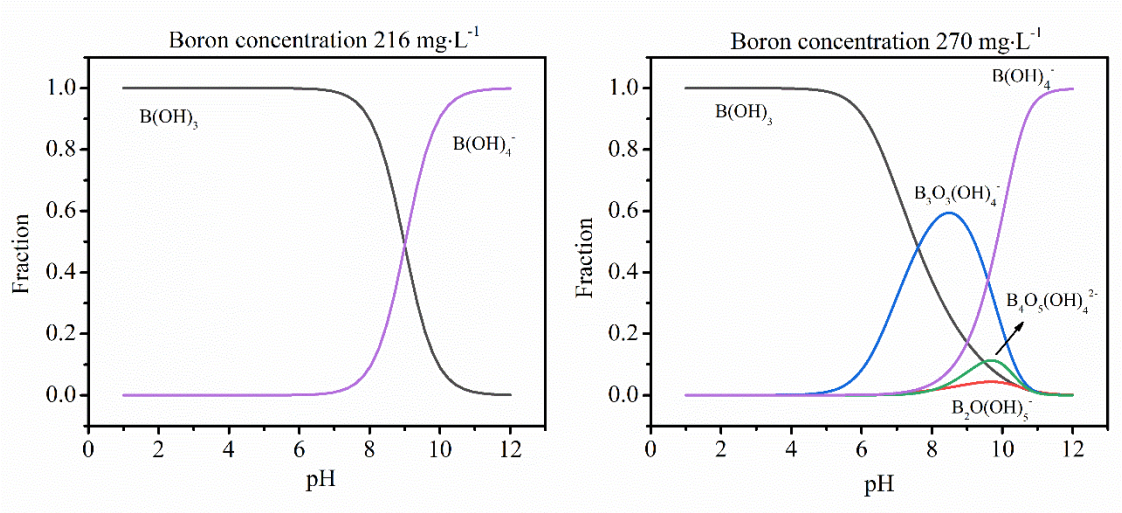

Figure 7.2. Distribution diagram of borate species in solution at various pH and different concentrations.

7.1.4. Boron removal methods

Taking into account the increasing concentration of boron in surface and groundwater, and the need for treatment of seawater and wastewater, which contains large amounts of this element, the development, and study of effective boron removal processes from aqueous solutions has become an important task [25]. The presence of many different chemical boron species in water and the regional concentration variability imposes a great challenge for efficiently and selectively remove boron from polluted water [26].

In the past decades, multiple methodologies such as precipitation [27,28], oxidation [29], extraction [30,31], ion exchange [32,33], adsorption [34–36] and

membrane [37,38] processes have been studied for boron removal. Previous works have shown that, compared to many metalloids, boron is much harder to remove. For instance, conventional processes such as coagulation, flocculation and filtration used for treating drinking water provide little or no removal of boron. Boron rejection in reverse osmosis (RO) is poor, because boron is a small species and, since it is present as an undissociated acid, it could not be rejected by the membrane due to charge difference [39]. Many advances had been introduced to membrane technologies to achieve close 90% removal; however, the removal time, material cost and the system complexity have concomitantly increased together with the removal efficiency [40]. Compared with the above methods, adsorption is considered to be one of the most promising approaches owing to its numerous advantages: high efficiency, easy operation, environmentally friendly, and low cost [41].

7.1.5. Adsorbents used for boron removal

In the past years, various traditional adsorbents, such as activated carbon [34], fly ash [42] and industrial materials [43], biomass [44] and biochar [45], have been used for boron removal. These adsorbents are low-cost and easy to get, but have low adsorption capacities and bad selectivity, because boron can hardly form complexes on the surface of these adsorbents [46]. Many types of commercial resins are also used for boron removal because they show a high boron selectivity [47,48]. However, they have poor chemical and thermal stability and their adsorption capacities (29.22 $mg \cdot g^{-1}$ for a widely used commercial resin) reported still need to be improved [49]. Besides, raw materials used for synthesizing the resins are expensive, and the cost for recycling those materials is also rather high.

Researchers all over the world are still working on the design of the novel boron adsorbents with high adsorption capacities, good selectivity and low costs. Among all adsorbent materials, γ-Al_2O_3 has a porous structure and a large

specific surface area, so it is commonly used as adsorbents, dehydrating agents, and automobile exhaust purifiers in industry [50,51]. In recent years, hierarchically structured metal oxides have recently been widely used in adsorption [52], catalysis [53], sensors [54], drug delivery [55], electronic conversion and storage [56]. Among them, hierarchical alumina microspheres (HAM) have attracted great attention due to their large specific surface area, low cost and no toxicity [57–59]. Therefore, in this study, we propose using microwave-assisted methods to synthesize γ-HAM with a large specific surface area (240-250 $m^2 \cdot g^{-1}$) [60] to remove boron from aqueous solutions.

7.1.6. Objectives

The overall objective of this work is to study the boron adsorption by microwave-assisted synthesized HAM. The main points that have been developed are:

- To successfully synthesize and fully characterize HAM;
- To investigate the adsorption behaviors of HAM under different pH values, initial concentrations, contact times;
- To better explain the adsorption behaviors by using isotherm models, kinetic models, the analysis of thermodynamics parameters;
- To study the selectivity of HAM for boron adsorption in the presence of foreign ions.
- To study the reusability of HAM by performing adsorption-desorption experiments.

7.2. Materials and Methods

7.2.1. Chemical reagents

All chemicals used in the experiments were of analytical grade (ACS reagent). The source of boron used in experiments was boric acid (H_3BO_3) from Merk

(Darmstadt, Germany). An aqueous stock solution of 1000 mg·L^{-1} boron was first prepared and then diluted as required.

Potassium sulfate dodecahydrate ($KAl(SO_4)\cdot 12H_2O$) and urea ($CO(NH_2)_2$) from Sigma-Aldrich (State of Missouri, USA) were used to synthesize HAM. Hydrogen chloride (HCl) and sodium hydroxide (NaOH) from Panreac (Barcelona, Spain) were used to adjust the pH of the solutions in the synthesis and the adsorption processes.

Carmine ($C_{22}H_{20}O_{13}$) from Sigma-Aldrich (State of Missouri, USA) and sulfuric acid (H_2SO_4) from Scharlab (Barcelona, Spain) were used as color reagents for the detection of boron by carmine colorimetric method as reported elsewhere [61]. The method is described in detail in 7.2.4.

7.2.2. Microwave-assisted synthesis of HAM

Microwave-assisted synthesis is based on the interaction of electromagnetic waves with polar solvent molecules and/or ions in solution [62]. The direct interaction of electromagnetic waves with the solution/reactant provides high heating rates, homogeneous heating, high energy efficiency and short synthesis time [63,64]. Compared with conventional heating, microwave heating results in a more homogeneous microstructure [65]. With these advantages, microwave-assisted synthesis has been widely used in organic synthesis [66], inorganic synthesis [67], polymer synthesis [68], nanotechnology [69], peptide synthesis [70].

In this study, HAM were synthesized using an analytical microwave CEM MARS-5 in accordance to the procedure described as follows [60]:

a) Aluminum sulfate and urea were mixed with 100 ml water in a 250 ml beaker to get an aqueous solution containing 0.1 M aluminum sulfate and 0.05 M urea. The mixture was stirred at 300 rpm for 15 min.

b) The resulting solution was divided into seven microwave vessels of 100 ml using a graduated cylinder, then heated 20 min by microwave with the power of 1000W at 180°C.

c) Once the system was cooled down to room temperature, the pH was adjusted to ~ 9.0 by adding 1 M NaOH solution (initial pH of the solution ~ 7.2).

d) The synthesized solid material was collected by centrifugation (3000 rpm, 5 mins) and washed with hot Milli-Q water (70°C), twice with ethanol, and a final time with hot Milli-Q water.

e) The collected precipitate was dried in oven at 80°C for 12 h.

f) The dried precipitate was calcinated in a muffle at 600°C for 2 h.

g) After cooling down to room temperature, the final lump material obtained was broken down by gently grinding and stored for future use.

Figure 7.3. CEM MARS-5 microwave used for HAM synthesis.

7.2.3. Characterizations of HAM

The morphology of the material was studied by field emission scanning electron microscope (FE-SEM, Merlin, Carl Zeiss AG, Oberkochen, Germany). X-ray powder diffraction (XRD, X-Pert, Philips, Amsterdam, Netherlands) was carried

out to identify the crystallinity of HAM.

7.2.4. Detection of Boron

Boron concentration was detected by carmine colorimetric method using UV-visible spectroscopy (UV-Vis, 2-200, UNICAM, Hanau, Germany) as follows:

a) For the calibration curve, a series of boron standard solutions within the desired concentration range (0, 0.5, 1, 2, 5, 7 and 10 $mg \cdot L^{-1}$) were prepared with Milli-Q water.

b) 2.00 ml of each solution was pipetted into a 100 ml test tube.

c) 0.1 ml of concentrated HCl solution (37%) was added to the test tube and then 10.0 ml of concentrated H_2SO_4 solution (98%) was slowly added, mix them by stirring and let cool down to room temperature.

d) Afterwards, 10.0 ml 0.05 wt.% carmine sulfate acid solution was added to the mixture.

e) After at least 60 min of color developing, the absorbance was detected at 585 nm, using a blank solution without B in the reference cuvette.

The similar procedure was followed for the detection of B in the samples after diluting the solution for the concentration to lie within the calibration range.

All containers used in the experiments were made of plastic to avoid cross contamination with boron coming from borosilicate glass. During the UV-Vis measurements, special care was taken to avoid the presence of air bubbles resulting from the incomplete mixing of the reagents. Besides, the calibration was done daily to avoid issues derived from the carmine degradation.

7.2.5. Adsorption and desorption experiments

Boron adsorption experiments were performed in a series of 50 ml plastic tubes containing 25 ml of boron solution and 0.1 g of adsorbent. The tubes were

agitated mechanically at 300 rpm, and the experiments were performed at different temperatures: 293, 318, and 343 K. The solutions were separated from the adsorbents after centrifugation (3000 rpm, 5min). The concentration of unabsorbed boron was determined by UV-Vis (see 7.2.4) to calculate the equilibrium concentration. The adsorption capacity at equilibrium was calculated using the following equation:

$$q_e = (C_o - C_e)\frac{V}{m} \quad (7.1)$$

where q_e ($mg \cdot g^{-1}$) is the adsorption capacity, V (L) is the volume of the solution, m (g) is the weight of the adsorbent, C_o and C_e ($mg \cdot L^{-1}$) are initial and equilibrium concentrations of boron, respectively.

Desorption experiments were performed using 25 ml of 0.1M HCl solution and agitating 2 h. Adsorbents were separated by centrifugation and the adsorption/desorption cycle was repeated several times.

7.2.6. Effect of competing ions and different ion strength

To examine the competing effects in the boron adsorption procedure due to the presence of other ions that may be present in natural systems, a 1:1 concentration mixture of each ion (cations and anions) and boron was used having a boron concentration of 18.50 mM (200 $mg \cdot L^{-1}$). Besides, to account for the composition of wastewater in real conditions, experiments with higher concentration ratio of different anions, [B]:[anion]=1:100, were also performed. The salt ions sources used in this study were NaCl, KCl, $CaCl_2$, $MgCl_2$ reagents; the metal ion sources used were $Ni(NO_3) \cdot 4H_2O$, $Cu(NO_3)_2 \cdot 6H_2O$, $Cr(NO_3)_2 \cdot 6H_2O$ and $Fe(NO_3)_2 \cdot 6H_2O$, reagents; the anion ion sources were NaCl, $NaNO_3$, $Na_2SO_4 \cdot 10H_2O$, $Na_3PO_4 \cdot 12H_2O$. The adsorption experiments were performed at pH 8.0 as described above.

To examine the effect the ion strength of the solution on the boron adsorption

capacity, a series of adsorption experiments were performed adding NaCl to the boron solution to a final concentration of 0-58.44 $g \cdot L^{-1}$.

7.3. Results and discussion

7.3.1. Characterizations of HAM

Getting information about the physical properties of adsorbents is very important for understanding their adsorption behaviors [71]. Therefore, various techniques were used to characterize the synthesized HAM before boron adsorption experiments. SEM and TEM were used to characterize the morphology and XRD was used to get information about the crystal structure of HAM.

7.3.1.1 SEM

The morphology of HAM was studied to provide information about shape, average size, and size distribution of the synthesized particles. SEM images (Figure 7.4a and 7.4b) show that synthesized HAM are hollow particles with highly textured surface and porous dandelion shape. This structure provides a large specific surface area, which would benefit the boron adsorption.

The SEM images were analyzed using Image-pro Plus software to determine the size distribution of the particles. The resulting histogram is shown in Figure 7.5. The average size of HAM is 1.5 +/-0.5 μm. These values are similar to those reported in previous works following similar syntheis procedure [72].

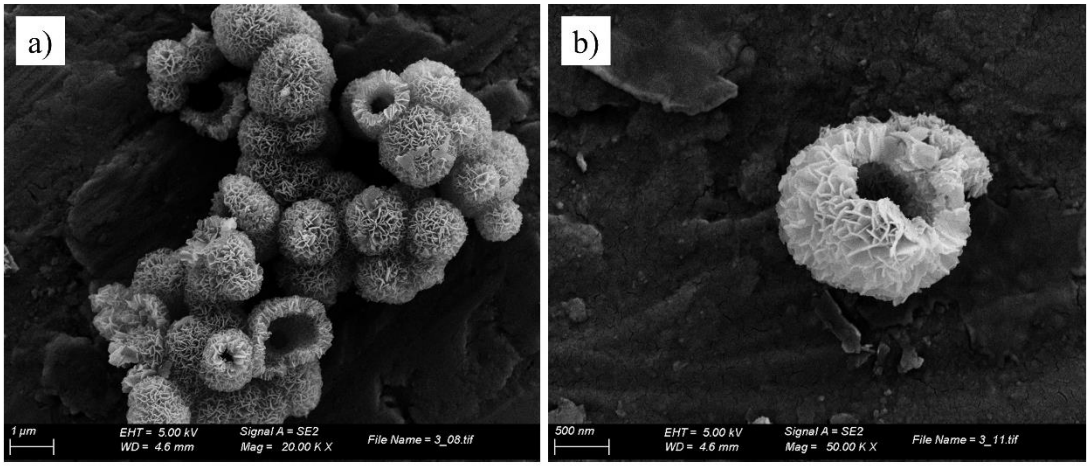

Figure 7.4. SEM images of synthesized HAM with different magnification: 20000x (a) and 50000x (b).

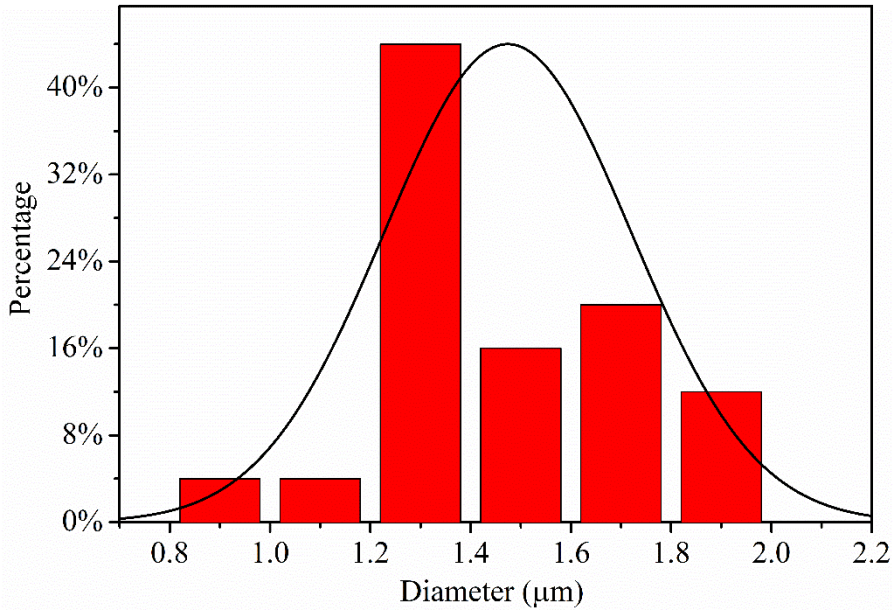

Figure 7.5. Histogram of HAM size distribution calculated by Image-Pro Plus.

7.3.1.2 TEM

Figure 7.6 shows the TEM images of HAM. In Figure 7.6a, several particles were aggregated together, but the particles can be easily identified. Figure 7.6b displays a higher magnification image of one HAM particle. These images further confirm the hollow and porous dandelion morphology of HAM. Besides, the size

of HAM determined from TEM images was consistent with the results from SEM characterization.

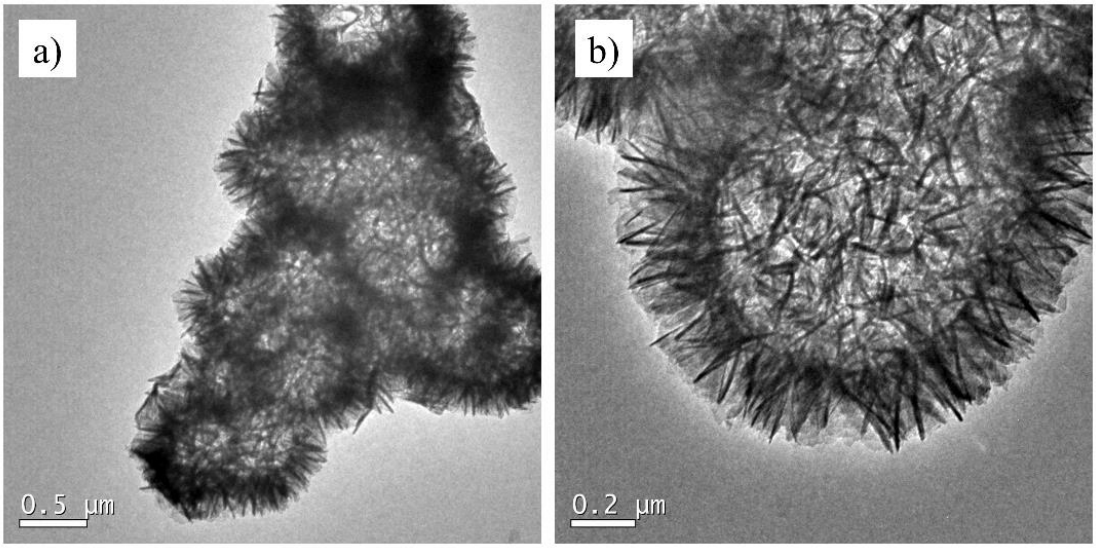

Figure 7.6. TEM images of synthesized HAM.

7.3.1.2 XRD

In this study, XRD was used to identify the crystal structure of the synthesized HAM particles. The diffraction pattern obtained is displayed in Figure 7.7 and compared with the one for γ-Al_2O_3 simulated using the crystallographic structure reported in the Crystallography Open Database [73]. Despite the fact that the diffraction peaks of the HAM particles are rather wide, the main reflections are matching with the γ-Al_2O_3 reference.

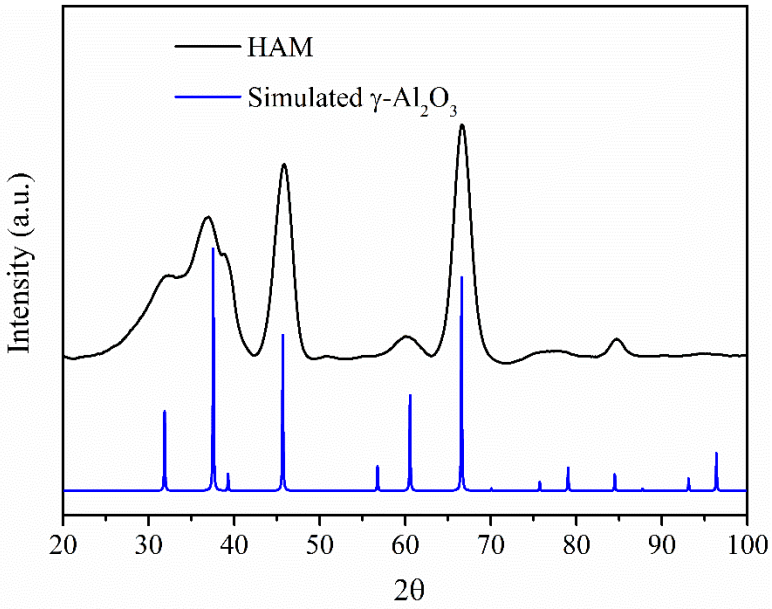

Figure 7.7. XRD spectra of synthesized HAM and simulated γ-Al_2O_3 [74].

7.3.2. Adsorption performance

In this part, batch experiments were performed to study the boron adsorption behaviors by using HAM. Different parameters (pH, contact time, initial concentration and temperature) that affect boron adsorption had been investigated.

7.3.2.1 Adsorption dependence with pH

As mentioned above, the chemical species of boron in water are influenced by the pH of the solution. Therefore, pH is an important parameter that should be investigated when studying the boron adsorption [74]. The boron adsorption capacity of HAM as a function of pH is shown in Figure 7.8.

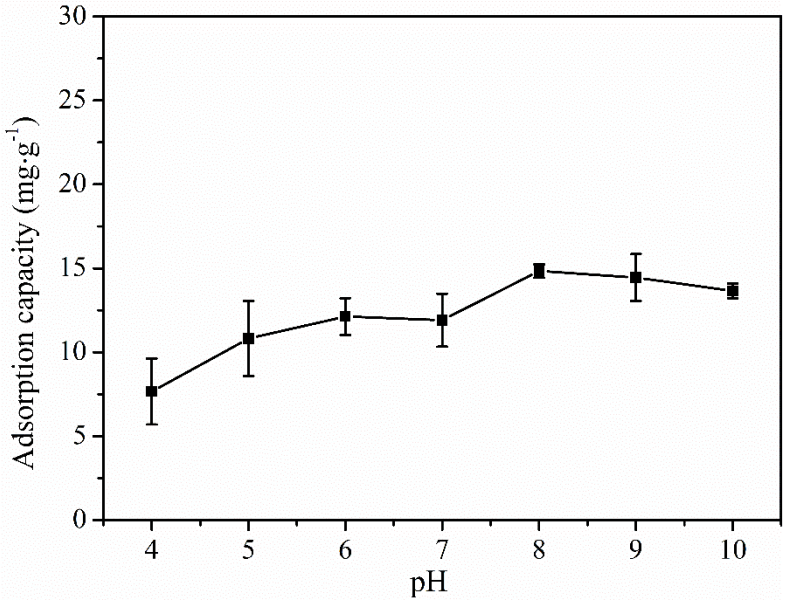

Figure 7.8. Boron adsorption capacity of HAM as a function of pH.

Our results show that, within the pH range studied, the adsorption capacity increases with the pH until reaching a maximum at pH 8.0. For higher pH, a slightly decrease is found. A plateau is found for pH around 6.0-7.0. These results are related with the change of the boron species fraction as function of pH and with the different charge of HAM surface for different pH values. As shown in Figure 7.2, for pH< 7.0, boron exists mostly as H_3BO_3, which has low affinity to HAM since boric acid is a kind of weak acid with the pK_a of 9.2. For higher values of pH, 7.0-9.0, H_3BO_3 changes to $B(OH)_4^-$. Since the pH_{pzc} of HAM is 9.0, the electrostatic attraction between boron (negative) and HAM (positive) favors the adsorption process. However, for pH>9.0, the dominant chemical form of boron is $B(OH)_4^-$, therefore, there is a electrostatic repulsion between HAM and $B(OH)_4^-$ because both of them have negative surface charges.

7.3.2.2 Contact time

Different contact time experiments from 1 min to 24 h were performed. The results displayed in Figure 7.9 reveal an initial sharp increase of the adsorption

capacity, which might be attributed to the large number of adsorption sites initially available on the surface of HAM. After 120 minutes, the adsorption capacity becomes almost constant, which means the adsorption equilibrium has been reached.

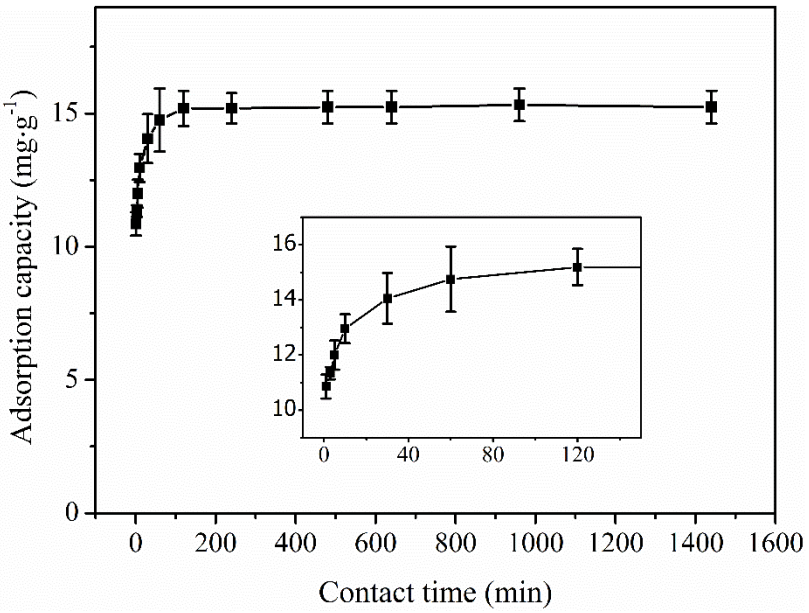

Figure 7.9. Effect of contact time on the adsorption of boron by HAM.

7.3.2.3 Initial concentration

In this experiment, different initial boron concentrations from 1 to 1000 mg·L^{-1} were studied. As can be seen in Figure 7.10, the adsorption capacity increases monotonically with boron initial concentration without reaching saturation within the concentration range studied. It is worth mentioning that the top-end of the concentration range is much higher than the concentration found in polluted waters (~ 100 mg·L^{-1}) targeted by this study.

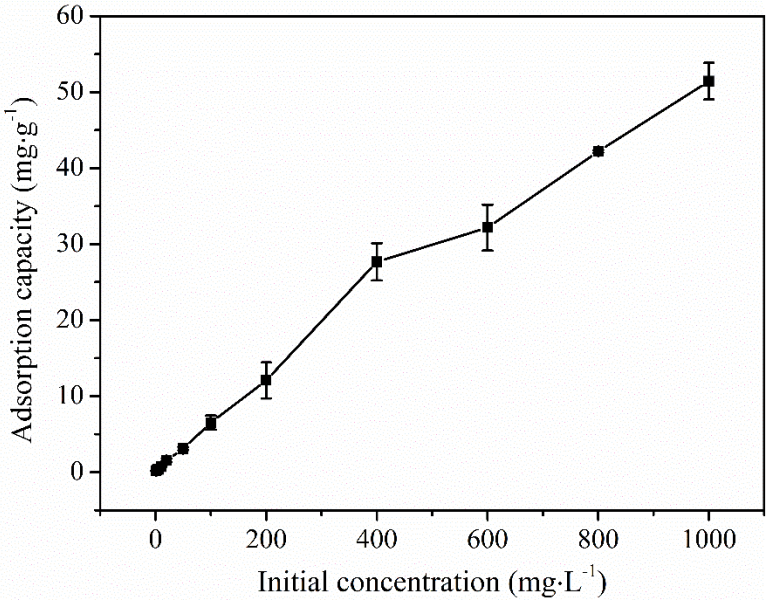

Figure 7.10. Effect of initial concentration on born adsorption capacity of HAM.

7.3.2.4 Temperature

In this part, boron adsorption experiments were performed at different temperatures (293, 318, and 343 K). The results are shown in Figure 7.11. Our result show that the adsorption capacity decreases when increasing the temperature. This indicates that the temperature has a negative effect on boron adsorption by HAM.

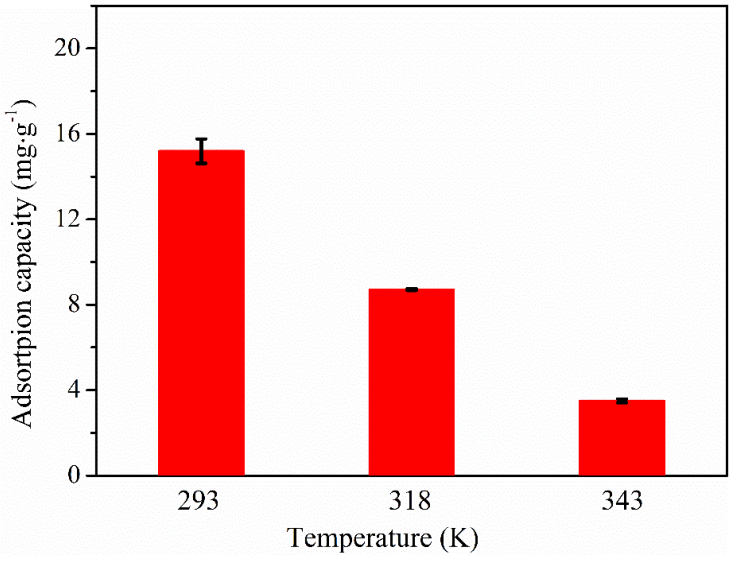

Figure 7.11. Boron adsorption capacity of HAM at different temperatures.

7.3.3. Isotherm and kinetic study

7.3.3.1 Isotherm modelling

Langmuir, Freundlich, Temkin isotherm models were used in this study to analyze the data. The forms of those three models are displayed in Annex I.

The results from the modelling are shown in Figure 7.12 and Table 7.1. Among the three models, high correlation coefficients (R^2 >0.99) were obtained for both Langmuir and Freundlich models, being the fit for Langmuir marginally better. In some reports, chemisorption was determined as the main process when the isotherms were successfully modelled by both Langmuir and Freundlich model [75–77]. Besides, for Temkin model, the value of regression coefficient is much worst, R^2 = 0.6993, which means that the boron adsorption process by HAM cannot be explained by this model.

Since the data were well fitted to the Langmuir model, the boron adsorption on HAM should be a chemisorption process on the homogenous surface [78]. The theoretical maximum capacity calculated by Langmuir was 138.50 mg·L^{-1}.

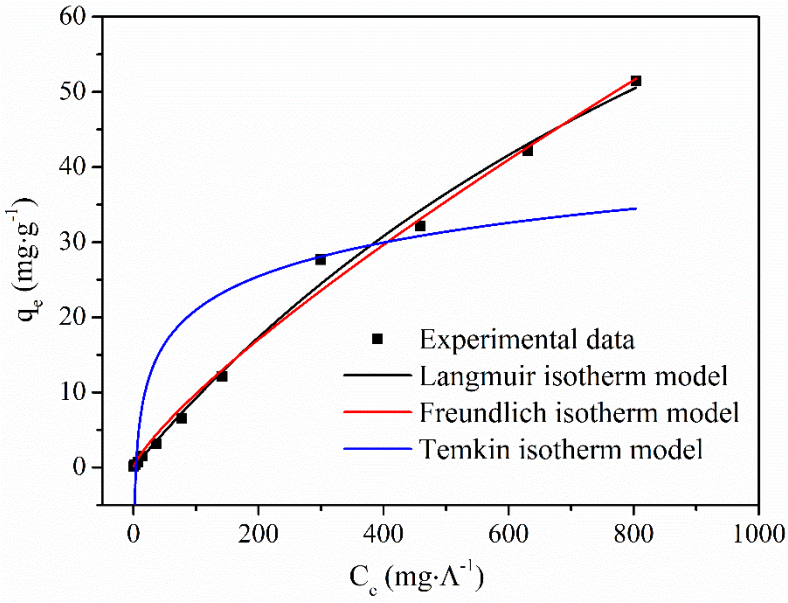

Figure 7.12. Isotherm fitting of boron adsorption by HAM.

Table 7.1. The parameters of different isotherms models of boron adsorption by HAM. The parameters are expressed in the following units: q_m ($mg \cdot g^{-1}$), K_L ($L \cdot mg^{-1}$), K_F [$(mg \cdot g^{-1})$ $(L \cdot mg^{-1})^{1/n}$], A_T ($L \cdot g^{-1}$), b_T ($K \cdot Jmol^{-1}$).

Adsorbent	Langmuir isotherm			Freundlich isotherm			Temkin isotherm		
	q_m	K_L	R^2	K_F	1/n	R^2	A_T	b_T	R^2
HAM	138.50	0.0007	0.9949	0.25	0.80	0.9931	0.26	0.38	0.6993

7.3.3.2 Kinetic modelling

Kinematic parameters are important to determine the efficiency and the mechanism responsible of the adsorption process [79]. To study the rate and mechanism of boron adsorption onto HAM surface, the experimental kinetic data were fitted to the pseudo-first order kinetic model and pseudo-second order kinetic model. The forms of those two models are displayed in Annex II.

Boron adsorption data were fitted to these two kinetic models and the results are shown in Figure 7.13 and Table 7.2. Despite obtaining a relatively good agreement with the two models (R^2 >0.90), the fitting results are better for the Pseudo-second order kinetic model. This implies that chemisorption is the speed control step in the adsorption process. Hence, the adsorption of boron on HAM involves valency forces and ion exchange mechanisms through the sharing/exchange of electrons between the adsorbent surface and boron [80,81].

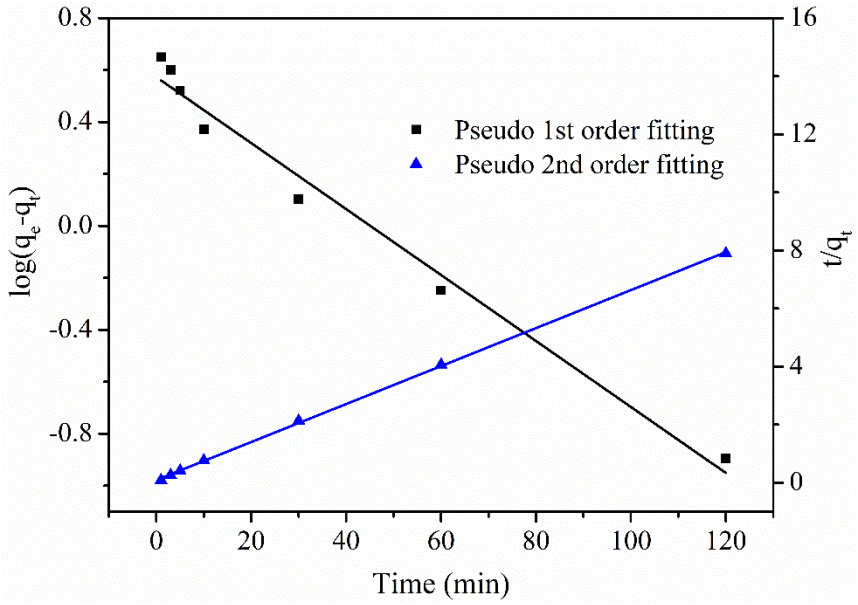

Figure 7.13. Kinetic modelling of boron adsorption by HAM.

Table 7.2. Kinetic parameters for boron adsorption on HAM.

Adsorbents	Kinetic model	R^2	Rate constant
HAM	Pseudo-first order	0.9795	K_1 (min^{-1}) = 0.0290
	Pseudo-second order	0.9996	K_2 ($g \cdot mg^{-1} \cdot min^{-1}$) = 0.0445

7.3.4. Thermodynamic analysis

Thermodynamic parameters such as Gibbs free energy change (ΔG^o), enthalpy change (ΔH^o) and entropy change (ΔS^o) can predict the feasibility and nature of the adsorption process [82,83]. The relations of these thermodynamic parameters are displayed in Annex III.

The plot of *ln K* and *1/T* and corresponding linear fit are shown in Figure 7.14. Accordingly, the values of $\Delta H°$, $\Delta S°$, $\Delta G°$ were calculated at 293, 318, and 343 K and listed in Table 7.3. Value of $\Delta H°$ is negative, which indicates the adsorption of boron by HAM is an exothermic process. However, the values for $\Delta G°$ are positive, indicating the non-spontaneous of boron adsorbed on HAM.

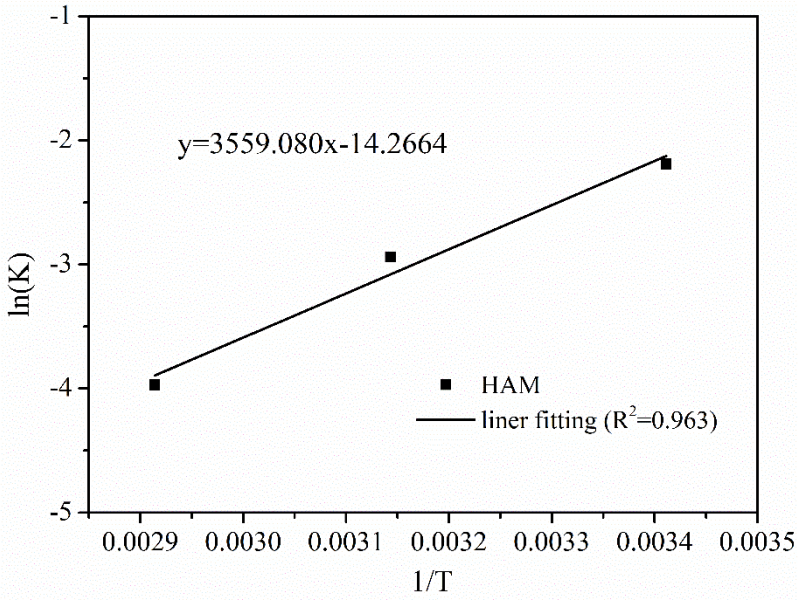

Figure 7.14. Fitting results of ln(K) vs 1/T.

Table 7.3. Thermodynamic parameters for boron adsorption onto the HAM.

Adsorbent	T (K)	ln K	ΔG^0 (kJ·mol^{-1})	ΔH^0 (kJ·mol^{-1})	ΔS^0 (J·mol^{-1})
	293	-2.19	5.18		
HAM	318	-2.94	8.15	-29.59	-118.62
	343	-3.97	11.11		

7.3.5. Effect of the foreign ions on the adsorption of boron

To investigate the possible interference of foreign ions on the selectivity of boron adsorption by HAM. Several adsorption experiments were performed with the existence of salt cations (Na^+, Mg^{2+}, K^+, Ca^{2+}) and metal cations (Cr^{2+}, Fe^{2+}, Ni^{2+} and Cu^{2+},); and anions (Cl^-, NO_3^-, SO_4^{2-}, PO_3^{3-}). The results are shown in Figure 7.15 and Figure 7.16, respectively.

For the different salt ions, the adsorption capacity was slightly lower than in the case when only boron is present. While for the metal ions, different results were obtained. For Ni^{2+} ions, the adsorption capacity also showed a slight decrease.

While with the existence of Cu^{2+}, Cr^{2+} and Fe^{2+}, the adsorption capacity increased significantly. The latter might be associate with the formation of hydroxides precipitates which can also adsorb boron ions.

Regarding the different [B]:[anion] rates, 1:1 and 1:100, see Figure 7.16, there is a small decrease in the boron adsorption capacity for 1:1. Thus, the different anions did not have a special affinity to HAM. However, when increasing the concentration of anions to have [B]:[anion]=1:100, the adsorption capacities were higher than that for1:1, especially for the PO_4^{3-} ions. This may be related to the inhibition of electrostatic interactions caused by different ion strengths. To corroborate this, boron adsorption experiments were performed with the existence of different NaCl concentrations (0~1 M, thus 0~58.44 $g \cdot L^{-1}$). The results are shown in Figure 7.17. The adsorption capacity of boron by HAM decreased at first with the competing adsorption of Na^+ and Cl^- ions. When the concentration of NaCl increase from 2.92 to 58.44 $g \cdot L^{-1}$, the adsorption of boron increased as well. This might because Na^+ and Cl^- ions could be shielding the site of the charged adsorbent and compressed the double layer of HAM, resulting in inhibition of electrostatic interactions [74].

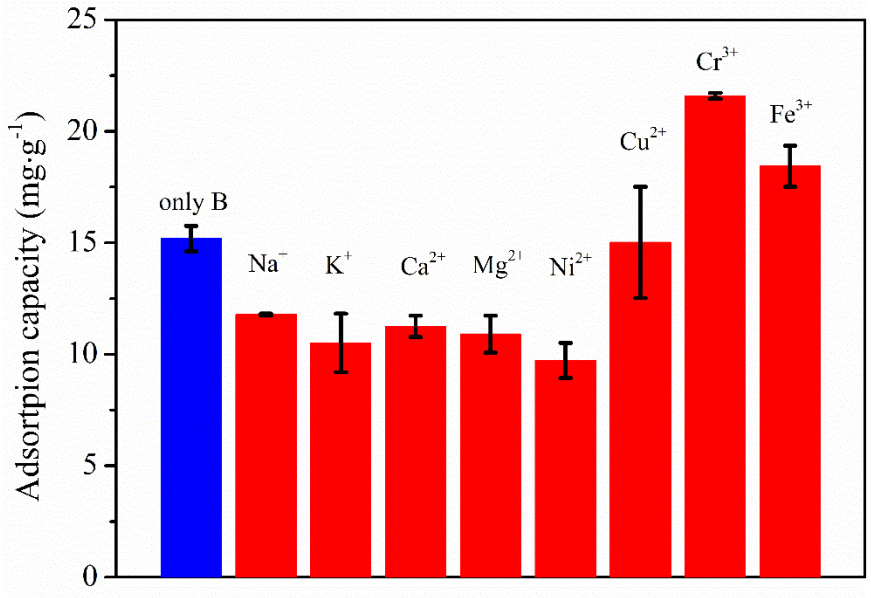

Figure 7.15. Adsorption capacity of boron with competing cations.

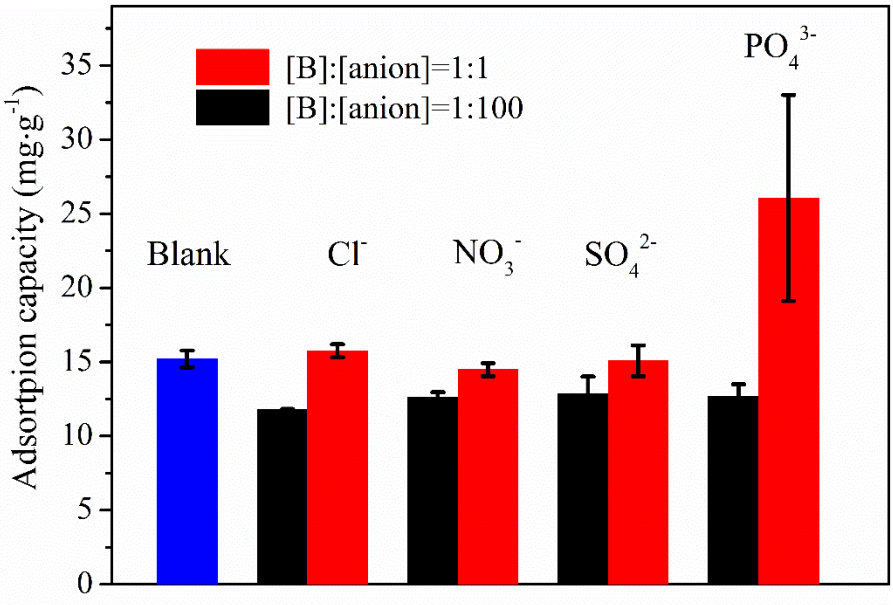

Figure 7.16. Adsorption capacity of boron with competing anions.

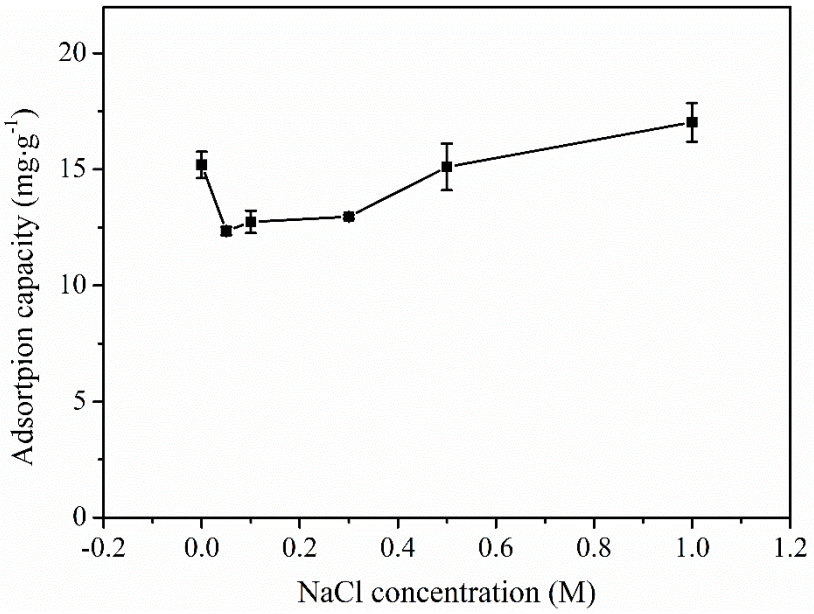

Figure 7.17. Adsorption capacity of boron with different NaCl concentrations.

7.3.6. Adsorption capacity comparison with similar adsorbent systems

As shown in Table 7.4, when comparing the maximum adsorption capacity of HAM with other adsorbents reported in the literature, we found that our value is higher than that of reported adsorbent material and commercial resins. This is

mainly because that microwave-assisted synthesized HAM have a large specific surface area due to the hollow dandelion-like structure; furthermore, hydroxyl groups on their hydrated surfaces could attract boron via surface complexation and electrostatic physisorption [88].

Table 7.4. Boron maximum adsorption capacities of some tractional materials and commercial resins.

Adsorbents	Maximum adsorption capacity ($mg \cdot g^{-1}$)	Particle size (μm)	Ref
Hierarchical alumina microspheres (HAM)	138.50	1-2	This work
Activated carbon	0.97	-	[84]
Wood sawdust	1.58	-	[84]
CL-RESIN	8.37	722–855	[85]
NCL-RESIN	8.57	710–845	[85]
IRA 743-RESIN	10.92	550–700	[85]
P(GMA-co-TRIM)-EN-PG-RESIN	29.22	< 241	[49]
P(GMA-co-TRIM)-TETA-PG-RESIN	23.25	< 273	[49]
CL-MCM-41-RESIN	19.45	1.3 nm	[86]
NCL-MCM-41-RESIN	16.73	1.4 nm	[86]
T-RESIN	21.25	-	[87]

7.3.7. Adsorption-desorption study

For practical applications, recycling and regeneration of adsorbents are essential. Therefore, the regeneration capacity of HAM was studied. The results were shown in Figure 7.18. As it can be seen, the adsorption capacity did not show significant change after the 1st regeneration. From 2nd to 5th regeneration, the adsorption capacity of HAM only showed a slight decrease. All these results indicated that HAM is a promising adsorbent with good regeneration properties regarding boron adsorption.

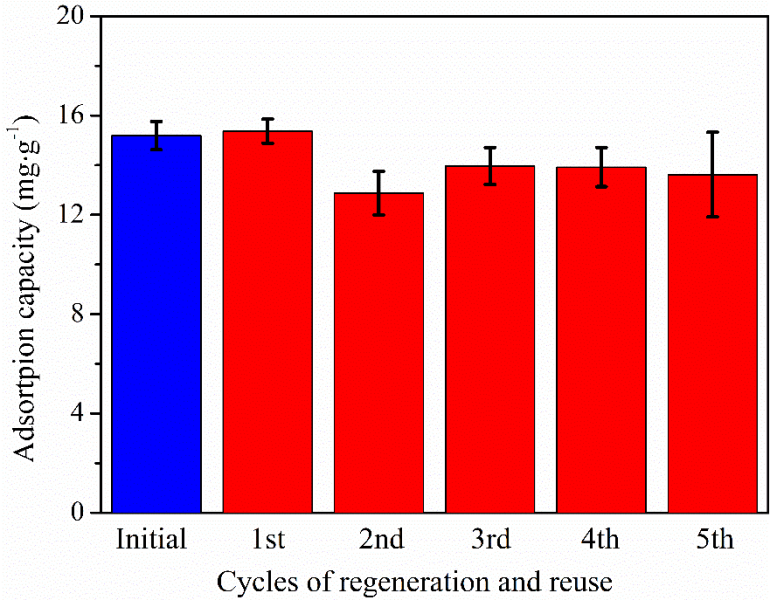

Figure 7.18. Adsorption capacity of HAM in different regeneration circle.

7.4. Conclusions

In this study, HAM was successfully synthesized by microwave-assisted co-precipitation method and used to remove boron from aqueous solution. SEM and TEM images showed that synthesized HAM are hollow particles with a fluffy and porous dandelion shape. The average size of HAM is 1.5 μm. XRD results confirmed that the crystallographic phase was γ-Al_2O_3. The adsorption data were well reproduced by the Langmuir isotherm and Pseudo-second order models, indicating that a single-layer homogeneous adsorption and chemical adsorption was the controlling step. The theoretical maximum capacity calculated by Langmuir was 138.50 mg·L^{-1}, which is higher than the adsorbents that have been previously reported in the literature.

According to thermodynamics calculation results, the value of ΔH° is negative and values of ΔG° are positive, indicating that the adsorption of boron on HAM is an exothermic and non-spontaneous process. HAM also showed high adsorption affinity and excellent selectivity towards boron in an aqueous solution, even in the presence of competitive salt ions (Na^+, K^+, Ca^{2+}, Mg^{2+}), metal

ions (Cu^{2+}, Cr^{2+}, Ni^{2+} and Fe^{2+}), anions (Cl^{-}, NO_3^{-}, SO_4^{2-}, PO_3^{3-}) and different ion strengths. In addition, no significant decrease of the adsorption performance was observed after five regeneration cycles. Therefore, HAM can be a promising adsorbent material for removing trace amounts of boron from contaminated wastewater.

7.5. Reference

[1] L. Wu, Y. Wei, W.B. Zhou, Y.S. Zhang, Q.H. Chen, M.X. Liu, Z.P. Zhu, J. Zhou, L.H. Yang, H.M. Wang, G.M. Wei, S. Wang, Z.G. Tang, Gene expression alterations of human liver cancer cells following borax exposure, Oncol. Rep. 42 (2019) 115–130. https://doi.org/10.3892/or.2019.7169.

[2] D. Schubert, Boron Oxides, Boric Acid, and Borates, Kirk-Othmer Encycl. Chem. Technol. (2011) 1–68. https://doi.org/10.1002/0471238961.0215181519130920.a01.pub3.

[3] F.S. Kot, Boron in the Environment, Boron Sep. Process. 35 (2015) 1–33. https://doi.org/10.1016/B978-0-444-63454-2.00001-0.

[4] P.F. Rodriguez-Espinosa, C. Sabarathinam, K.M. Ochoa-Guerrero, E. Martínez-Tavera, B. Panda, Geochemical evolution and Boron sources of the groundwater affected by urban and volcanic activities of Puebla Valley, south central Mexico, J. Hydrol. 584 (2020) 124613. https://doi.org/10.1016/j.jhydrol.2020.124613.

[5] H.R. Mao, C.Q. Liu, Z.Q. Zhao, Source and evolution of dissolved boron in rivers: Insights from boron isotope signatures of end-members and model of boron isotopes during weathering processes, Earth-Science Rev. 190 (2019) 439–459. https://doi.org/10.1016/j.earscirev.2019.01.016.

[6] M. Liu, Q. Guo, L. Luo, T. He, Environmental impacts of geothermal waters with extremely high boron concentrations: Insight from a case study in Tibet, China, J. Volcanol. Geotherm. Res. 397 (2020) 106887. https://doi.org/10.1016/j.jvolgeores.2020.106887.

[7] C. Helvaci, Borates, in: Encycl. Geol., Elsevier, 2021: pp. 489–504. https://doi.org/10.1016/b978-0-12-409548-9.12049-4.

[8] C. Özkul, E. Çiftçi, S. Tokel, M. Savaş, Boron as an exploration tool for terrestrial borate deposits: A soil geochemical study in Neogene Emet-Hisarcık basin where the world largest borate deposits occur (Kütahya-western Turkey), J. Geochemical Explor. 173 (2017) 31–51. https://doi.org/10.1016/j.gexplo.2016.11.014.

[9] E. Güler, C. Kaya, N. Kabay, M. Arda, Boron removal from seawater: State-of-the-art review, Desalination. 356 (2015) 85–93. https://doi.org/10.1016/j.desal.2014.10.009.

[10] D. Drohmann, F. Hernández, Risk of Regrettable Substitution under EU REACH: Level Playing Field in the EU Regulatory Context, Int. Chem. Regul. Law Rev. 3 (2020) 25–35.

https://doi.org/10.21552/icrl/2020/1/6.

[11] Y. Xu, J.Q. Jiang, Technologies for boron removal, Ind. Eng. Chem. Res. 47 (2008) 16–24. https://doi.org/10.1021/ie0708982.

[12] L. Dai, Y. Wei, X. Xu, P. Wu, M. Zhang, C. Wang, H. Li, Q. Zhang, H. Li, W. Zhu, Boron and Nitride Dual vacancies on Metal-Free Oxygen Doping Boron Nitride as Initiating Sites for Deep Aerobic Oxidative Desulfurization, ChemCatChem. 12 (2020) 1734–1742. https://doi.org/10.1002/cctc.201902088.

[13] N. Arslan, Invisible face of boron pollution in fluvial ecosystem: The level in the tissues of sentinel and nectonic organisms, Ambio. 42 (2013) 715–723. https://doi.org/10.1007/s13280-013-0383-9.

[14] C. Liu, W. Gu, Z. Dai, J. Li, H. Jiang, Q. Zhang, Boron accumulation by Lemna minor L. under salt stress, Sci. Rep. 8 (2018) 1–6. https://doi.org/10.1038/s41598-018-27343-y.

[15] H.W. Lee, K.J. Yoo, M.T. Tran, I.Y. Moon, Y.S. Oh, S.H. Kang, D.K. Kim, Effect of quenching tempering-postweld heat treatment on the microstructure and mechanical properties of laser-arc hybrid-welded boron steel, Materials (Basel). 12 (2019) 2862. https://doi.org/10.3390/ma12182862.

[16] C.G. Neochoritis, S. Shaabani, M. Ahmadianmoghaddam, T. Zarganes-Tzitzikas, L. Gao, M. Novotná, T. Mitríková, A.R. Romero, M.I. Irianti, R. Xu, J. Olechno, R. Ellson, V. Helan, M. Kossenjans, M.R. Groves, A. Dömling, Rapid approach to complex boronic acids, Sci. Adv. 5 (2019) eaaw4607. https://doi.org/10.1126/sciadv.aaw4607.

[17] B. Wang, X. Guo, P. Bai, Removal technology of boron dissolved in aqueous solutions - A review, Colloids Surfaces A Physicochem. Eng. Asp. 444 (2014) 338–344. https://doi.org/10.1016/j.colsurfa.2013.12.049.

[18] J. Kluczka, T. Korolewicz, M. Zołotajkin, J. Adamek, Boron removal from water and wastewater using new polystyrene-based resin grafted with glycidol, Water Resour. Ind. 11 (2015) 46–57. https://doi.org/10.1016/j.wri.2015.05.001.

[19] F.S. Kot, Boron sources, speciation and its potential impact on health, Rev. Environ. Sci. Biotechnol. 8 (2009) 3–28. https://doi.org/10.1007/s11157-008-9140-0.

[20] Y. Hua, T. Zhou, G. Ding, Q. Yang, L. Shi, F. Xu, Physiological, genomic and transcriptional diversity in responses to boron deficiency in rapeseed genotypes, J. Exp.

Bot. 67 (2016) 5769–5784. https://doi.org/10.1093/jxb/erw342.

[21] B. Tomaszewska, M. Bodzek, Desalination of geothermal waters using a hybrid UF-RO process. Part II: Membrane scaling after pilot-scale tests, Desalination. 319 (2013) 107–114. https://doi.org/10.1016/j.desal.2013.01.030.

[22] The European Parliament and the Council of the European Union, Directive (EU) 2020/2184, EU (revised) Drinking Water Directive. Annex 1. Part B., Off. J. Eur. Communities. 2019 (2020) 35. https://eur-lex.europa.eu/eli/dir/2020/2184/oj.

[23] C.M. Evans, D.L. Sparks, On the chemistry and mineralogy of boron in pure and in mixed systems: A review, Commun. Soil Sci. Plant Anal. 14 (1983) 827–846. https://doi.org/10.1080/00103628309367412.

[24] K. Chruszcz-Lipska, B. Winid, G.A. Madalska, J. Macuda, Ł. Łukańko, High Content of Boron in Curative Water: From the Spa to Industrial Recovery of Borates? (Poland as a Case Study), Minerals. 11 (2020) 8. https://doi.org/10.3390/min11010008.

[25] M. Tagliabue, A.P. Reverberi, R. Bagatin, Boron removal from water: Needs, challenges and perspectives, J. Clean. Prod. 77 (2014) 56–64. https://doi.org/10.1016/j.jclepro.2013.11.040.

[26] N. Kabay, E. Güler, M. Bryjak, Boron in seawater and methods for its separation - A review, Desalination. 261 (2010) 212–217. https://doi.org/10.1016/j.desal.2010.05.033.

[27] X. Vu, J.Y. Lin, Y.J. Shih, Y.H. Huang, Reclaiming Boron as Calcium Perborate Pellets from Synthetic Wastewater by Integrating Chemical Oxo-Precipitation within a Fluidized-Bed Crystallizer, ACS Sustain. Chem. Eng. 6 (2018) 4784–4792. https://doi.org/10.1021/acssuschemeng.7b03951.

[28] C. Irawan, Y.L. Kuo, J.C. Liu, Treatment of boron-containing optoelectronic wastewater by precipitation process, Desalination. 280 (2011) 146–151. https://doi.org/10.1016/j.desal.2011.06.064.

[29] S. Sarp, B. Stanford, S.A. Snyder, J. Cho, Ozone oxidation of desalinated seawater, with respect to optimized control of boron and bromate, Desalin. Water Treat. 27 (2011) 308–312. https://doi.org/10.5004/dwt.2011.2086.

[30] D. Mohapatra, G.R. Chaudhury, K.H. Park, Solvent extraction approach to recover boron from wastewater generated by the LCD manufacturing industry: Part 1, Miner. Metall.

Process. 25 (2008) 175–180. https://doi.org/10.1007/bf03403405.

[31] X. Fan, X. Yu, Y. Guo, T. Deng, Recovery of Boron from Underground Brine by Continuous Centrifugal Extraction with 2-Ethyl-1,3-hexanediol (EHD) and Its Mechanism, J. Chem. 2018 (2018). https://doi.org/10.1155/2018/7530837.

[32] A. Alharati, Y. Swesi, K. Fiaty, C. Charcosset, Comparison of boron removal by ion-exchange resin in column and hybrid membrane process, Desalin. Water Treat. 129 (2018) 34–42. https://doi.org/10.5004/dwt.2018.22805.

[33] A. Alharati, Y. Swesi, K. Fiaty, C. Charcosset, Boron removal in water using a hybrid membrane process of ion exchange resin and microfiltration without continuous resin addition, J. Water Process Eng. 17 (2017) 32–39. https://doi.org/10.1016/j.jwpe.2017.03.002.

[34] J. Kluczka, W. Pudło, K. Krukiewicz, Boron adsorption removal by commercial and modified activated carbons, Chem. Eng. Res. Des. 147 (2019) 30–42. https://doi.org/10.1016/j.cherd.2019.04.021.

[35] P. Demircivi, Application of Adsorption Methods for Boron Uptake, in: Green Adsorbents to Remove Met. Dye. Boron from Polluted Water, Springer, 2021: pp. 313–322. https://doi.org/10.1007/978-3-030-47400-3_12.

[36] T. Chen, J. Lyu, Q. Wang, P. Bai, Y. Wu, X. Guo, Mechanistic study on boron adsorption and isotopic separation with magnetic magnetite nanoparticles, J. Mater. Sci. 56 (2021) 4624–4640. https://doi.org/10.1007/s10853-020-05546-x.

[37] Z. Ali, Y. Al Sunbul, F. Pacheco, W. Ogieglo, Y. Wang, G. Genduso, I. Pinnau, Defect-free highly selective polyamide thin-film composite membranes for desalination and boron removal, J. Memb. Sci. 578 (2019) 85–94. https://doi.org/10.1016/j.memsci.2019.02.032.

[38] Y.P. Tang, L. Luo, Z. Thong, T.S. Chung, Recent advances in membrane materials and technologies for boron removal, J. Memb. Sci. 541 (2017) 434–446. https://doi.org/10.1016/j.memsci.2017.07.015.

[39] K. Baransi-Karkaby, M. Bass, V. Freger, In situ modification of reverse osmosis membrane elements for enhanced removal of multiple micropollutants, Membranes (Basel). 9 (2019) 28. https://doi.org/10.3390/membranes9020028.

[40] A. Alkhudhiri, N. Bin Darwish, M.W. Hakami, A. Abdullah, A. Alsadun, H.A. Homod, Boron removal by membrane distillation: A comparison study, Membranes (Basel). 10

(2020) 1–15. https://doi.org/10.3390/membranes10100263.

[41] J. Jung, H. Choi, S. Hong, S.J. Yoon, T.H. Kim, J.Y. Lee, Y.T. Hong, S. So, Surface-initiated ATRP of glycidyl methacrylate in the presence of divinylbenzene on porous polystyrene-based resins for boron adsorption, Desalination. 473 (2020) 114166. https://doi.org/10.1016/j.desal.2019.114166.

[42] J. Ulatowska, I. Polowczyk, A. Bastrzyk, T. Koźlecki, W. Sawiński, Fly ash as a adsorbent for boron removal from aqueous solutions: Equilibrium and thermodynamic studies, Sep. Sci. Technol. 55 (2020) 2149–2157. https://doi.org/10.1080/01496395.2019.1612434.

[43] S. Yamaguchi, T. Hongo, Synthesis of metaettringite from blast furnace slag and evaluation of its boron adsorption ability, Environ. Sci. Pollut. Res. 28 (2021) 15070–15075. https://doi.org/10.1007/s11356-020-11028-z.

[44] R. Saavedra, R. Muñoz, M.E. Taboada, M. Vega, S. Bolado, Comparative uptake study of arsenic, boron, copper, manganese and zinc from water by different green microalgae, Bioresour. Technol. 263 (2018) 49–57. https://doi.org/10.1016/j.biortech.2018.04.101.

[45] S. Mahdavi, Z. Tarhani, A.H. Sayyahzadeh, E. Naderi Peikam, Effect of Nano-MgO, Biochar and Humic Acid on Boron Stabilization in Soil in Bath and Leaching Columns, Soil Sediment Contam. 29 (2020) 595–612. https://doi.org/10.1080/15320383.2020.1752145.

[46] J. Kluczka, J. Trojanowska, M. Zolotajkin, J. Ciba, M. Turek, P. Dydo, Boron removal from wastewater using adsorbents, Environ. Technol. 28 (2007) 105–113. https://doi.org/10.1080/09593332808618769.

[47] M.M. Nasef, M. Nallappan, Z. Ujang, Polymer-based chelating adsorbents for the selective removal of boron from water and wastewater: A review, React. Funct. Polym. 85 (2014) 54–68. https://doi.org/10.1016/j.reactfunctpolym.2014.10.007.

[48] E.B. Simsek, B.F. Senkal, U. Beker, Boron Uptake from Aqueous Solution by Chelating Adsorbents: A Statistical Experimental Design Approach, Boron Sep. Process. (2015) 355–381. https://doi.org/10.1016/B978-0-444-63454-2.00017-4.

[49] Q. Luo, M. Zeng, X. Wang, H. Huang, X. Wang, N. Liu, X. Huang, Glycidol-functionalized macroporous polymer for boron removal from aqueous solution, React. Funct. Polym. 150 (2020) 104543. https://doi.org/10.1016/j.reactfunctpolym.2020.104543.

[50] Y. Huang, Y. Yang, H. Hu, M. Xu, H. Liu, X. Li, X. Wang, H. Yao, A deep insight into

arsenic adsorption over γ-Al2O3 in the presence of SO2/NO, Proc. Combust. Inst. 37 (2019) 2951–2957. https://doi.org/10.1016/j.proci.2018.06.136.

[51] S. Tabesh, F. Davar, M.R. Loghman-Estarki, Preparation of γ-Al2O3 nanoparticles using modified sol-gel method and its use for the adsorption of lead and cadmium ions, J. Alloys Compd. 730 (2018) 441–449. https://doi.org/10.1016/j.jallcom.2017.09.246.

[52] Y. Lv, L. Gao, S. Feng, S. Wang, Y. Qiao, Q. Li, Hierarchically structured Mg–Al mixed metal oxides templated from pine sawdust: fabrication, Congo red adsorption and antibacterial properties, Sep. Sci. Technol. 54 (2019) 2625–2637. https://doi.org/10.1080/01496395.2018.1548484.

[53] N. Horzum, R. Muñoz-Espí, G. Glasser, M.M. Demir, K. Landfester, D. Crespy, Hierarchically structured metal oxide/silica nanofibers by colloid electrospinning, ACS Appl. Mater. Interfaces. 4 (2012) 6338–6345. https://doi.org/10.1021/am301969w.

[54] A.-M. Cao, J.-S. Hu, H.-P. Liang, W.-G. Song, L.-J. Wan, X.-L. He, X.-G. Gao, S.-H. Xia, Hierarchically Structured Cobalt Oxide (Co 3 O 4): The Morphology Control and Its Potential in Sensors, J. Phys. Chem. B. 110 (2006) 15858–15863. https://doi.org/10.1021/jp0632438.

[55] W. Li, Y. Li, Z. Liu, N. Kerdsakundee, M. Zhang, F. Zhang, X. Liu, T. Bauleth-Ramos, W. Lian, E. Mäkilä, M. Kemell, Y. Ding, B. Sarmento, R. Wiwattanapatapee, J. Salonen, H. Zhang, J.T. Hirvonen, D. Liu, X. Deng, H.A. Santos, Hierarchical structured and programmed vehicles deliver drugs locally to inflamed sites of intestine, Biomaterials. 185 (2018) 322–332. https://doi.org/10.1016/j.biomaterials.2018.09.024.

[56] R. Guo, W. Yue, Y. Ren, W. Zhou, Hierarchical structured graphene/metal oxide/porous carbon composites as anode materials for lithium-ion batteries, Mater. Res. Bull. 73 (2016) 102–110. https://doi.org/10.1016/j.materresbull.2015.08.027.

[57] S.G. Lanas, M. Valiente, E. Aneggi, A. Trovarelli, M. Tolazzi, A. Melchior, Efficient fluoride adsorption by mesoporous hierarchical alumina microspheres, RSC Adv. 6 (2016) 42288–42296. https://doi.org/10.1039/c5ra27371d.

[58] M. Tian, X. Cui, C. Dong, Z. Dong, Palladium nanoparticles dispersed on the hollow aluminosilicate microsphere@hierarchical γ-AlOOH as an excellent catalyst for the hydrogenation of nitroarenes under ambient conditions, Appl. Surf. Sci. 390 (2016) 100–106. https://doi.org/10.1016/j.apsusc.2016.08.073.

[59] K.K. Yadav, N. Gupta, V. Kumar, S.A. Khan, A. Kumar, A review of emerging adsorbents and current demand for defluoridation of water: Bright future in water sustainability, Environ. Int. 111 (2018) 80–108. https://doi.org/10.1016/j.envint.2017.11.014.

[60] G. Lanas, S. Isabel, Fluoride and metal ions removal from water by adsorption on nanostructured materials, (2017). https://hdl.handle.net/10803/403774.

[61] T.M. Salman, R.K. Fakher Alfahed, H.A. Badran, K.I. Ajeel, M.M. Jafer, K.K. Mohammad, The evaluation and analysing the boron concentration rate in soil of north Basrah city (Iraq) by carmine method, in: J. Phys. Conf. Ser., IOP Publishing, 2019: p. 22006. https://doi.org/10.1088/1742-6596/1294/2/022006.

[62] A. Morsali, L. Hashemi, Nanoscale coordination polymers: Preparation, function and application, in: D. Ruiz-Molina, R.B.T.-A. in I.C. van Eldik (Eds.), Adv. Inorg. Chem., Academic Press, 2020: pp. 33–72. https://doi.org/10.1016/bs.adioch.2020.03.007.

[63] V. Palma, D. Barba, M. Cortese, M. Martino, S. Renda, E. Meloni, Microwaves and heterogeneous catalysis: A review on selected catalytic processes, Catalysts. 10 (2020). https://doi.org/10.3390/catal10020246.

[64] G.B. Dudley, R. Richert, A.E. Stiegman, On the existence of and mechanism for microwave-specific reaction rate enhancement, Chem. Sci. 6 (2015) 2144–2152. https://doi.org/10.1039/c4sc03372h.

[65] C. Leonelli, P. Veronesi, L. Denti, A. Gatto, L. Iuliano, Microwave assisted sintering of green metal parts, J. Mater. Process. Technol. 205 (2008) 489–496. https://doi.org/10.1016/j.jmatprotec.2007.11.263.

[66] Á. Díaz-Ortiz, P. Prieto, A. de la Hoz, A Critical Overview on the Effect of Microwave Irradiation in Organic Synthesis, Chem. Rec. 19 (2019) 85–97. https://doi.org/10.1002/tcr.201800059.

[67] M.B. Schütz, L. Xiao, T. Lehnen, T. Fischer, S. Mathur, Microwave-assisted synthesis of nanocrystalline binary and ternary metal oxides, Int. Mater. Rev. 63 (2018) 341–374. https://doi.org/10.1080/09506608.2017.1402158.

[68] M. Adamski, T.J.G. Skalski, S. Xu, M. Killer, E.M. Schibli, B.J. Frisken, S. Holdcroft, Microwave-assisted Diels-Alder polycondensation of proton conducting poly(phenylene)s, Polym. Chem. 10 (2019) 1668–1685. https://doi.org/10.1039/c8py01804a.

[69] A. Kumar, Y. Kuang, Z. Liang, X. Sun, Microwave chemistry, recent advancements, and eco-friendly microwave-assisted synthesis of nanoarchitectures and their applications: a review, Mater. Today Nano. 11 (2020) 100076. https://doi.org/10.1016/j.mtnano.2020.100076.

[70] A. Kumar, Y.E. Jad, J.M. Collins, F. Albericio, B.G. De La Torre, Microwave-Assisted Green Solid-Phase Peptide Synthesis Using γ-Valerolactone (GVL) as Solvent, ACS Sustain. Chem. Eng. 6 (2018) 8034–8039. https://doi.org/10.1021/acssuschemeng.8b01531.

[71] O.R. Brown, M.B.B.M. Yusof, M.R. Bin Salim, K. Ahmed, Physico-chemical properties of palm oil fuel ash as composite adsorbent in kaolin clay landfill liner system, in: 2011 IEEE 1st Conf. Clean Energy Technol. CET 2011, 2011: pp. 269–274. https://doi.org/10.1109/CET.2011.6041495.

[72] G. Lanas, S. Isabel, Fluoride and metal ions removal from water by adsorption on nanostructured materials, 2017. https://hdl.handle.net/10803/403774.

[73] L. Smrcok, V. Langer, J. Krestan, [gamma]-Alumina: a single-crystal X-ray diffraction study, Acta Crystallogr. Sect. C. 62 (2006) i83–i84. https://doi.org/10.1107/S0108270106026850.

[74] V. Claude, J.G. Mahy, F. Micheli, J. Geens, S.D. Lambert, Sol-gel Ni/Γ-Al2O3 material as secondary catalyst for toluene reforming: Tailoring the Γ-Al2O3 substrate with stearic acid, Microporous Mesoporous Mater. 291 (2020) 109681. https://doi.org/10.1016/j.micromeso.2019.109681.

[75] C. Wang, L. Boithias, Z. Ning, Y. Han, S. Sauvage, J.M. Sánchez-Pérez, K. Kuramochi, R. Hatano, Comparison of Langmuir and Freundlich adsorption equations within the SWAT-K model for assessing potassium environmental losses at basin scale, Agric. Water Manag. 180 (2017) 205–211. https://doi.org/10.1016/j.agwat.2016.08.001.

[76] C. Ng, J.N. Losso, W.E. Marshall, R.M. Rao, Freundlich adsorption isotherms of agricultural by-product-based powdered activated carbons in a geosmin-water system, Bioresour. Technol. 85 (2002) 131–135. https://doi.org/10.1016/S0960-8524(02)00093-7.

[77] J.H. Potgieter, Adsorption of methylene blue on activated carbon: An experiment illustrating both the langmuir and freundlich isotherms, J. Chem. Educ. 68 (1991) 349–350. https://doi.org/10.1021/ed068p349.

[78] Y. Wang, J. Wiener, G. Zhu, Langmuir isotherm models applied to the sorption of acid dyes from effluent onto polyamide nanofibers, Autex Res. J. 13 (2013) 95–98. https://doi.org/10.2478/v10304-012-0028-2.

[79] S. Nethaji, A. Sivasamy, A.B. Mandal, Adsorption isotherms, kinetics and mechanism for the adsorption of cationic and anionic dyes onto carbonaceous particles prepared from Juglans regia shell biomass, Int. J. Environ. Sci. Technol. 10 (2013) 231–242. https://doi.org/10.1007/s13762-012-0112-0.

[80] X. Hu, L. Jia, J. Cheng, Z. Sun, Magnetic ordered mesoporous carbon materials for adsorption of minocycline from aqueous solution: Preparation, characterization and adsorption mechanism, J. Hazard. Mater. 362 (2019) 1–8. https://doi.org/10.1016/j.jhazmat.2018.09.003.

[81] S.K. Singh, T.G. Townsend, D. Mazyck, T.H. Boyer, Equilibrium and intra-particle diffusion of stabilized landfill leachate onto micro- and meso-porous activated carbon, Water Res. 46 (2012) 491–499. https://doi.org/10.1016/j.watres.2011.11.007.

[82] B. Adane, K. Siraj, N. Meka, Kinetic, equilibrium and thermodynamic study of 2-chlorophenol adsorption onto Ricinus communis pericarp activated carbon from aqueous solutions, Green Chem. Lett. Rev. 8 (2015) 1–12. https://doi.org/10.1080/17518253.2015.1065348.

[83] E.C. Lima, A. Hosseini-Bandegharaei, J.C. Moreno-Piraján, I. Anastopoulos, A critical review of the estimation of the thermodynamic parameters on adsorption equilibria. Wrong use of equilibrium constant in the Van't Hoof equation for calculation of thermodynamic parameters of adsorption, J. Mol. Liq. 273 (2019) 425–434. https://doi.org/10.1016/j.molliq.2018.10.048.

[84] M. Jaouadi, Characterization of activated carbon, wood sawdust and their application for boron adsorption from water, Int. Wood Prod. J. 12 (2021) 22–33. https://doi.org/10.1080/20426445.2020.1785605.

[85] J. Lyu, Z. Zeng, N. Zhang, H. Liu, P. Bai, X. Guo, Pyrocatechol-modified resins for boron recovery from water: Synthesis, adsorption and isotopic separation studies, React. Funct. Polym. 112 (2017) 1–8. https://doi.org/10.1016/j.reactfunctpolym.2016.12.016.

[86] Y. Chen, J. Lyu, Y. Wang, T. Chen, Y. Tian, P. Bai, X. Guo, Synthesis, Characterization, Adsorption, and Isotopic Separation Studies of Pyrocatechol-Modified MCM-41 for

Efficient Boron Removal, Ind. Eng. Chem. Res. 58 (2019) 3282–3292. https://doi.org/10.1021/acs.iecr.8b04748.

[87] S. Bai, J. Han, C. Du, J. Li, W. Ding, Removal of boron and silicon by a modified resin and their competitive adsorption mechanisms, Environ. Sci. Pollut. Res. 27 (2020) 30275–30284. https://doi.org/10.1007/s11356-020-09308-9.

[88] S. Bhagyaraj, M.A. Al-Ghouti, P. Kasak, I. Krupa, An updated review on boron removal from water through adsorption processes, Emergent Mater. (2021). https://doi.org/10.1007/s42247-021-00197-3.

Chapter 8: Conclusions and future perspectives

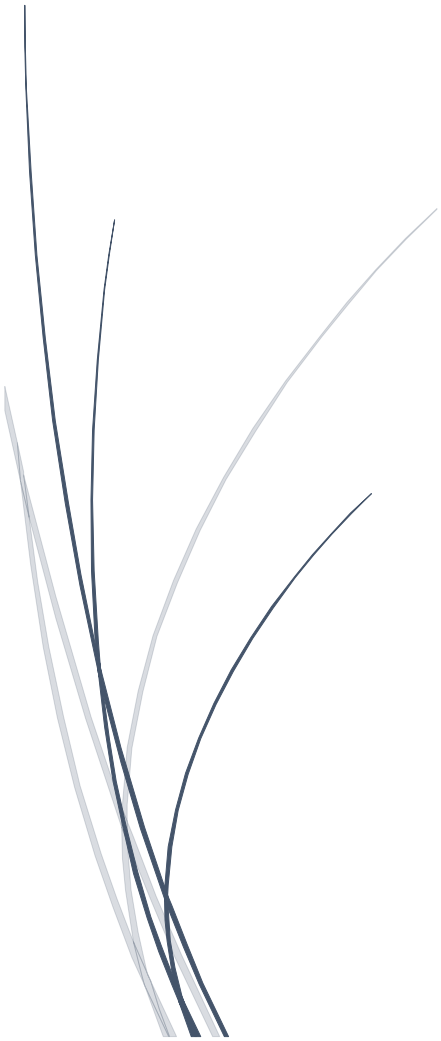

8.1. Conclusions

The conclusions collected in each chapter, have been summarized below under the main topics of the present thesis:

For Arsenic adsorption removal:

In this study, the composite adsorbent cube-shaped open-celled cellulose commercial sponge-loaded SPION was successfully synthesized by the in-situ co-precipitation method. XAS measurements at the Fe K-edge and TEM identified maghemite as the main iron phase of the SPION nanoparticles (average size ~13 nm).

Batch adsorption experiments of As(V) adsorption showed that adsorption capacity of sponge had a 28.3% enhancement after loading 2.6 wt.% mass fraction of SPION. Cube sponge-loaded SPION had a higher adsorption capacity compared with similar system adsorbents reported. The adsorption of As(V) by sponge-loaded SPION fitted well by Freundlich isotherm, indicating a multilayer and heterogeneous adsorption. Kinetic studies showed As(V) adsorption followed pseudo-second order kinetic model, suggesting chemical adsorption was the controlling step. Thermodynamics calculation indicates the adsorption was spontaneous and exothermic. In addition, we have observed that As(V) was not reduced to more toxic As(III) after adsorbed on the surface of adsorbents, which is desirable for the treatment of As(V) contaminated waters. The modeling of the EXAFS signals revealed that the binuclear corner-sharing, ^{2}C, configuration is the main one. Moreover, we have shown that the cube-shaped sponge-loaded SPION has good regenerative performance and can be used over many adsorption/desorption cycles.

Batch experiments of As(III) adsorption showed that the 2.6 wt.% of SPION loaded in the sponge outperforms the adsorption of the unsupported SPION. Normalizing by the mass fraction of the SPION, the adsorption capacity of the

composite is ~14 times larger than the one of the unsupported SPION. The adsorption of As(III) on this composite adsorbent was best described by the Temkin isotherm model and the pseudo-second order kinetic model which indicates that chemisorption is controlling the speed of the adsorption process. The assessment of the thermodynamic parameters $\Delta H°$ and $\Delta G°$ indicated that the As(III) adsorption on the composite adsorbent kept the same properties (spontaneous and endothermic) as the unsupported SPION. In addition, we have observed that the highly toxic and carcinogenic As(III) was oxidized to less toxic As(V), which is desirable for the treatment of As(III)-contaminated waters. Our XAS study supports that, after adsorption, As(III) was oxidized to As(V) by both the •OH radicals generated from Fe(III) and the -OH groups present in SPION and sponge adsorbents under neutral conditions. Besides, similar oxidation level of the adsorbed As(III) was found at different cube depths which demonstrates that the same adsorption process takes place at the different parts of the cube due to the good diffusion properties of the sponge material and the rather homogeneity of the SPION loaded in the porous sponge.

In the fixed-bed column adsorption study, several parameters of the fixed-bed breakthrough experiments such as initial concentration and the adsorbent material (sponge and sponge-loaded SPION) had a greater effect than the flow rate and/or the temperature. In both column systems, the As(V) removal rates were always higher than 95% for all the operating parameters studied. The results obtained for the composite material, sponge-loaded SPION, indicated that loading 2.6 wt.% SPION on the commercial cube sponge results in a 95.56% and 97.09% increment in the number of bed volumes and adsorption capacity at breakthrough point, respectively, respect to sponge. For low concentrated As solutions, which are closer to more realistic polluted environmental scenarios, 1 $mg \cdot L^{-1}$, the maximum desorption concentrations obtained for both systems were higher than 100 $mg \cdot g^{-1}$. Hence, we were able to concentrate the inlet

solution by 100 times which is rather relevant for industrial applications. All these results proved that both adsorbents, sponge and sponge-loaded SPION, have a great As adsorption performance when used as fixed-bed in both laboratory columns and pilot plant systems.

For Boron adsorption removal:

In this study, HAM was successfully synthesized by microwave-assisted co-precipitation method and used to remove boron from aqueous solutions. SEM TEM and XRD analysis showed that synthesized HAM is hollow γ-Al_2O_3 particles with a fluffy and porous dandelion shape and an average size of 1.5 μm. Adsorption data were fitted well to Langmuir isotherm and Pseudo-second order model, indicating a single-layer homogeneous adsorption and chemical adsorption was the controlling step. The theoretical maximum capacity calculated by Langmuir was 138.50 $mg \cdot g^{-1}$, which is higher than the adsorbents reported before.

According to thermodynamics calculation results, the value of $\Delta H°$ is negative and values of $\Delta G°$ are positive, indicating the adsorption of boron on HAM is an exothermic and non-spontaneous process. HAM also showed high adsorption affinity and excellent selectivity towards boron in an aqueous solution, even in the presence of competitive salt ions, metal ions anions and different ion strengths. In addition, the adsorbent particles could be recyclable up to five cycles without a considerable decrease in the boron removal efficiency.

8.2 Future perspectives

Considering the results obtained in this thesis, the following aspects can be considered for future perspectives.

For As adsorption system, an excellent commercial cube adsorbent with cheap

price, good adsorption capacity, quick adsorption kinetic, and promising for industrial use has been successfully synthesized and its adsorption behaviors have been fully investigated. However, there are still some aspects that need further study in the synthesis. Firstly, the iron oxide nanoparticles that we obtained are maghemite (γ-Fe_2O_3). The behavior of cube sponge loaded-magnetite (Fe_3O_4) nanoparticles would be interesting to investigate and compare with maghemite composite material as well. Secondly, the synthesis method of cube sponge-loaded SPION is the in-situ co-precipitation method. It would be necessary to develop a large-scale synthesis method, such as spray-drying and fluidized-bed method. This would be further reducing the price of the total system and more promising for industrial use.

For boron adsorption system, the maximum adsorption of hierarchical alumina microspheres (HAM) is 138.50 $mg \cdot g^{-1}$, which is higher than the adsorbents reported before. It would be interesting to do the modification of HAM and further improve its adsorption capacity, for example using the N-Methyl-D-glucamine (NMDG). Besides, as we considered in As system, it would be necessary to find support materials to reduce the aggregation of HAM, such as sponge, membrane, and nanofiber, before using in industry.

Annex

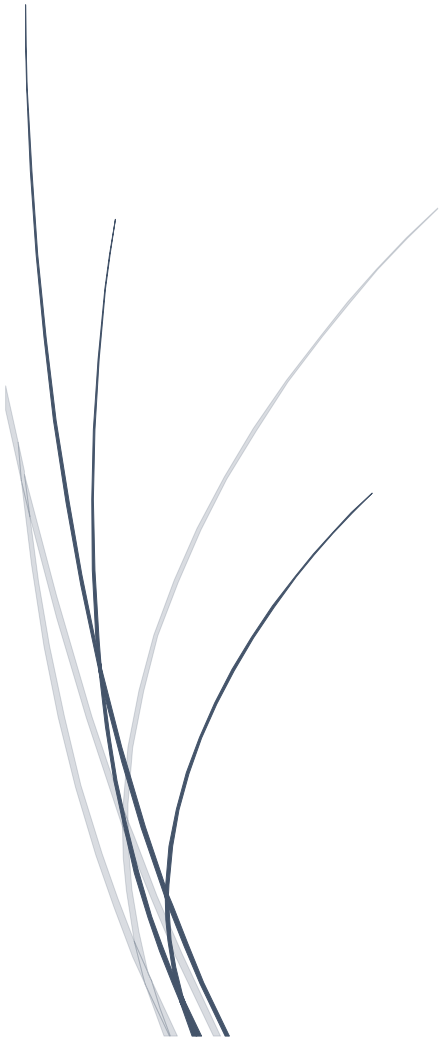

Annex I

Isotherm model introduction

For adsorption of heavy metals and metalloids from aqueous solution, Langmuir, Freundlich, and Temkin are the most commonly used isotherm models because of the usefulness of their model parameters, their simplicity, and their easy interpretability. Langmuir model assumes that the adsorption occurs on a homogeneous surface and that all binding sites have equal affinity for the adsorbate [1]. Freundlich isotherm assumes multilayer adsorption, with non-uniform distribution of adsorption heat and affinities over the heterogeneous surface [2]. Temkin isotherm contains a factor that explicitly considers the adsorbent–adsorbate interactions and it is mostly used for electrostatic interaction-based chemical adsorption [3]. The models are described by the following equations:

Langmuir isotherm model:

$$\frac{1}{q_e} = \left(\frac{1}{K_L q_m}\right)\frac{1}{C_e} + \frac{1}{q_m} \quad \text{(Annex 1)}$$

Freundlich isotherm model:

$$log\ q_e = log\ k_F + \frac{1}{n} log\ C_e \quad \text{(Annex 2)}$$

Temkin isotherm model:

$$q_e = \frac{RT}{b_T} ln\ A_T + \frac{RT}{b_T} ln\ C_e \quad \text{(Annex 3)}$$

where q_e and q_m ($mg \cdot g^{-1}$) are the equilibrium and maximum adsorption capacity, respectively. C_e ($mg \cdot g^{-1}$) is the concentration remaining in the solution. K_L ($L \cdot mg^{-1}$) is the Langmuir constant, which is related to the pollutant affinity to binding sites. K_F ($mg \cdot g^{-1}$)($L \cdot mg^{-1}$)$^{1/n}$ and n are Freundlich adsorption constants, and $\frac{1}{n}$ gives an indication of the preferential adsorption process. R is the ideal

gas constant 8.3145 ($J \cdot mol^{-1} \cdot K^{-1}$) and T (K) is the absolute temperature. A_T ($L \cdot g^{-1}$) and b_T ($KJ \cdot mol^{-1}$) are Temkin constants, which are linked to the maximum binding energy and heat of adsorption, respectively.

Annex II

Kinetic model introduction

Kinematic parameters are important to determine the efficiency and mechanism of the adsorption process [4]. To study the rate and mechanism of As(V) adsorption onto sponge-loaded SPION, the experimental kinetic data were fitted to the pseudo-first order kinetic model and pseudo-second order kinetic model, which can be expressed by the following equations [1]:

Pseudo-first order kinetic model:

$$log(q_e - q_t) = log\, q_e - \frac{K_1}{2.303} t \qquad \text{(Annex 4)}$$

Pseudo-second order kinetics model:

$$\frac{t}{q_t} = \frac{1}{K_2 q_e^2} + \frac{t}{q_e} \qquad \text{(Annex 5)}$$

Where, q_e and q_t ($mg \cdot g^{-1}$) are the adsorption capacity at equilibrium and at any time t (min), respectively; K_1 and K_2 are the rate constants of each respective model.

Annex III

Thermodynamic parameters such as Gibbs free energy change (ΔG^o), enthalpy change (ΔH^o) and entropy change (ΔS^o) can predict the feasibility and nature of the adsorption process [5,6]. The free energy of adsorption is related to the temperature as given by the following relationship:

$$\Delta G^o = -RTlnK^o \quad \text{(Annex 6)}$$

where, K^o is the standard distribution coefficient of the adsorption [7].

$$K^o = \frac{q_e}{q^o} / \frac{C_e}{C^o} \quad \text{(Annex 7)}$$

where, q^o and C^o and are the standard states of solution in solid and liquid, respectively. Here, q^o is selected as 1 mol·kg^{-1}, and C^o is selected as 1 mol·L^{-1}.

$\Delta G°$ is also related to $\Delta S°$ and $\Delta H°$ as

$$\Delta G^o = \Delta H^o - T\Delta S^o \quad \text{(Annex 8)}$$

By constructing a plot of $ln\,K$ versus $1/T$, $\Delta S°$ can be calculated from the intercept and $\Delta H°$ can be obtained from the slope.

Reference

[1] H.N. Tran, S.J. You, A. Hosseini-Bandegharaei, H.P. Chao, Mistakes and inconsistencies regarding adsorption of contaminants from aqueous solutions: A critical review, Water Res. 120 (2017) 88–116. https://doi.org/10.1016/j.watres.2017.04.014.

[2] K.Y. Foo, B.H. Hameed, Insights into the modeling of adsorption isotherm systems, Chem. Eng. J. 156 (2010) 2–10. https://doi.org/10.1016/j.cej.2009.09.013.

[3] Y. Liu, Y. Xiong, P. Xu, Y. Pang, C. Du, Enhancement of Pb (II) adsorption by boron doped ordered mesoporous carbon: Isotherm and kinetics modeling, Sci. Total Environ. 708 (2020) 134918. https://doi.org/10.1016/j.scitotenv.2019.134918.

[4] S. Nethaji, A. Sivasamy, A.B. Mandal, Adsorption isotherms, kinetics and mechanism for the adsorption of cationic and anionic dyes onto carbonaceous particles prepared from Juglans regia shell biomass, Int. J. Environ. Sci. Technol. 10 (2013) 231–242. https://doi.org/10.1007/s13762-012-0112-0.

[5] B. Adane, K. Siraj, N. Meka, Kinetic, equilibrium and thermodynamic study of 2-chlorophenol adsorption onto Ricinus communis pericarp activated carbon from aqueous solutions, Green Chem. Lett. Rev. 8 (2015) 1–12. https://doi.org/10.1080/17518253.2015.1065348.

[6] E.C. Lima, A. Hosseini-Bandegharaei, J.C. Moreno-Piraján, I. Anastopoulos, A critical review of the estimation of the thermodynamic parameters on adsorption equilibria. Wrong use of equilibrium constant in the Van't Hoof equation for calculation of thermodynamic parameters of adsorption, J. Mol. Liq. 273 (2019) 425–434. https://doi.org/10.1016/j.molliq.2018.10.048.

[7] T. Chen, T. Da, Y. Ma, Reasonable calculation of the thermodynamic parameters from adsorption equilibrium constant, J. Mol. Liq. 322 (2021) 114980. https://doi.org/10.1016/j.molliq.2020.114980.